# GLOBAL GYROKINETIC STUDY OF ELECTROMAGNETIC MICROINSTABILITIES IN TOKAMAK PLASMAS

*By*

**ADITYA KRISHNA SWAMY**

(PHYS06200904003)

**Institute for Plasma Research, Gandhinagar**

***A thesis submitted to the***

***Board of Studies in Physical Sciences***

***In partial fulfillment of requirements***

***for the Degree of***

**DOCTOR OF PHILOSOPHY**

***of***

**HOMI BHABHA NATIONAL INSTITUTE**

**September 2015**

# Homi Bhabha National Institute

## Recommendations of the Viva Voce Committee

As members of the Viva Voce Committee, we certify that we have read the dissertation prepared by **Aditya Krishna Swamy** entitled "Global Gyrokinetic Study of Electromagnetic Microinstabilities in Tokamak Plasmas" and recommend that it may be accepted as fulfilling the dissertation requirement for the award of Degree of Doctor of Philosophy.

PKaw ______ **Date :** **1/1/2016**

Chairman - Prof. Predhiman K. Kaw

Avinash ______ **Date :** **1/1/2016**

Examiner - Prof. Avinash Khare

______ **Date :** **1/1/2016**

Guide/Convener - Dr. R. Ganesh

Abhijit ______ **Date :** **1/1/2016**

Member - Prof. Abhijit Sen

______ **Date :** **1/1/2016**

Member - Dr. R. Srinivasan

---

Final approval and acceptance of this dissertation is contingent upon the candidate's submission of the final copies of the thesis to HBNI.

I hereby certify that I have read this dissertation prepared under my direction and recommend that it may be accepted as fulfilling the thesis requirement.

**Date** : 1/1/2016

**Place** : Gandhinagar

**Guide** : Dr. R Ganesh

# STATEMENT BY AUTHOR

This dissertation has been submitted in partial fulfillment of requirements for an advanced degree at Homi Bhabha National Institute (HBNI) and is deposited in the Library to be made available to borrowers under rules of the HBNI.

Brief quotations from this dissertation are allowable without special permission, provided that accurate acknowledgement of source is made. Requests for permission for extended quotation from or reproduction of this manuscript in whole or in part may be granted by the Competent Authority of HBNI when in his or her judgement the proposed use of the material is in the interests of scholarship. In all other instances, however, permission must be obtained from the author.

Aditya Krishna Swamy

# DECLARATION

I, hereby declare that the investigation presented in the thesis has been carried out by me. The work is original and has not been submitted earlier as a whole or in part for a degree / diploma at this or any other Institution / University.

Aditya Krishna Swamy

## List of Publications arising from the Thesis

1. *Global Gyrokinetic Stability of Collisionless Microtearing Modes in Large Aspect Ratio Tokamaks*, Aditya K. Swamy, R. Ganesh, J. Chowdhury, S. Brunner, J. Vaclavik, and L. Villard, Physics of Plasmas 21, 082513 (2014).

2. *Role of Trapped Electrons on Global Gyrokinetic Linear Stability of Collisionless Microtearing Modes*, Aditya K. Swamy, R. Ganesh, J. Chowdhury, S. Brunner, J. Vaclavik, and L. Villard, J. of Phys: Conf. Ser. 561 012017, (2014).

3. *Collisionless Microtearing Modes in Hot Tokamaks: Effect of Trapped Electrons*, Aditya K. Swamy, R. Ganesh, S. Brunner, J. Vaclavik, and L. Villard, Physics of Plasmas 22, 072512 (2015).

4. *Collisionless Microtearing Modes in Large Aspect Ratio Tokamaks with Weak Reversed Shear Configurations*, Aditya K. Swamy, R. Ganesh, S. Brunner, J. Vaclavik, and L. Villard, (*submitted to* Physics of Plasmas (2016)).

5. *Optimization of global gyrokinetic microinstability code EM-GLOGYSTO*, Aditya K. Swamy, R. Ganesh, S. Brunner, J. Vaclavik, and L. Villard, (*to be submitted to* J. Comp. Phys (2016)).

Aditya Krishna Swamy

# DEDICATIONS

To the sweet anticipation of our *paapu*
and
To the memory of *ajja* and *rajiamma*

# ACKNOWLEDGEMENTS

At the very outset, I convey my heartfelt gratitude to my thesis supervisor Dr. Rajaraman Ganesh. His diligent, friendly and spirited support and guidance through this long journey has been the source of inspiration for me. His enthusiasm, impeccable patience and understanding and availability for discussion at practically any time and anywhere made the journey that much easier. I am also thankful to him for providing incredible independence in charting the work, which went a long way in arriving at the present shape.

I am obliged to Prof. P.K. Kaw, Prof. Abhijit Sen and Dr. Srinivasan for consenting to be my Doctoral Committee members. Their unstinting support and listening to their advice through the years have been a pleasant experience. It was a privilege to have them on the committee. Many thanks are also due to the collaborators J. Chowdhury, S. Brunner, L. Villard who were very helpful and supportive all through the project.

I would like to thank Prof. Jha, Prof. Amita Das, Prof. Sudip, Prof. S. Mukherjee, Dr. A Chattopadhyay, Dr. M Kundu, Dr. S Pahari, Dr. M Warrier, Dr. C.V.S Rao and staff at FCIPT for their endurance while teaching us during the first year course work. Prof. P.K. Kaw and Prof. D. Bora, Prof. Sudip Sengupta, Prof. P.K Chattopadhyay, Dr. Joydeep and Prof. S. Mukherjee have been of continuous support and advice in academic affairs.

The library staff, computer centre staff and administrative staff of IPR have always remained cooperative. I convey my thanks to Mrs. Sutapa Ranjan, Mr. Shailendra Trivedi, Mr. Arvind Singh, Mr. Hemant Joshi, Mr. Gaurav Garg, Mr. Prashant Kumar, Mr. Govind Lokhande, Mr. Saroj Das, Mr. Shravan Kumar, Ms. Smita Parmar, Mrs. Shilpa Khandker, Mr. H.C. Khanduri, Mr. Souraban, Mr. Silel Shah, Mr. Dinesh Nair, Mr. Savai Ms. Shirin Bhesania for their help and advice on numerous occasions. I thank Mr. H. Chamunde, Mr. Hitesh Mehta, Mr. S M Patel, Mr. Gohil, Mr. Parmar, Dr. Balakrishnan, Jayendra bhai and others for their active support and cooperation in helping improve Hostel amenities. Among others, interactions with Mr. H.K. Sharma and Mr. P.K. Atrey, Mr. Vartak have been very educative in framing life's philosophies.

The long sojourn in IPR Hostel was made eventful and pleasant by the welcoming team of seniors Vikrant, Maya, Kishor, Shekar, Jugal, Sharad, Satya, Vikram, Kshitish, Ujjwal, Gurudatt, Deepak, Prabhal, Sita, Ashwin, Pravesh, Rameswar, Sanat, Sushil, Sayak and Manjit and fellow students Soumen and Ilyas. The hostel life was only made better by the many contemporary batch of Technical Trainees, as also the juniors Vikram, Veda Prakash, Rana, Vara Prasad, Roopendra, Chandrasekhar, Bibhu, Neeraj, Mangilal, Deepa, Akanksha, Vidhi, Harish, Meghraj, Samir, Sandeep, Sonu, Arghya, Surabhi, Bhumika, Narayan, Ratan, Modhu, Amit, Debraj, Umesh, Dushyant, Sagar, Atul, Jervis, Deepak, Prabhakar, Meenakshi, Pallavi, Alamgir, Sandeep, Harshita, Chetan, Arun, Rupak, Shivam, Avnish, Subroto, Niraj, Srimanto, Dipshika, Garima and others.

My parents B.S. Krishnaswamy and Jayalakshmi have been a continuous source of impeccable support and motivation, to say the least. My heartfelt gratitude to them for all their sacrifices, my brother Aravind, Bindu *attige* and the rest of the larger family for their goodwill and support all through my life. This thesis would not have been possible without the support and love of my dear wife Prithvi.

# Contents

## Abstract

Magnetic confinement of hot plasmas in Tokamaks is one of the important avenues to realize fusion energy, which promises to provide a clean and lasting source of energy for the human civilization. Turbulent transport of energy, particles and momentum is one of the important limiting factors for long time plasma confinement. In a magnetically confined hot plasma which is macroscopically stable, small scale instabilities set in due to the inhomogeneity of the magnetic field. In the presence of equilibrium density and/or temperature gradients, low frequency electromagnetic perturbations become unstable and generate turbulence, which leads to radial transport and thereby undermine long time confinement. Early analytic works in ballooning angle formalism have identified *ballooning parity* modes such as Ion Temperature Gradient mode (ITG), Kinetic Ballooning Mode (KBM) and Electron Temperature Gradient mode (ETG) as some of the important modes which could cause transport through fluctuations, and *tearing parity* modes such as Microtearing modes which change the local magnetic topology and cause transport through stochasticization of the magnetic field.

The framework of modern gyrokinetic theory is well developed and simulations are now able to consider realistic Tokamak configuration and plasma parameters in the limit of low plasma pressure $\beta$. Such simulations, in particular ITG, at the low $\beta$ approximation have been successful in accounting for ion thermal transport to within an order of magnitude or better. However, plasma is at a finite plasma pressure, which brings characteristically new length and time scales to these instabilities and also excites new modes and thereby new transport channels. Obtaining a theoretical understanding of the electron thermal transport has remained a major challenge. Several electron-driven instabilities have been found and investigated, such as the ETG, Trapped Electron Mode (TEM) and the trapped electron-coupled-ITG (ITG-TEM). The relative contribution of these instabilities in different experimental scenarios has been found to be different and a conclusive picture is slowly emerging. Considering plasma parameters relevant to present day experiments, recent simulations have found possibility of existence of unstable microtearing modes. These are inherently multi-scale, kinetic, low frequency electromagnetic mode with tearing parity. Development of advanced gyrokinetic electromagnetic codes and availability of large scale computational facilities have enabled the study of these modes.

In this thesis, global, linear, gyrokinetic study of electromagnetic microinstabilities that cause turbulent transport in Tokamaks is carried out. The primary focus is

to address the possibility of existence of completely collisionless microtearing mode in large aspect ratio, fusion tokamaks. To study multiscale modes such as the microtearing modes, the electromagnetic gyrokinetic spectral code EM-GLOGYSTO has been numerically improved to handle high resolutions. A hybrid MPI-OpenMP parallelization has been introduced to obtain improved runtimes of upto 2x-10x relative to the earlier MPI versions.

Electromagnetic gyrokinetic simulations using EM-GLOGYSTO find the collisionless MTMs linearly unstable in large aspect ratio Tokamaks. By considering only passing particle contribution, the magnetic drift resonance of passing electrons due to the toroidal magnetic configuration is identified as the collisionless drive mechanism. The closely spaced mode rational surfaces due to the high value of safety factor $q$ and magnetic shear couple several poloidal modes, and the global mode is several ion-Larmor radii in width. Several characteristics of MTM are recovered, such as the tearing parity of $\tilde{\varphi}$ and $\tilde{A}_{\|}$, the free energy source being electron temperature gradient, dependence on $\beta$ and the requirement of threshold values of these parameters. The MTM is found to be unstable above a larger $\beta$ threshold than for KBM. At lower $\beta$, the KBM is dominant whereas at larger $\beta$, MTM is found to be more dominant. The $\beta$ threshold for different toroidal modes is found to be different. Importantly, the $\eta$ threshold is found to be lower at higher $\beta$ and vice versa and a stability regime is proposed in $\eta$-$\beta$ space. The MTM is found to have a broad radial spectrum, ranging from ion-Larmor scales to a few electron-Larmor scales, making the mode truly mesoscale.

The inclusion of non-adiabatic trapped electrons is found to contribute to the instability via a resonance of the $\tilde{\varphi}$ fluctuations with the toroidal precessional drift. The trapped electrons destabilize the high-$n$ modes in particular and are significant at smaller aspect ratios. The trapped electron contribute to, and also broaden the range of, short scale fluctuations. The tearing parity of the fluctuations are found to be preserved clearly. The $\beta$ threshold is found to be downshifted by the inclusion of trapped electrons.

The strong dependence of MTM on the closeness of MRS raises questions about its stability in lower shear. A systematic study of dependence on shear by varying global safety factor profiles shows that MTM is relatively stabilized at lower shear and is subdominant to AITG in weak reverse shear configuration. The emergence of unstable mixed parity modes is observed alongside subdominant MTMs in lower shear configurations. The tearing parity modes are found to correlate to the location of high temperature gradient ($dT/ds$) location, unlike the electrostatic ITG mode which localizes about the region of peak logarithmic temperature gradient. In contrast, in weak reverse shear, subdominant MTM mode is found to remain fixed at a radial location regardless of the peak temperature gradient location. The unstable growth rate spectrum is found to extend to relatively shorter wavelengths in weak reverse shear than the monotonic $q$-profile case.

Comprehensive global linear gyrokinetic study of purely collisionless MTM and its comparison to Kinetic Ballooning Mode has been attempted in this thesis in a range of drive factors has increased the understanding of linear electromagnetic microinstabilities.

# List of Figures

# Chapter 1

# Introduction

## 1.1 Magnetic confinement fusion

The modern civilization of humans has entailed an increasing need for energy, resulting in a quest for clean and lasting sources of energy that are alternative to existing sources of energy such as fossil fuels, nuclear fission and wind energy. From time immemorial, the major source of energy for all life on Earth has been the Sun. The core of the Sun is comprised of fully ionized hydrogen nuclei, the strong electrostatic repulsion of which is contained by the self-gravitational compression due to its own mass. The core is millions of Kelvin hot and energy is produced by thermonuclear fusion reaction, a process in which two hydrogen nuclei with sufficient energy breach the electrostatic repulsion and fuse to form a helium nucleus, which has a relatively lesser nuclear mass than the two hydrogen nuclei combined, releasing a large amount of nuclear energy obeying Einstein's famous relation $E = mc^2$. Closer on the Earth, fusion energy can be produced by obtaining a similar "plasma" (i.e. a collective medium of fully ionized ions and electrons) of Deuterium and Tritium. If the plasma sufficiently hot, the energetic nuclei among these fuse to produce fusion energy. This reaction is energetically more feasible alternative to Hydrogen-

Hydrogen fusion [1]. This process produces a net positive energy that can then be extracted in the form of heat to produce electricity [2]. Confinement of such a plasma is achieved by externally applied high magnetic field in the shape of a torus.

In the presence of a magnetic field, the motion of charged particles are confined in the transverse direction by cyclotron motion due to the Lorentz force. A Tokamak is a magnetic confinement system in the shape of a torus, in which the plasma is confined with the help of toroidal magnetic field generated by a set of current coils external to the vessel and poloidal magnetic field generated by plasma current. Topologically, a torus is the only closed surface that can be covered with a vector field, in this case, the confining magnetic field $\vec{B}$, without a fixed point, in accordance with the "Poincare Theorem" [3]. A poloidal magnetic field $B_p$ together with the toroidal magnetic field causes the magnetic field to wind helically around the torus and thereby confines the plasma. The poloidal magnetic field $B_p$ is generated in Tokamaks by driving an inductive current in the toroidal direction, which is also a heating mechanism. As plasma temperature increases, the large angle Coulomb collisions become rarer and inductive heating becomes less efficient. The plasma is heated further in other ways by driving non-inductive current within it [1]. The magnetic field lines confine themselves to closed surfaces (called as flux surfaces) at each radial location with respect to a magnetic axis and wind helically around the surface. The magnetic axis is the unique non-helical field line that winds toroidally and joins itself. The pitch of poloidal magnetic field with the toroidal magnetic field $B_t$ varies with the radius from the magnetic axis due to the current density profile and is called the rotational transform. The inverse of the rotational transform, the so-called the "safety factor" $q(r)$, determines the macroscopic stability properties of the plasma, which can be described by MagnetoHydroDynamic (MHD) model.

In a Tokamak, the "major radius" $R_0$ is the distance of the magnetic axis from the vertical axis at the center of the torus, while "minor radius" $a$ is defined as the

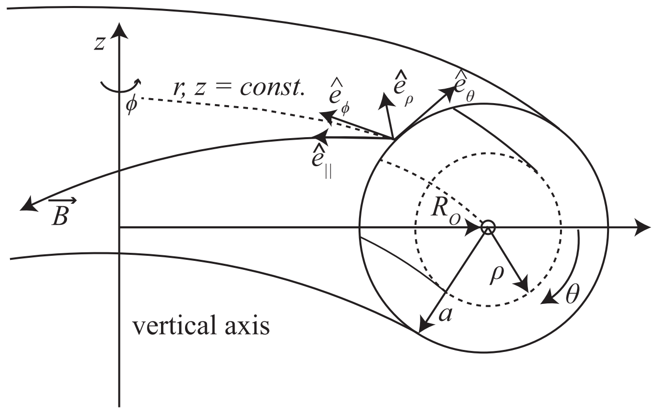


Figure 1.1: Schematic of a large aspect ratio Tokamak geometry. The vertical axis, magnetic axis, major radius $R_0$, minor radius $a$, and unit vectors in toroidal coordinates $(\hat{e}_\rho, \hat{e}_\theta, \hat{e}_\phi)$ are indicated. The radius from the magnetic axis $\rho$ normalized to $a$ is denoted as $s$. The net equilibrium magnetic field winds helically around the torus.

distance from the magnetic axis to the "last closed flux surface" within which the plasma is confined. A schematic of the Tokamak is shown in Fig. 1.1. The ratio $A = R_0/a$ is known as the 'aspect ratio' of the Tokamak. As described later, in the presence of a magnetic field, charged particles gyrate around the magnetic field line, while motion along the field line is unconstrained. Thus, charged ions and electrons "free stream" helically along the field lines and gyrate or have a Larmor motion about the magnetic field. The geometric centre of the Larmor (perpendicular) motion is known as the "guiding centre". As dictated by Maxwell's equations, the magnitude of the toroidal magnetic field decreases as $\sim 1/R$ as one moves away from the vertical axis. The "adiabatic invariance" of the magnetic moment of charged particles implies that some particles get reflected upon reaching a turning point according to the pitch of the perpendicular velocity $v_\perp$ with the parallel velocity $v_\parallel$ and are hence "trapped" within a region towards the outer side of the Tokamak, whereas those particles with high $v_\parallel$ trace a complete field line and are termed "passing particles". In addition, the inhomogeneity of the magnetic field lead to slow drift motion of the guiding centre across the magnetic field. The basic physical and engineering principles for the Tokamak operation are described by J.Wesson in Ref. [1] and in a handbook on the JET mission [4]. Other important alternatives to Tokamaks that are being investigated for achieving fusion are the Stellarators, in which the confining magnetic field is completely generated by a non-axisymmetric set of 3-D coils external to the plasma, Reversed Field Pinch, and the so-called inertial confinement fusion (ICF) in which a tiny blob of fusion fuel is confined and heated by intense laser beams to achieve fusion [2].

## 1.2 Turbulent transport by microinstabilities

Macroscopically confined hot plasma or MHD stable plasma in a Tokamak is not in thermodynamic equilibrium and hence is susceptible to instabilities. In a Tokamak plasma, the temperature and density are high in the core region and fall off rapidly towards the edge of the plasma, closer to the wall of the vessel. The inherent free energy due to the gradients of these quantities in the plasma excite several small scale instabilities called microinstabilities that can lead to turbulent cross-field losses of heat, momentum and particles from the core of the plasma to the outside. A high level of ion thermal transport and a similar level of electron thermal transport is observed in Tokamak experiments. The observed levels are far in excess of analytical estimates expected from known classical and neo-classical (i.e. due to toroidal geometry) theories. Hence, this transport is termed “anomalous”. For the design of future Tokamaks towards a fusion reactor and control of the plasma, transport data from experiments in several past and existing Tokamaks have been used to obtain empirical scaling law [5]. Such an exercise, while inevitable, is expensive, however. Theoretical understanding and predicting turbulent transport from microinstabilities is hence particularly important for fusion because the size (and therefore cost) of future Tokamak reactors is determined by the balance between fusion self-heating and turbulent transport losses that hinder onset of ignition. Extensive progress has been achieved over the years in obtaining the growth, saturation and transport driven by several microinstabilities, in tandem with the development of advanced numerical codes and availability of large-scale computational resources [6, 7, 8].

Considering simplifying assumptions and simple geometries, early analytic predictions have suggested several microinstabilities [9, 10, 11, 12]. These instabilities are variously characterized according to the free energy source, ion vs electron driven modes, length and time scale of fluctuations. In experimental Tokamak plasmas consisting of ions and electrons, the Larmor radii $\rho_j$ (of a particle species $j$) of the particles are much smaller than the typical equilibrium length scales $L$, which are of system size, i.e. $\rho_j/L << 1$. The different length and time scales in microinstabilities can be characterized in terms of this smallness parameter $\epsilon_g \doteq \rho_j/L$ as follows: (a) the mode real frequency is much smaller than the cyclotron frequency of ions/electrons $\omega_r << \omega_{c,j}$ (b) the wavelength is long parallel to the magnetic field: $k_{\|}\rho_j \sim O(\epsilon_g)$ (c) the perpendicular wavelength is of the order of Larmor radii. For ion-driven modes such as Ion Temperature Gradient mode (ITG) [9], Alfvén-Ion Temperature Gradient mode (AITG) [12] (described later), $k_{\perp}\rho_i \sim O(1)$, while for electron-driven modes such as Electron Temperature Gradient mode (ETG) [10], $k_{\perp}\rho_e \sim O(1)$. This set of ordering is usually known as *gyro-ordering*. Microinstabilities can be studied by applying this ordering to kinetic models by averaging over the fast gyromotion and considering only the guiding-centre motion parallel to the field line and slow drift-motion across the flux surfaces. In the last few decades, gyrokinetic framework of theory [13, 14] and simulations has progressed and numerical simulations now are able to consider realistic geometries and plasma parameters based on Tokamak experiments. The gradient in density and/or temperature is a free energy source for various density, temperature and/or pressure gradient instabilities. The plasma pressure in a Tokamak, normalized to the magnetic field energy is defined as the so-called plasma beta: $\beta = 2\mu_0 < p > /B^2$, where $< p >$ is the average plasma pressure and $B$ is the magnitude of Tokamak magnetic field. In the very low $\beta$ limit, the magnetic field fluctuations are negligible and electrostatic potential fluctuations are excited by these gradients. For example, amongst this class of low frequency, short scale instabilities, the one driven by ion temperature gradient (ITG) in the radial direction, the ITG mode destabilizes electrostatic perturbations of the scale of ion-Larmor radius [9]. The ITG mode driven by nonadiabatic ions, is believed to cause anomalous loss, or transport of ion heat at low $\beta$. In the presence of ion temperature gradient, above a certain threshold $(R/L_T)_{crit} \simeq 4$, the mode is destabilized by the torioidal magnetic drift of ions. Several ITG modes interact with each other in the nonlinear regime to generate poloidally symmetric flows with short radial scales called zonal flows. These self-generated zonal flows tend to suppress the instability leading to a non-linear saturation and a nonlinear upshift of the threshold temperature gradient to $(R/L_T)_{crit} \simeq 6$, known as the "Dimits shift" [15]. On the other hand, the non-adiabatic electrons tend to bring fine-scale structures near the mode rational surfaces of ITG modes, while marginally affecting the linear growth rates and its threshold [16].

With increasing plasma $\beta$, due to electromagnetic fluctuations, the ITG mode is stabilized beyond a critical $\beta$. Similarly, in the presence of gradient in electron temperature profile, the Electron Temperature Gradient (ETG) mode is unstable at much shorter scales than ITG. The Trapped Electron Mode is unstable due to the trapped electron dynamics in the presence of a pressure gradient in the edge region of the Tokamak. These modes have been studied extensively and seen to generate electrostatic turbulence, leading to transport in excess of neo-classical estimates [5]. Experimental plasma, however, has a finite plasma pressure; therefore magnetic fluctuations cannot be neglected. As indicated earlier, the presence of magnetic fluctuations fully stabilizes the ITG turbulence between 1% and 2% [12]. The TEM, on the other hand, is found to be insensitive to magnetic perturbations and remain unstable at finite $\beta$ [17]. Above a threshold $\beta$, the Alfvén-ITG or Kinetic Ballooning Mode(KBM) has been shown to become unstable in the presence of ion temperature gradient and grows more unstable with $\beta$ [12, 18, 19]. Thus, fully electromagnetic investigations are necessary for a thorough understanding of the nature of turbulent transport from these instabilities. However, such a problem is difficult to tackle analytically and progress has been made only in the last two decades with the development of fully electromagnetic gyrokinetic codes [20]. Thus electrostatic and electromagnetic modes driven by electrons and/or ions have been extensively studied using gyrokinetic simulations. The particular form of the perturbations in these modes, known as the 'ballooning parity', does not affect the mean magnetic field configuration and causes transport by "flutter" type of fluctuations.

Another class of electromagnetic modes which are driven by electron nonadiabaticity, but are of ion scale (thus inherently mesoscale) are called the tearing parity modes. The tearing parity modes lead to a change in the local magnetic topology. The nature of transport in these broken magnetic fields assuming stochastically generated by tearing parity modes was investigated by Rechester and Rosenbluth [21] and Stix [22], who found that such fields allow free-streaming of the electrons away from the flux surfaces, leading to turbulence and hence increased transport. Tearing parity modes, can generate magnetic islands near the Mode Rational Surfaces (MRS) due to their having $k_{\|} = 0$ near the MRS and $A_{\|}$ even. If the MRSs are closely spaced and and magnetic island widths are sufficiently large to overlap, it leads to a stochasticization of the magnetic field. Thus the MicroTearing Mode (MTM) has recently emerged as an important candidate to understand anomalous transport due to its electron-driven, multi-scale nature that spans length scales from ion-Larmor radii to electron-Larmor radii. Unlike the conventional tearing modes which derive their free energy from electric current gradients, MTMs draw free energy from the electron temperature gradient. These modes do not alter the MHD equilibrium but are rather short scale, low frequency fluctuations that is envisaged to open up an important channel of electron transport.

### 1.2.1 A survey of earlier work done

In the wake of unstable pinch experiments [23] which were earlier predicted to be stable to ideal, large scale hydromagnetic instabilities and triggered by Dungey's suggestion [24] that near an X-point of magnetic field, finite conductivity can lead to an unstably growing electric current density, Furth, Killeen and Rosenbluth [25] proposed a resistive hydromagnetic instability of a current sheet leading to discrete current filaments via a magnetic "tearing" instability. The released magnetic energy was proposed to lead to ideal plasma flow away from the point of "tear". This is the conventional long scale MagnetoHydroDynamic tearing mode. The observation of kink-like oscillations prompted Hazeltine *et.al.* [26] to study tearing modes for plasmas in Tokamaks. Using guiding centre kinetic equations or drift kinetic equations in cylindrical geometry (no toroidal effects) and a Fokker-Planck collision operator, they obtained a general dispersion valid for a range of $\nu_{ei}/\omega_r$, where $\nu_{ei}$ is the electron-ion collision frequency and $\omega_r$ is real frequency of the mode. They predicted that a relatively short scale tearing parity mode can be driven unstable by electron temperature gradient (eTG). In the limit of zero collisionality, this "microtearing mode" was found to be stable. This is perhaps one of the earliest work which found that temperature gradient can also produce a tearing parity electromagnetic mode. Hazeltine and Strauss [27], subsequently invoked this model to estimate using a quasilinear theory, saturated amplitude of $\delta B_r$. These studies were performed in straight cylinder coordinates, used a quasi-linear fluid model and a parallel heat conduction equation dependent on $E_{||}$ and temperature fluctuations (or Thermo Electric force). For a local flattening of equilibrium temperature profile $T_o(r)$ i.e, $dT_o/dr$ small around a $m = n$ surface, saturation amplitudes predicted were of the order $\delta B_r/B \sim 1 \times 10^{-4}$ due to tearing instability, but with large cross-field transport coefficients.

Drake and Lee [28], again using cylindrical coordinates, identified 3 regions of collisionality for MHD tearing modes and 3 regions of collisionality for drift-tearing modes (with real frequency depending on density and temperature gradients), namely collsionless ($\nu_{ei}/w_r << 1$), semicollisional ($\nu_{ei}/w_r \leq 1$) and fully collisional ($\nu_{ei}/w_r > 1$) regimes. In the collisionless limit as defined above, drift tearing modes were moderately found to be unstable and their growth rates were found to be insensitive to density and temperature gradients whereas real frequency was found to depend on density and temperature gradients. In the semi-collisional and collisional limits, both growth rates and real frequencies depended on density and temperature gradients. The authors note that toroidal effects which they neglect is not justifiable. Subsequently, Drake *et.al.* [29] showed that using a shear slab geometry and using a drift kinetic, low $\beta$ (two potential) model for electrons, Microtearing modes (MTM) driven by electron temperature gradient are stable in collisionless regime and in highly collisional regimes. It was shown that in the regime $10 < \nu_{ei}/w_r < 100$, the mode survives with positive growth. Outside this limit, MTM was shown to be stable. For low frequency banana regime, (i.e. $\nu_{ei}/w_r < \epsilon$, where $\epsilon = a/R_0$), Catto and Rosenbluth [30] considered the trapping-passing boundary in velocity space and its contribution to the stability of MTMs. Using a gyrokinetic, radially local calculation, they evaluated the effect of electrons near a narrow passing-trapping boundary in velocity space. Collisions were taken into account via a Lorentz model collision operator. They argued that as the response of barely trapped and barely passing electrons to parallel electric field is different near the passing-trapping boundary, to make a smooth transition, existence of a narrow boundary-layer at the passing-trapping boundary becomes necessary. They found a correction to the growth rate of those obtained by Drake and Lee [28] which further destabilizes the mode. In this work, magnetic drift of passing electrons was neglected as its magnitude was considered to be smaller than the trapped particle drift and opposite in direction. As mentioned earlier, the calculations were local.

Except for a few studies [31, 32], investigations on the tearing parity modes driven by electron temperature gradient was largely dormant until the recent work by Applegate *et al.* [33] which investigated the microinstabilities, in general, in connection to MAST experimental observations. With a linear electromagnetic gyrokinetic numerical study using flux tube code GS2 [34] for MAST-like equilibria, they found amongst host of conventional ballooning parity modes such as ITG, ETG, a mode which possess a tearing parity. It was found that setting collisionality to zero had stabilizing influence on the mode and more importantly, the character of the mode became ITG-like (ballooning parity from tearing). A detailed analysis in 2007 [35] showed that neither the shaping of the flux surfaces in MAST-like equilibria nor the large trapped particles fraction or the type of MHD equilibria ($s-\alpha$, Solovev etc.) was important, but a high value of $\beta$, in the presence of steep electron temperature gradient and collisionality (linearized Lorentz Collision Operator). It was found that the decreasing collisionality stabilized the mode qualitatively consistent with [26, 28]. Mode was strongly destabilized by magnetic drift of passing electrons and electrostatic potential fluctuations. Using GENE [36] flux tube code, Told *et al.* [37] considered for ASDEX Upgrade realistic edge profiles, the linear electromagnetic gyrokinetic simulations which indicate that as the edge profiles steepen, a host of electron temperature gradient driven modes such as ETG, TEMs and MTMs are found. These MTMs were sensitive to collisionality and as collisions are reduced, growth rate of MTMs reduced and were found to couple to TEMs which survive at zero collisionality and zero $\beta$.

Dickinson *et al.* in [38, 39] studied MTMs in edge pedestal region. Starting from MAST experimental, shaped profiles, they considered a closely related circular shifted flux surface and performed local, electromagnetic, gyrokinetic analysis for experimentally relevant, equilibrium profiles of density and electron temperature. It was found that the trapped electrons and their magnetic drifts were more important than the passing electrons as predicted by [35] for MAST-like equilibria for core. MTMs were found to be maximally unstable for weak or zero collisionality. It was indicated that trapped electrons, high $\beta$ and high electron temperature gradient are responsible for this MTM to be unstable in both large and small aspect ratio Tokamaks. For another spherical Tokamak namely NSTX, Guttenfelder *et al.* [40], showed using GYRO electromagnetic gyrokinetic code [41, 42] that for NSTX relevant collisionality, $\beta$ and electron temperature gradient, the linear stability and nonlinear turbulence of MTM explains the observed transport level in NSTX experiments. Internal Transport Barriers were found for self organized Single Helical Axis (SHAx) regimes in Reverse Field Pinch (RFP) device RFX-Mod [43], where steep electron temperature gradient at ITB was found to trigger magnetic activity. Linear stability analysis with GS2 and field mapping indicated MTMs which grow and the magnetic island overlapping produces stochastic transport of electrons. For RFP, a more detailed study [44] with GS2 at the limit of very small collisionality showed the MTMs can be unstable as long as magnetic drift of electrons and sufficient electron temperature gradient is available. Doerk *et al.* [45, 46] investigated microtearing turbulence in standard geometry Tokamak ASDEX-U, with an aspect ratio of 3. In these global electromagnetic gyrokinetic simulations with GENE, the microtearing modes were found to be linearly unstable in collisional plasmas in standard Tokamaks. The mode was found to be unstable and dominate ITG in the low wavenumber range and a 2-D structure of the current layer was obtained, whose width was in close agreement with analytical predictions. In these studies, the dependency on collisionality was found to be weak, but necessary nevertheless. From the non-linear evolution, saturated amplitude of the magnetic perturbations was obtained and found to be described well by the Rechester and Rosenbluth model [21].

In summary, study of microtearing modes, which are short scale kinetic analogues of tearing modes, were begun in the 70's and 80's. In the presence of electron temperature gradient, collisional destabilization was found to sustain the mode in simplified geometries in these analytic works. The hot plasmas in fusion relevant experiments being essentially in a collisionless regime, the MTM was expected to be unimportant, resulting in a hiatus until the early last decade. The development of advanced electromagnetic gyrokinetic formulations and the availibility of large scale computational resources has enabled the study of MTM in realistic toroidal geometries and plasma parameters to understand the observed, large levels of electron thermal transport. Local flux tube simulations for Spherical Tokamaks MAST and NSTX, which operate at high $\beta$ and with significant collisionality found MTMs unstable. Subsequently, unstable collisional MTMs have been reported for several MCF devices, such as the Reversed Field Pinch and standard Tokamaks, typically using local flux-tube simulation. In Spherical Tokamaks, using flux-tube simulations, drift resonance of trapped electrons was identified as a possible source collisionless drive by Dickinson et al.

A natural thought is the following: In large aspect ratio fusion plasmas, the relative fraction of trapped electrons is much less than that of a spherical tokamak. Do such large aspect ratio plasmas support an unstable, collisionless, microtearing mode? If so, what are the collisionless drive mechanisms? What is the role of trapped electrons? If the aspect ratio is reduced, can one establish a qualitative connection with the results of Spherical Tokamak? What is the 2D eigenmode structure of this Mode? Will these modes survive in advanced tokamak magnetic shear configurations? In the following Chapters, using global gyrokinetic electromagnetic simulations as applicable to large aspect ratio fusion plasmas, several of the above stated issues are addressed.

## 1.3 Thesis organization

In **Chapter 2**, the global gyrokinetic formulation implemented in ElectroMagnetic-GLObal GYrokinetic STability of TOkamaks (EM-GLOGYSTO) to study the electromagnetic microinstabilities will be detailed. The formulation is valid to arbitrary wavelengths and hence is capable of studying some of the complex multi-scale microinstabilities considering actual electron-to-ion mass ratio and non-adiabatic electrons and ions. In the past, the code has been used to obtain several features of the mainly ion-scale modes such as ITG, AITG, Kinetic Infernal Modes [47], to mention a few. Optimization of the numerical implementation and introduction of a second level of parallelization using OpenMP results in a speedup of 2x-10x in runtime, thus enabling the study of the problems addressed in this work.

In **Chapter 3**, a comparative study of various electromagnetic microinstabilities previously reported such as finite-$\beta$ ITG, AITG and the Microtearing Mode will be discussed. Collisionless Microtearing Mode are found unstable in large aspect ratio Tokamaks. A clear evidence for the existence of collisionless MTM was reported for the first time during the course of this Thesis. Results on the wavenumber spectrum of the mode, global 2-D structures in the poloidal cross-section, $\beta$-scaling of the mode is discussed. The main drive mechanism leading to the instability is also addressed. Mode sensitivity to global temperature profiles and Landau resonance is investigated.

In **Chapter 4**, the role of non-adiabatic trapped electron population on the Collisionless MTM is studied. Modelling the trapped electron dynamics via a Drift Kinetic Equation, the bounce averaged contribution to the electrostatic potential is obtained in the formulation. At a given aspect ratio, the contribution is found to be destabilizing at high-$n$ but is found to be ineffective for low $n$. At lower aspect ratios, the trapped electron contributions are seen to significantly add to the destabilization. The trapped electrons are seen to bring short-scale structures on each mode rational surface and enlarge the radial wavenumber spectrum of electrostatic potential fluctuations, whereas the magnetic perturbations are more or less unchanged.

In **Chapter 5**, the global mode characteristics of MTM and AITG are explored for their sensitivity to equilibrium safety factor profiles. Keeping in mind, the primarily passing-particle driven nature of these modes, the trapped particles are ignored for this study. This is justified in particular for low-$n$, in accordance with the results of Chapter 4 at large aspect ratio and also helps to delineate the distinct role of passing and trapped particle dynamics on the complex nature of MTM. Considering only passing particles, the sensitivity to global temperature profiles at given $q$-profiles and to global $q$-profile (and hence shear profiles) at a given temperature profile and $q_{min}$ is studied. Multiple MTM and AITG modes are found for any given profile. The dominant MTM mode is found to prefer regions of higher $dT/ds$ in regular safety factor operations, whereas subdominant branches exist that prefer a particular magnetic shear location location and are insensitive to location of $\eta_{max}$. The dominant MTM branch is found to changeover to linearly unstable collisionless mixed parity mode with a change in the global safety factor profile MTM is seen to be very sensitive to $q$ variation relative to AITG.

Finally, in **Chapter 6** a summary of important findings from this global linear gyrokinetic study of MTM and AITG is described. The study of electromagnetic instability is only beginning to gain momentum and several important problems remain to be addressed. Several nontrivial issues that remain outside the scope of this work are outlined including directions along which the model may be improved.

# Chapter 2

# Global linear electromagnetic gyrokinetic model

Global mode structures and stability characteristics of electrostatic and electromagnetic microinstabilities provide useful means to gain insight into turbulent transport processes in tokamak plasmas. The hot plasmas in experimental tokamaks are at intrinsically finite pressure. The study of electromagnetic turbulence and transport is of immense importance since electromagnetic fluctuations not only bring characteristic changes to intrinsically electrostatic modes such as the ITG, but also excite other instabilities such as the Kinetic Ballooning Mode (KBM) at finite $\beta$ [12]. The linear characteristics act as a natural platform for more detailed and realistic nonlinear investigations. Understanding such linear processes can provide a means to predict transport phenomena and to control and/or mitigate such phenomena in order to realize the desired conditions in future reactor tokamaks.

In hot plasmas with ion and electron temperatures of 7-10 KeV and density of the order $10^{18} - 10^{19}\ m^{-3}$, the collision frequency $\nu_{ei}$ is typically much smaller than the real frequency $\omega_r$ of the instabilities, $2\pi\nu_{ei}/\omega_r \lesssim 2 \times 10^{-3}$. As described in the previous chapter, the microinstabilities that produce turbulence can be studied by applying the gyrokinetic ordering. In this thesis, the 2-D global linear characteristics of microinstabilities is studied using the fully gyrokinetic electromagnetic code EM-GLOGYSTO [48, 49]. With circular flux surfaces and an axisymmetric equilibrium in toroidal coordinates $(\rho, \theta, \phi)$, this code models microinstabilities in purely collisionless tokamak plasmas by numerically solving Gyrokinetic Vlasov-Maxwell equations in Fourier space using Nyquist method. The code takes into account finite Larmor radius effects (FLR) to all orders, contribution of passing and trapped particles and Shafranov shift and is fully electromagnetic, with perturbations in the electrostatic potential $\varphi$, the magnetic vector potentials $A_\parallel$ and $A_\perp$. In EM-GLOGYSTO, the passing and trapped particle effects can be delineated and the physics of these species can be addressed separately or together. Both ion electron and ion scales are resolved using a very large number of radial grid points and poloidal Fourier harmonics, keeping intact the physics of FLR at all orders. The high resolution in velocity space allows for dissipationless, accurate description of kinetic effects such as Landau and magnetic drift resonances.

In the past, the code has been extensively used to study different instabilities, namely the Ion Temperature Gradient mode (ITG), Electron Temperature Gradient mode (ETG), Trapped Electron Mode-coupled ITG, Universal Drift Mode, Short wavelength ITG and AITG, as well as the effect of $E \times B$ flows on ITG and AITG modes [18, 19, 48, 49]. The formulation relevant to the present work is described in the remaining Sections of this chapter. For the basic theoretical formulation and implementation, the reader is referred to Refs. [48, 49] and for the electromagnetic formulation, Refs. [18, 19, 50].

## 2.1 Gyrokinetic Formulation

Starting from the Vlasov equation appropriate for collisionless hot plasmas in tokamaks, the standard technique of gyrokinetic change of variables is employed [51] followed by an *eikonal* or *spectral ansatz* to obtain a gyrokinetic Vlasov equation.

Theoretical formulations used here are an extension of those studied in [48, 52] with a major change, namely the use of proper gyrokinetic non-adiabatic passing electron response to the fluctuations. A brief description of the electromagnetic formulation considering $\varphi$ and $A_\parallel$ fluctuations relevant for current studies is presented in the rest of this Section. For details of the full electromagnetic formulation the reader is referred to Ref. [19].

The basic equation for the kinetic description of a collisionless plasma is the Vlasov equation

$$\frac{D}{Dt} f_j(\mathbf{r}, \mathbf{v}, t) = \left[\frac{\partial}{\partial t} + \mathbf{v}\cdot\nabla + \frac{q_j}{m_j}(\mathbf{E} + \mathbf{v}\times\mathbf{B})\cdot\nabla_{\mathbf{v}}\right] f_j(\mathbf{r}, \mathbf{v}, t) = 0 \tag{2.1}$$

where $f_j(\mathbf{r}, \mathbf{v}, t)$ is the distribution function of a given species $j$ of mass $m_j$ and electric charge $q_j$ and $\mathbf{E}(\mathbf{r}, t)$, $\mathbf{B}(\mathbf{r}, t)$ are the electromagnetic fields consistent with Maxwell's equations. For a linear stability study, the full distribution function $f_j(\mathbf{r}, \mathbf{v}, t)$ of species $j$ is linearized about a suitable equilibrium $f_{0j} = f_{0j}(\mathbf{r}, \mathbf{v})$ such that $f_j(\mathbf{r}, \mathbf{v}, t) = f_{0j}(\mathbf{r}, \mathbf{v}) + \tilde{f}_j(\mathbf{r}, \mathbf{v}, t)$ with the assumption that $\tilde{f}_j/f_{0j} \ll 1$. The equilibrium distribution function is invariant along the equilibrium or *unperturbed* trajectories of particles, so that,

$$\left.\frac{D}{Dt}\right|_{u.t.p.} f_{0j}(\mathbf{r}, \mathbf{v}) = 0$$

where $u.t.p$ implies unperturbed trajectories of particles, with

$$\left.\frac{D}{Dt}\right|_{u.t.p.} \equiv \frac{\partial}{\partial t} + \mathbf{v}\cdot\nabla + \frac{q_j}{m_j}(\mathbf{v}\times\mathbf{B}_0)\cdot\nabla_{\mathbf{v}} \tag{2.2}$$

The linearized equation is

$$\left.\frac{D}{Dt}\right|_{u.t.p.} \tilde{f}_j(\mathbf{r}, \mathbf{v}, t) = -\frac{q_j}{m_j}(\tilde{\mathbf{E}} + \mathbf{v}\times\tilde{\mathbf{B}})\cdot\nabla_{\mathbf{v}} f_{0j} \tag{2.3}$$

Here $\tilde{\mathbf{E}}$ and $\tilde{\mathbf{B}}$ are the perturbed electric and magnetic fields such that $\mathbf{E} = \mathbf{E}_0 + \tilde{\mathbf{E}}$ and $\mathbf{B} = \mathbf{B}_0 + \tilde{\mathbf{B}}$, where $\mathbf{E}_0$ and $\mathbf{B}_0$ are the equilibrium fields. For the studies in this work, the equilibrium electric field $\mathbf{E}_0$ is considered to be zero.

Then, following change of variables $(\mathbf{r}, \mathbf{v}) \rightarrow (\mathbf{r}, \varepsilon = v^2/2,\ \mu = v_\perp^2/2B,\ \psi_{0j})$ wherein the particle canonical angular momentum for species $j$ is $\psi_{0j} = \hat{e}_\phi \cdot [\mathbf{r} \times (\mathbf{A} + m_j\mathbf{v}/q_j)] = \psi + m_j r v_\phi/q_j$, and $\psi = rA_\phi$ is the poloidal flux function per unit radian, $v_\phi$ the particle speed in the toroidal direction, one obtains $f_{0j}(\mathbf{r}, \mathbf{v}) = f_{0j}(\mathbf{r}, \varepsilon, \mu, \psi_{0j})$. Such a transformation enables one to express $f_{0j}$ in terms of single particle constants of motion $(\varepsilon,\ \mu,\ \psi_{0j})$. Thus the $\nabla_\mathbf{v} f_{0j}$ term on the right hand side $(r.h.s)$ of Eq. (2.3) becomes

$$\nabla_\mathbf{v} f_{0j}(\mathbf{r}, \varepsilon, \mu, \psi_{0j}) = \mathbf{v}\left(1 + \frac{m_j r v_\phi}{q_j}\frac{\partial}{\partial\psi_{0j}}\right)\frac{\partial f_{0j\psi}}{\partial\varepsilon} + \frac{\mathbf{v}_\perp}{B}\frac{\partial f_{0j\psi}}{\partial\mu} + \hat{e}_\phi\frac{m_j r}{q_j}\frac{\partial f_{0j}}{\partial\psi_{0j}}\bigg|_{\psi_0=\psi} \quad (2.4)$$

where $f_{0j\psi} \equiv f_{0j}(\psi_{0j} = \psi)$ and $\hat{e}_\phi$ is the toroidal unit vector. To obtain Eq. (2.4), $f_{0j}$ is Taylor expanded to first order in $(m_j/q_j)rv_\phi$ about $\psi_{0j} = \psi$. Then, the following *gyrokinetic ordering* is used $\epsilon_g \doteq \varrho_{Lj}/L_{eq},\ \omega/w_{cj} \sim O(\epsilon_g),\ k_\perp\varrho_{Lj} \simeq O(1),\ k_\parallel\varrho_{Lj} \simeq O(\epsilon_g)$ where $k_\perp, k_\parallel$ are perpendicular and parallel wavenumbers respectively, $\varrho_{Lj}$ is the Larmor radius of the species $j$ and $L_{eq}$ is a typical equilibrium scale length, such as the length scale over which the equilibrium temperature profile varies.

Rewriting $\tilde{f}_j$ in Eqs.(2.3), in terms of the explicit adiabatic contribution and the non-adiabatic remainder $h_j^{(0)}$:

$$\tilde{f}_j = h_j^{(0)} + \frac{\tilde{\varphi}q_j}{m_j}\left(1 - \frac{v_\phi}{\Omega_{pj}}\nabla_n\right)\frac{\partial f_{0j\psi}}{\partial\varepsilon} + \frac{q_j}{m_j B}\frac{\partial f_{0j\psi}}{\partial\mu}\left(\tilde{\varphi} - v_\parallel\tilde{A}_\parallel\right) - \frac{q_j}{m_j}\frac{\tilde{A}_\phi}{\Omega_{pj}}\nabla_n f_{0j\psi} \quad (2.5)$$

In the large aspect ratio limit with circular flux surfaces $\tilde{A}_\parallel$ and $\tilde{A}_\phi$ are related by $\tilde{A}_\parallel = \hat{e}_\parallel \cdot \tilde{\mathbf{A}} = b_\phi\tilde{A}_\phi + b_\theta\tilde{A}_\theta$, where $b_\phi = \hat{e}_\phi \cdot \mathbf{B}_0/|\mathbf{B}_0|$ and $b_\theta = \hat{e}_\theta \cdot \mathbf{B}_0/|\mathbf{B}_0|$. The quantities $\tilde{A}_\phi$ and $\tilde{A}_\theta$ are toroidal and poloidal components of the vector potential $\tilde{\mathbf{A}}$. Invoking the previously mentioned gyrokinetic ordering followed by some standard algebra, one arrives at

$$\left.\frac{D}{Dt}\right|_{u.t.p} h_j^{(0)}(\mathbf{r},\mathbf{v},t) = -\frac{q_j}{m_j}\left[\frac{\partial f_{0j\psi}}{\partial \varepsilon}\frac{\partial}{\partial t} + \frac{v_{||}}{B}\frac{\partial f_{0j\psi}}{\partial \mu}\hat{e}_{||}\cdot\nabla + \frac{\nabla_n f_{0j\psi}}{\Omega_{pj}}\hat{e}_{\phi}\cdot\nabla\right]\times$$
$$(\tilde{\varphi} - \mathbf{v}\cdot\tilde{\mathbf{A}}) + O(\epsilon_g^2) \qquad (2.6)$$

In Eqs.(2.5-2.6), the following definitions are introduced: $\nabla_n = -rB_p\frac{\partial}{\partial\psi}, \Omega_{pj} = w_{cj}b_p$, $w_{cj} = q_jB/m_j$. $b_p = B_p/B$ and $B_p = |\nabla\psi|/r$. $h_j^{(0)}$ is the zeroth order term of the perturbative series in the “inverse gyro-frequency expansion” of the nonadiabatic part $h_j = h_j^{(0)} + (1/w_{cj})h_j^{(1)} + (1/w_{cj}^2)h_j^{(2)}....$ Note that since $D/Dt \simeq O(w_{cj})$, only $h_j^{(0)}$ is retained which is independent of $w_{cj}$ and hence the gyro-angle (defined below). In the rest of this presentation $h_j^{(0)}$ is referred simply as $h_j$. Eq. (2.6) is our starting equation.

The gyroaverging proceeds as follows. In a large aspect ratio tokamak geometry, the velocity $\mathbf{v}$ of a particle gyrating around a field line is $\mathbf{v} = v_\perp(\hat{e}_\rho\cos\alpha + \hat{e}_\theta\sin\alpha) + v_\|\hat{e}_\|$ where unit vectors $\hat{e}_\rho, \hat{e}_\theta, \hat{e}_\phi$ define the toroidal coordinates and $\alpha$ is the gyroangle. Gyro-averaging a quantity “Q” is defined as

$$< Q >= \frac{1}{2\pi}\int_0^{2\pi} d\alpha Q(\alpha; ..)$$

In Eq. (2.6), the terms in square brackets [..] on the right hand side (*r.h.s.*) are all *equilibrium quantities* and are independent of $\alpha$. Thus only the potentials need to be averaged. Similarly, on the left hand side (*l.h.s*), $h_j$ is independent of $\alpha$, hence, only $D/Dt|_{u.t.p}$ is to be gyro-averaged. Therefore,

$$\left.\frac{D}{Dt}\right|_{u.t.p} \overset{gyro-averaging}{\Longrightarrow} \left.\frac{D}{Dt}\right|_{u.t.g} \equiv \frac{\partial}{\partial t} + (v_\|\hat{e}_\| + \mathbf{v}_{dj})\cdot\frac{\partial}{\partial\mathbf{R}}$$

where $\mathbf{v}_{dj} = (v_\perp^2/2 + v_\|^2)\hat{e}_z/(rw_{cj})$, *u.t.g.* implies *unperturbed trajectory of guiding* *centers* $\mathbf{R}$ defined by $\mathbf{R} = \mathbf{r} + \mathbf{v} \times \hat{e}_{\|}/w_{cj}$. Therefore,

$$< \tilde{\varphi} - \mathbf{v} \cdot \tilde{\mathbf{A}} > = \frac{1}{2\pi} \int_0^{2\pi} d\alpha \left[ \tilde{\varphi}(\mathbf{r}[\alpha], t) - \mathbf{v} \cdot \tilde{\mathbf{A}}(\mathbf{r}[\alpha], t) \right] \Bigg|_{\mathbf{r}=\mathbf{R}-\mathbf{v}\times\hat{e}_{\|}/w_{cj}}$$

Since $\tilde{\varphi}(\mathbf{r}[\alpha], t)$ and $\tilde{\mathbf{A}}(\mathbf{r}[\alpha], t)$ are unknown functions, the gyro-averaging is performed by first Fourier decomposing these functions, then representing the particle coordinate $\mathbf{r}$ by the gyro-center $\mathbf{R}$ and utilizing

$$J_p(x) = \frac{1}{2\pi} \int_0^{2\pi} d\alpha \exp[i(x\text{sin}\alpha - p\alpha)]$$

one obtains a gyro-averaged equation for the nonadiabatic distribution function.

For low but finite $\beta$, $B_{\|}$ fluctuations are neglected so that $\tilde{\mathbf{A}} = \tilde{A}_{\|}\hat{e}_{\|}$. However, generalization to include $\mathbf{B}_{\|}$ fluctuations is obtained by setting $\tilde{\mathbf{A}} = \tilde{A}_{\|}\hat{e}_{\|} + \tilde{A}_{\theta}\hat{e}_{\theta}$ [19], which leads to a Bessel function $J_1$. It will be seen later in Chapter 3 that for the problem of interest, namely microtearing instability, the inclusion of $B_{\|}$ fluctuations in a $\beta$ scaling study does not affect the calculations even at very high values of $\beta$. Hence, unless otherwise specified, electromagnetic fluctuations are taken to imply only the low $\beta$ approximation where $\tilde{\mathbf{A}} = \tilde{A}_{\|}$. With the above said procedure, one obtains the following *gyrokinetic equation*:

$$\frac{D}{Dt}\bigg|_{u.t.g} h_j(\mathbf{R}, \mathbf{v}, t) = -\left(\frac{q_j}{m_j}\right) \left[ \frac{\partial f_{0j\psi}}{\partial \varepsilon} \frac{\partial}{\partial t} + \frac{v_{\|}}{B} \frac{\partial f_{0j\psi}}{\partial \mu} \hat{e}_{\|} \cdot \nabla + \frac{1}{\Omega_{pj}} \nabla_n f_{0j} \bigg|_{\psi} \hat{e}_{\phi} \cdot \nabla \right] \times \\ \Big( \tilde{\varphi}(\mathbf{k};) J_0(k_{\perp} \varrho_{Lj}) - v_{\|} \tilde{A}_{\|}(\mathbf{k};) J_0(k_{\perp} \varrho_{Lj}) \Big) + O(\epsilon_g^2) \qquad (2.7)$$

Here, $\nabla_n \equiv \nabla_\rho = \partial/\partial\rho$, $\mathbf{k} = \kappa\ \hat{e}_\rho + k_\theta\ \hat{e}_\theta + k_\phi\ \hat{e}_\phi$ and $\kappa = (2\pi/\Delta\rho)\ n_\rho$, with $\Delta\rho = \rho_u - \rho_l$ which defines the radial domain, $k_\phi = n/r$, $k_\theta = m/\rho$; and $(n_\rho, m, n)$ are radial, poloidal and toroidal mode numbers respectively. (In later Chapters, $r$ is used for the radial variable $\rho$ and the notation for radial wavenumber $\kappa$ and $k_r$ are used interchangeably). The solution to Eq. (2.7) is obtained by the *Green's function technique* (unit source solution *say* $\mathcal{P}$) [53]. An explicit form of $\mathcal{P}$ is obtained analytically by the method of characteristics of *unperturbed trajectories of guiding centers* (*u.t.g*) and followed by a perturbative technique for the guiding center velocity [49]. Moreover, the unit source solution, $\mathcal{P}$, to Eq. (2.7) is independent of the type of perturbation (electrostatic or electromagnetic) and solely depends on the considered *equilibrium*. The equilibrium distribution function $f_{0j}$ is assumed to be a local Maxwellian of the form

$$f_{0j}(\varepsilon,\mu,\psi) = f_{Mj}(\varepsilon,\psi) = \frac{N(\psi)}{(2\pi T_j(\psi)/m_j)^{3/2}}\ \exp\left(-\frac{\varepsilon}{T_j(\psi)/m_j}\right)$$

so that $\partial f_{0j}/\partial\mu \equiv 0$ by choice and density profile $N(\psi)$ is independent of the species type $j$. Thus, for a "sinusoidal" time dependence, the solution to Eq. (2.7) in guiding center coordinates $\mathbf{R}$ is :

$$\begin{aligned} h_j(\mathbf{R},\mathbf{v},\omega) = &-\left(\frac{q_j F_{Mj}}{T_j}\right)\int d\mathbf{k}\exp\left(i\mathbf{k}\cdot\mathbf{R}\right)\left(\omega-\omega_j^*\right)\left(i\ \mathcal{P}_j\right) \\ &\times\left(\tilde{\varphi}(\mathbf{k};)J_0(k_\perp\varrho_{Lj}) - v_\parallel\tilde{A}_\parallel(\mathbf{k};)J_0(k_\perp\varrho_{Lj})\right) + O(\epsilon_g^2) \end{aligned}$$

where $\omega$ is the *eigen value* and $\omega_j^* = \omega_{nj}\left[1+\frac{\eta_j}{2}\left(\frac{v_\parallel^2+v_\perp^2}{v_{thj}^2}-3\right)\right]$ wherein $\omega_{nj} = (T_j\nabla_n \ln Nk_\theta)/(q_jB)$ is the *diamagnetic drift frequency*; $\eta_j = (d\ln T_j)/(d\ln N)$. Note also that since the equillibria considered are axisymmetric, the toroidal mode number $n$ can be fixed and the problem is effectively two dimensional in $(r,\theta)$ (configuration space) or $(\kappa,k_\theta)$ (Fourier space).

The unit source solution $\mathcal{P}$ for a given $(\mathbf{k},\omega)$ is,

$$\begin{aligned} \mathcal{P}(\mathbf{R},\mathbf{k},\varepsilon,\mu,\sigma,\omega) &= \int_{-\infty}^{t} dt'\exp\left(i\left[\mathbf{k}\cdot(\mathbf{R}'-\mathbf{R})-\omega t'\right]\right) \\ &= \int_{-\infty}^{t} dt'\exp\left(i\int^{t'} dt''\mathbf{k}\cdot\mathbf{v}_g(t'')-i\omega t'\right) \end{aligned} \tag{2.8}$$

where the guiding center velocity $d\mathbf{R}/dt = \mathbf{v}_g = \mathbf{v}_{\|} + \mathbf{v}_d$ and $\mathbf{R}(t)$ is obtained by solving for the unperturbed guiding center trajectories as an "initial value problem".

*Passing ions and electrons:* For passing particles, the solution is obtained analytically by first assuming the cross-field drift terms $[\mathbf{v}_d]$ to be small and drop them at the zeroth order and to include them iteratively at the next order. This procedure gives us an explicit form for passing particle propagator as:

$$i\mathcal{P} = \sum_{p,p'} \frac{J_p(x_{tj}^{\sigma}) J_{p'}(x_{tj}^{\sigma})}{\omega + k_\theta v_{dz} - \sigma k_{||} v_{||} - p\omega_t} \exp(i(p-p')(\theta - \bar{\theta}_\sigma)) \tag{2.9}$$

where $x_{tj}^{\sigma} = k_\perp \xi_\sigma$, $\xi_\sigma = v_d/\omega_t$, $v_d = \left(v_\perp^2/2 + v_\|^2\right)/(\omega_c R)$, $\omega_t = \sigma v_\|/(q(s)R)$, $\sigma = \pm 1$ (sign of $\mathbf{v}_\|$), $k_\perp = \sqrt{\kappa^2 + k_\theta^2}$, $k_\| = [nq(s) - m]/(q(s)R)$ and $\bar{\theta}_\sigma$ is defined as $\tan\bar{\theta}_\sigma = -\kappa/k_\theta$ and $s = r/a$, $a-$ is the minor radius at the plasma edge. To obtain the particle density fluctuation $\tilde{n}_j(\mathbf{r};\omega)$ and current density fluctuation $\tilde{j}_j(\mathbf{r};\omega)$, one needs to go from guiding center $(g.c.)$ co-ordinate $\mathbf{R}$ to *particle co-ordinate* $\mathbf{r}$ using $\mathbf{R} = \mathbf{r} + \mathbf{v} \times \hat{e}_\|/w_{cj}$, by replacing $h_j$ using Eq. (2.5) followed by the integration over $\mathbf{v}$ keeping in mind the *gyro-angle* integration over $\alpha$. This last integration on $\alpha$ yields an additional Bessel function "$J_0$" for $\tilde{\varphi}$ and $\tilde{A}_\|$.

A few points to be noted here are as follows: (1) In arriving at this solution, the parallel velocity of the particles are assumed to remain unchanged as they pass through the high field side. That is, the modulation of $v_\|$ due to inhomogeneity of the magnetic field $B$ is assumed to be weak and hence negligible. In this sense, particles are considered as "highly passing". (2) The grad-$B$ and curvature drift effects appear through the drift $v_{dz}$ in the argument of Bessel functions ($x_{tj}^{\sigma} = k_\perp v_d/\omega_t$) and the term $k_\theta v_{dz}$ in the denominator in Eq. (2.9). Thus for example, "radial" and "poloidal coupling" vanishes if $v_{dz}$ in Eq. (2.9) and one would recover the "cylindrical" results. (3) The argument of Bessel functions $J_p$'s in Eq. (2.9) i.e., $x_{tj}^{\sigma} = k_\perp \xi_\sigma$ also depends on transit frequency $\omega_t$, $x_{tj}^{\sigma}$ can become $x_{tj} \simeq \mathcal{O}(1)$.

Hence transit harmonic orders are to be chosen accordingly. In this form $\mathcal{P}$ contains effects such as transit harmonic and its coupling, parallel velocity resonances and poloidal mode coupling. (4) Finite plasma pressure results in a compression of the nested flux-surfaces in the outboard side and is known as Shafranov Shift ($\Delta$) where $\Delta(\rho)$ is the shift measured from magnetic axis. EM-GLOGYSTO takes into account Shafranov shifted circular equilibrium and its effects on the equilibrium trajectories of the particles for small shifts with $\Delta' \simeq O(A^{-1})$. $\Delta$ is the shift from the magnetic axis. For details of the Shafranov shift corrected unit source solution, $\mathcal{P}$ see Refs. [18, 19]. However, for the purposes of present thesis, the corresponding changes due to Shafranov shift are ignored.

*Trapped electrons :* The mirror effect due to the inhomogeneous magnetic field of the tokamak causes a fraction of the population of ions and electron species to be trapped in the outboard region of the tokamak. These particles trace the well known banana orbit with a slow precessional drift in the toroidal direction. Considering a particle at its thermal velocity, the bounce frequency is $\omega_b \sim \sqrt{A^{-1}} v_{th}/qR$. Microinstabilities typically have real frequencies $\omega_r \sim v_{thi}/a$. Thus bounce frequency of trapped ions is low, $\omega_{bi}/\omega_r << 1$ and can be neglected. On the other hand, the bounce frequency of electrons is much higher, $\omega_{be}/\omega_r >> 1$. Hence, a bounce period averaged response of the trapped electron dynamics to the perturbations is considered. The Larmor radius of the electrons is smaller than that of ions by a factor $\sqrt{m_i/m_e}$. Hence, for instabilities with $k_\perp \rho_i \sim O(1)$, FLR effects of electrons are negligible and a Drift Kinetic Equation is used to model them following Ref. [49].

The fluctuating part of the guiding center (GC) distribution function is defined as $\tilde{f}_g = \tilde{g}_g - q\tilde{\varphi}F_M/T$, where $\tilde{g}_g$ is the non-adiabatic part. With perturbations of the form $\exp i(\omega t - n\phi)$, where $n$ is the toroidal mode number and $\phi$ is the toroidal angle, the evolution equation for $\tilde{g}_g$ is obtained as

$$\left.\frac{D}{Dt}\right|_{u.t.g}\tilde{g}_g = -\frac{q}{T}F_M i(\omega-\omega^*)\tilde{\varphi}$$

with $\omega^* = -\frac{T}{qB}\nabla_n lnF_M\frac{B}{B_p}k_\phi = \omega_n[1+\eta(\varepsilon/v_{th}^2-3/2)]$ and $\omega_n = -\frac{T}{qB}\nabla_n lnN\frac{B}{B_p}k_\phi$. This equation is then expanded to different orders in small parameter $\epsilon_b = \omega/\omega_b \ll 1$. Subtracting the slow precessional drift $<\dot{\phi}>$ from the fast periodic trapping motion and assuming $\omega \sim \omega^*$, one can write to lowest order in $\epsilon_b$,

$$\left(\vec{v_g}\cdot\frac{\partial}{\partial\vec{R}} - <\dot{\phi}>\frac{\partial}{\partial\phi}\right)\tilde{g}_g^{(0)} = 0,$$

where $\vec{R}$ is the guiding center coordinate. Thus $\tilde{g}_g^{(0)}$ is constant along the non-drifting banana orbits and to first-order,

$$\left(\vec{v_g}\cdot\frac{\partial}{\partial\vec{R}} - <\dot{\phi}>\frac{\partial}{\partial\phi}\right)\tilde{g}_g^{(1)} - i(\omega-n<\dot{\phi}>)\tilde{g}_g^{(0)} = -\frac{q}{T}F_M i(\omega-\omega^*)\tilde{\varphi} \tag{2.10}$$

Averaging this relation over a complete banana trajectory leads to the actual bounce-averaged equation

$$(\omega-n<\dot{\phi}>)\tilde{g}_g^{(0)} = \frac{q}{T}F_M(\omega-\omega^*) <\tilde{\varphi}>_b .$$

Thus, $\tilde{g}_g^{(0)} = \frac{q}{T}F_M\frac{\omega-\omega^*}{\omega-n<\dot{\phi}>} <\tilde{\varphi}>_b$, with

$$<\tilde{\varphi}>_b(\vec{R},\varepsilon,\mu) = \frac{1}{\tau_b}\int_0^{\tau_b} dt\varphi(\vec{R}'),$$

such that $\vec{R}'(t=0) = \vec{R}$, where $\varepsilon$ is the kinetic energy and $\mu$ is the magnetic moment.

By integrating only along the parallel motion of the GC, thus neglecting the finite banana width effects, one obtains in the general flux coordinates $(\psi, \chi, \phi)$,

$$< \tilde{\varphi} >_b = \frac{1}{\tau_b} \int_0^{\tau_b} dt \varphi(\psi, \chi') e^{in\phi'} = \frac{1}{\tau_b} 2 \int_{\chi_2}^{\chi_1} d\chi' \frac{JB}{|v_\parallel|} \varphi(\psi, \chi') e^{in(\phi - \int_{\chi'}^{\chi} \frac{JB_\phi}{r} d\chi'')} \\ = \bar{\varphi}(\psi, \lambda) e^{in(\phi - \int^{\chi} \frac{JB_\phi}{r} d\chi')} \tag{2.11}$$

where

$$\bar{\varphi}(\psi, \lambda) = \left( \int_{\chi_2}^{\chi_1} d\chi \frac{JB}{\sqrt{1 - \lambda B/B_0}} \right)^{-1} \int_{\chi_2}^{\chi_1} d\chi \frac{JB}{\sqrt{1 - \lambda B/B_0}} \varphi(\psi, \chi) e^{-in(\int^{\chi} \frac{JB_\phi}{r} d\chi')} \tag{2.12}$$

and using $\psi = \text{const}$, $d\chi/dt = -v_\parallel/JB$, $d\phi/d\chi = JB_\phi/r$ along the lowest order trajectories. Here $J$ is the Jacobian, $\lambda = \mu B_0/\varepsilon$ is a constant for a given energy along the trajectories, $\chi_1, \chi_2$ are the turning points.

*Closure:* In real space $\mathbf{r}$, for species $j$, one finally obtains the passing and trapped particle density fluctuations ($\tilde{n}_j^c$, $\tilde{n}_j^t$ respectively), and parallel current fluctuations $\tilde{j}_{\parallel j}$ as:

$$\tilde{n}_j = \tilde{n}_j^c + \tilde{n}_j^t \tag{2.13}$$

where

$$\tilde{n}_j^t = -\left(\frac{q_j N}{T_j}\right) \left[ \alpha_t \tilde{\varphi} + < \tilde{\varphi} >_b \right] \tag{2.14}$$

$$\tilde{n}_j^c = -\left(\frac{q_j N}{T_j}\right) \left[ \alpha_c \tilde{\varphi} + \int d\mathbf{k} e^{i\mathbf{k}\cdot\mathbf{r}} \int d\mathbf{v} \frac{f_{Mj}}{N} \left(\omega - \omega_j^*\right) (i\mathcal{P}_j) \left[\tilde{\varphi}(\mathbf{k};) - v_\parallel \tilde{A}_\parallel(\mathbf{k};)\right] \times \\ J_0^2(x_{Lj}) \right], \tag{2.15}$$

$$\tilde{j}_{\parallel j} = -\left(\frac{q_j^2}{T_j}\right)\left[\int d\mathbf{k}e^{i\mathbf{k}\cdot\mathbf{r}}\int v_\parallel d\mathbf{v} f_{Mj}\left(\omega - \omega_j^*\right)(i\mathcal{P}_j)\left[\tilde{\varphi}(\mathbf{k};) - v_\parallel \tilde{A}_\parallel(\mathbf{k};)\right]\times J_0^2(x_{Lj})\right], \tag{2.16}$$

where $x_{Lj} = k_\perp \varrho_{Lj}$. Owing to the average over the bounce motion, the terms containing the velocity moments cancel, therefore electromagnetic effects do not enter in the contribution of the trapped particle population. It may be worthwhile to emphasize here that (i) equilibrium effects (incorporated in $\mathcal{P}$) and perturbation effects are clearly delineated in the formulation (ii) a Solovev-type solution for flux surfaces at large aspect ratio is considered. This enables one to analytically obtain the particle response to electromagnetic perturbations in this numerical model.

As is well known, the underlying plasma current profile, which results in the global safety factor profile, and the equilibrium pressure gradients need to be consistent to an ideal MHD equilibrium magnetic field structure. However, the Solovev-type simplification, as employed here, implies a constant safety factor across the minor radius. Nevertheless, radially varying q-profiles are used. Hence, to this extent, the global profiles used in this formulation are *ad-hoc* with respect to the equilibrium magnetic configuration. Ideally, the equilibrium magnetic configuration is to be obtained as a solution to the Grad-Shafranov equation considering pressure and current profiles from an actual experimental MHD equilibrium. However, in the present study, the pressure profiles and magnetic safety factor profiles may not necessarily obey ideal MHD radial force balance. The global profiles employed in studies with this formulation are assumed to be close to the actual equilibrium and have minimal bearing on the quantitative observations in the large aspect ratio limit.

Equations are finally closed by invoking the Poisson equation and the component of Ampère's law parallel to $\mathbf{B}$:

$$\nabla^2 \tilde{\varphi} = -\frac{1}{\epsilon_0} \sum_j q_j \tilde{n}_j(\mathbf{r};\omega); \quad \frac{1}{\mu_0} \nabla_\perp^2 \tilde{A}_\parallel = -\sum_j \tilde{j}_{\parallel j} \tag{2.17}$$

By Fourier decomposing the potentials in Eq. (2.17) and then taking the Fourier transform of this same equation, one obtains a convolution matrix in Fourier space. Considering a hydrogen-like plasma with ions and electrons,

$$\sum_{\mathbf{k}'} \begin{pmatrix} \sum_{j=i,e} \mathcal{M}^j_{\tilde{\varphi}\tilde{\varphi},\mathbf{k},\mathbf{k}'} & \sum_{j=i,e} \mathcal{M}^j_{\tilde{\varphi}\tilde{A}_\parallel,\mathbf{k},\mathbf{k}'} \\ \sum_{j=i,e} \mathcal{M}^j_{\tilde{A}_\parallel\tilde{\varphi},\mathbf{k},\mathbf{k}'} & \sum_{j=i,e} \mathcal{M}^j_{\tilde{A}_\parallel\tilde{A}_\parallel,\mathbf{k},\mathbf{k}'} \end{pmatrix} \begin{pmatrix} \tilde{\varphi}_{\mathbf{k}'} \\ \tilde{A}_{\parallel,\mathbf{k}'} \end{pmatrix} = 0 \tag{2.18}$$

where $\mathbf{k} = (\kappa, m)$ and $\mathbf{k}' = (\kappa', m')$. The Laplacian of $\tilde{\varphi}$ and for the parallel component of Ampère's law is also included to the appropriate matrix elements. The submatrices $\mathcal{M}$ are symmetric about the diagonal. With the following definitions, $\Delta_\kappa = \kappa - \kappa'$ and $\Delta_m = m - m'$ matrix elements are :

$$\begin{aligned}
\mathcal{M}^i_{\tilde{\varphi}\tilde{\varphi},\mathbf{k},\mathbf{k}'} &= \frac{1}{\Delta r} \int_{r_l}^{r_u} dr \exp(-i\Delta_\kappa r) \times \left[ \alpha_p \delta_{mm'} + \exp(i\Delta_m \bar{\theta}) \sum_p \hat{I}^0_{p,i} \right], \\
&\quad - \frac{1}{\Delta r} \int_{r_l}^{r_u} dr \exp(-i\Delta_\kappa r) \times \left( \kappa'^2 + \frac{m'^2}{r^2} \right) \left( \frac{\epsilon_0 T_i(r)}{q_j^2 N} \right), \\
\mathcal{M}^i_{\tilde{\varphi}\tilde{A}_\parallel,\mathbf{k},\mathbf{k}'} &= -\frac{1}{\Delta r} \int_{r_l}^{r_u} dr \exp(-i\Delta_\kappa r) \times \left[ \exp(i\Delta_m \bar{\theta}) \sum_p \hat{I}^1_{p,i} \right], \\
\mathcal{M}^e_{\tilde{\varphi}\tilde{\varphi},\mathbf{k},\mathbf{k}'} &= \frac{1}{\Delta r} \int_{r_l}^{r_u} dr \exp(-i\Delta_\kappa r) \times \left[ \frac{\alpha_p \delta_{mm'}}{\tau(r)} + \frac{\exp(i\Delta_m \bar{\theta})}{\tau(r)} \sum_p \hat{I}^0_{p,e} \right], \\
\mathcal{M}^e_{\tilde{\varphi}\tilde{A}_\parallel,\mathbf{k},\mathbf{k}'} &= -\frac{1}{\Delta r} \int_{r_l}^{r_u} dr \exp(-i\Delta_\kappa r) \times \left[ \frac{\exp(i\Delta_m \bar{\theta})}{\tau(r)} \sum_p \hat{I}^1_{p,e} \right], \\
\mathcal{M}^i_{\tilde{A}_\parallel\tilde{A}_\parallel,\mathbf{k},\mathbf{k}'} &= \frac{1}{\Delta r} \int_{r_l}^{r_u} dr \exp(-i\Delta_\kappa r) \times \left[ \exp(i\Delta_m \bar{\theta}) \sum_p \hat{I}^2_{p,i} \right] \\
&\quad - \frac{1}{\Delta r} \int_{r_l}^{r_u} dr \exp(-i\Delta_\kappa r) \times \left( \kappa'^2 + \frac{m'^2}{r^2} \right) \left( \frac{T_i(r)}{q_i^2 N \mu_0} \right), \\
\mathcal{M}^e_{\tilde{A}_\parallel\tilde{A}_\parallel,\mathbf{k},\mathbf{k}'} &= \frac{1}{\Delta r} \int_{r_l}^{r_u} dr \frac{\exp(-i\Delta_\kappa r)}{\tau(r)} \times \left[ \exp(i\Delta_m \bar{\theta}) \sum_p \hat{I}^2_{p,e} \right],
\end{aligned} \tag{2.19}$$

where

$$\hat{I}^l_{p,j} = \frac{1}{\sqrt{2\pi}v^3_{th,j}(r)} \int_{-v_{max,j}(r)}^{v_{max,j}(r)} v^l_{||} dv_{||} \exp\left(-\frac{v^2_{||}}{v^2_{th,j}(r)}\right) \left\{\frac{N^j_1 I^\sigma_{0,j} - N^j_2 I^\sigma_{1,j}}{D^{\sigma,j}_1}\right\}_{p'=p-(m-m')} ,$$

$$I^\sigma_{n,j} = \int_0^{v_{\perp max,j}(r)} v^{2n+1}_\perp dv_\perp \exp\left(-\frac{v^2_\perp}{2v^2_{th,j}(r)}\right) J^2_0(x_{Lj}) J_p(x'^\sigma_{tj}) J_{p'}(x'^\sigma_{tj}) ,$$

The following definitions are introduced: $\epsilon = a/R_0$ is the inverse aspect ratio, $v_{max,j}(r)$ is the upper cutoff speed considered in the numerical implementation, of the species $j$, $v_{\perp max,j}(r) = min(v_{||}/\sqrt{\epsilon}, v_{max,j})$ excludes trapped particles when estimating the $\omega-$ independent perpendicular velocity integrals $I^\sigma_{n,j}$; $\alpha_p = 1 - \sqrt{\epsilon/(1+\epsilon)}$ is the fraction of passing particles; For electrons and ions at their thermal velocity, the drift term in Eq. 2.9 is a small fraction of the typical real frequencies, $k_\theta v_{dz} \sim (1/4)v_{th,i}/a$. For negligible values, the term can be ignored, and paves way for decoupling the parallel and perpendicular velocity integrals and enables numerical tractability. This simplification, used in the existing implementation, significantly improves the runtime. For modes with $\omega_r \sim v_{th,i}/a$, the resultant effect on the eigenvalues maybe expected to be minimal, although the effect is not evident *a-priori*. It will be seen later in Sec.[3.2.6] that this is indeed small for the linear growth rates and the global mode structures. $\hat{I}^l_{p,j}$, are $\omega-$ dependent parallel integrals; $x^\sigma_{tj} = k_\perp \xi_\sigma$, $N^j_1 = \omega - w_{n,j}\left[1 + (\eta_j/2)(v^2_{||}/v^2_{th,j} - 3)\right]$; $N^j_2 = w_{n,j}\eta_j/(2v^2_{th,j})$ and $D^{\sigma,j}_1 =< w_{t,j}(r) > (nq_s - m'(1-p)(\sigma v_{||}/v_{th,j}) - \omega$, where $< w_{t,j}(r) >= v_{th,j}(r)/(rq_s)$ is the average *transit frequency* of the species $j$.

## 2.2 Eigenvalue solution

Numerical solution to the eigenvalue problem Eq. 2.18 is obtained by using Davies method [54, 55]. The method involves evaluating the determinant of the matrix $\mathcal{M}(\mathbf{k}, \omega)$ on a preset, finite number $N$ of test frequencies $\omega$ on the Nyquist curve in the Complex frequency plane $\omega \in \mathbb{C}$. The MPI implementation of the code employs a coupled-domain decomposition scheme involving the test frequency $\omega_l,\ l = 1, 2...N$ and radial wavenumber $k_\rho$. Each MPI rank performs precalculation of the "equilibrium" quantities parallel for a single frequency $\omega_l$. The matrices are then split in blocks corresponding to $\Delta k_\rho$ intervals for a reparallelization with the same MPI processes, with each MPI process calculating matrix elements in its $\Delta k_\rho$ domain. A significant fraction of the compute time is involved in building the matrix elements are independent from the frequency $\omega_l$, hence the parallelization of $\Delta k_\rho$ intervals is very efficient. The coupled-domain decomposition scheme optimizes CPU time by a factor of 10. Details of this scheme, done prior to this thesis, is described in Ref. [55].

As is typical, the compute time scales with size of the matrix. For instabilities involving mainly ion-Larmor scales, such as ITG, the required resolution is relatively less and runtime required was about 30 minutes. However, as described later in Chapters 3-5, a rigorous treatment of the physics of the instabilities relevant to this thesis, in particular the microtearing modes in toroidal geometry turned out to be very demanding. This is due to the dynamics of MTMs being electron dominated but characteristically spanning from ion length scales to meso-scale. For the convergence of these modes, the radial wavenumber spectrum required was found to be nearly $5 \sim 6$ times larger, corresponding to resolutions spanning upto $k_\perp \rho_i \sim 24$. Calculations with such high resolutions increased the required runtime significantly to nearly 10 hours. Consequently, attention was paid to improve numerical performance, details of which is presented in the next section.

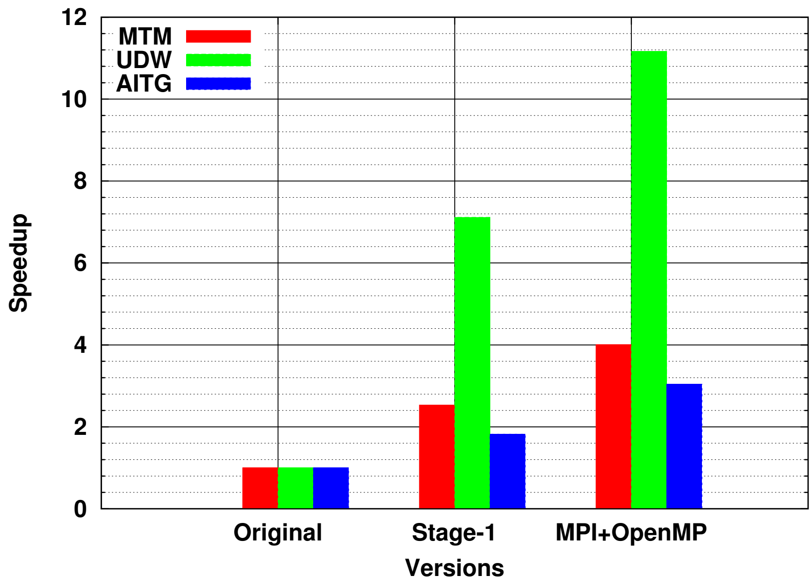


Figure 2.1: The speedup of EM-GLOGYSTO obtained in two stages (i) Stage-1 using LAPACK routines for LU decomposition and (ii) Hybrid MPI-OpenMP parallelization for different microinstabilities - Microtearing Mode (MTM), Universal Drift Wave (UDW) [56] and Alfvén ITG.

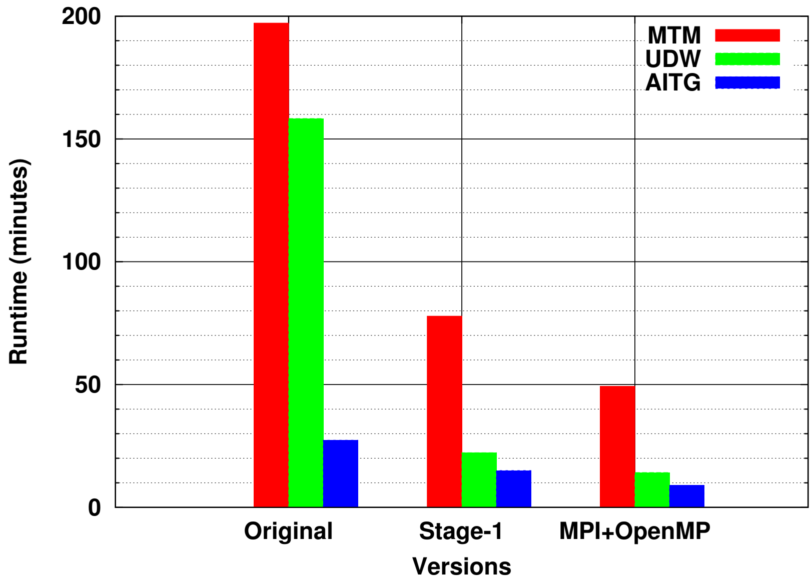


Figure 2.2: Actual runtimes for the test cases in Fig. 2.1.

## 2.3 Numerical Optimization

Profiling the code blocks for the amount of time spent in each block of a code is a primary step towards improving efficiency and runtime. Such an exercise showed that a major portion of the CPU runtime was consumed by two components in the algorithm, for which there was scope for improvements: (a) building the matrix by calculation of the matrix elements and (b) the LU decomposition of the matrices while obtaining the determinant for the Nyquist method. The latter task was performed by the routine ZGEFA from open-source library LINPACK. This legacy package was replaced with routine ZGETRF from another open-source and modern library LAPACK, resulting in a significant speedup. Figs. 2.1 and 2.2 show the improvement of more than 2x (at a rather benign plasma parameter requiring resolution upto $k_\perp \rho_i \sim 8$), labeled as "Stage-1". For further speedup by optimizing the matrix construction, a hybrid-parallelization scheme was necessary, for which GPGPU programming and OpenMP methods provide the alternatives. Considering the complexity of the algorithm, and the large memory requirements than provided by the prevalent GPGPUs, and considering the advantage offered by the shared memory architecture of OpenMP, the latter was chosen. Within the existing algorithm, the matrix is constructed sequentially for the two species in plasma namely ions and electrons as $\mathcal{M}_{\mathbf{k},\omega} = \mathcal{M}^i_{\mathbf{k},\omega} + \mathcal{M}^e_{\mathbf{k},\omega}$. The elements in the ion matrix $\mathcal{M}^i_{\mathbf{k},\omega}$ are independent of those in the electron matrix $\mathcal{M}^e_{\mathbf{k},\omega}$ and hence offers a possibility for domain-decomposition. Thus, using the OpenMP architecture, a second-level parallelization was implemented in matrix construction providing a further speedup of $\sim 1.5$x and resulting in a hybrid MPI-OpenMP code that is able to better utilize the multi-core CPUs in present day HPC infrastructure.

## 2.4 Conclusion

Gyrokinetic formulation of microinstabilities provides an important means to understand the turbulent transport in tokamaks. The 2-D global linear gyrokinetic eigenvalue formulation of EM-GLOGYSTO described in this Chapter provides a mechanism to obtain global mode structures. The eigenvalue problem is solved with the Nyquist method, and all the linearly unstable eigenmodes (i.e. those with $\gamma > 0$)

can be obtained simultaneously. The propagator is constructed analytically as an initial value problem so that the damped modes with $\gamma < 0$ cannot be addressed. The fully gyrokinetic treatment of both ions and electrons considers several kinetic effects, including FLR effects to all orders, transit and precessional drift resonance, Landau and magnetic drift resonances. The numerical improvements to the code in this thesis extends the access to the study of complex microinstabilities occurring at meso-scale. In the following Chapters, the optimized EM-GLOGYSTO is used to study global characteristics of two important electromagnetic microinstabilities namely AITG and Microtearing modes in collisionless regime in large aspect ratio tokamaks.

# Chapter 3

# Passing particle-driven electromagnetic microinstabilities

## 3.1 Introduction

The knowledge and prediction of anomalous transport in Tokamak plasmas is important for control of plasmas in present day Tokamaks and design of future Tokamak reactors. Transport is caused by microturbulence, the rigorous investigation of which has been enabled by the development of gyrokinetic theory. Full scale gyrokinetic turbulence simulations, however, are computationally demanding, resulting in the development of progressively more comprehensive codes over the past three decades. Plasma pressure, characterised by $\beta$ as described in Chapter 1, is an important parameter since it determines the fusion power output and is a parameter in turbulence simulations as well. In the low and negligible $\beta$ limit, magnetic fluctuations can be neglected hence the instabilities in this limit are known as electrostatic instabilities. This results in a significant reduction of the complexity and gyrokinetic simulations have been able to study the ITG turbulence, which is found to account for ion transport (in particular, ion thermal transport) to within an order of magnitude or less of experimentally observed levels. However, hot plasmas are intrinsically at finite $\beta$ and hence electromagnetic simulations are necessary for a realistic account. Magnetic fluctuations bring characteristic changes to the plasma behaviour. For instance, at finite $\beta$, considering a "ballooning angle" formalism, the ITG turbulence has been found to be suppressed by magnetic fluctuations in toroidal geometry [12]. In the formalism, the symmetry properties of the fluctuating potentials is such that $\tilde{\varphi}$ is even and $\tilde{A}_{\|}$ is odd in the ballooning angle (which is directly related to the poloidal angle $\theta$). This set of symmetry is conventionally called as "ballooning parity". Simultaneously, above a certain threshold $\beta$, new instabilities have been found to occur, such as the Kinetic Ballooning Mode (KBM) or Alfvén-ITG, which draws free energy from the ion temperature gradient (similar to the ITG mode) and the Microtearing Mode, which draws free energy from the electron temperature gradient. The Microtearing mode has the opposite symmetry properties, i.e. $\tilde{\varphi}$ is odd and $\tilde{A}_{\|}$ is even, is conventionally called as "tearing parity". Near the mode rational surfaces (MRS), where $k_{\|} = 0$, the even parity of $\tilde{A}_{\|}$ results in the formation of tiny, fluctuating current filaments thereby leading to a local tear of the otherwise smooth magnetic topology. The resulting stochasticization of the equilibrium magnetic fields through this mechanism can lead to large radial electron transport [21].

As described in Chapter 1, early analytic investigations found the collisionless regime, relevant to the hot Tokamaks, to be benign to microtearing instability. Hence, studies of the electron transport channel have focused mainly on the Electron Temperature Gradient (ETG) mode [57] and the Trapped Electron Mode (TEM) [11, 58, 59, 60, 61]. At finite $\beta$, the magnetic fluctuations $\delta B_{\|}$ have a stabilizing influence on the ETG mode [62, 63, 64], whereas TEM is insensitive to the plasma $\beta$ [17]. Of late however, gyrokinetic simulations have found unstable MTMs for parameters of spherical tokamaks such as NSTX and MAST with very high $\beta$ value in collisional or semi-collisional regime [35, 40, 65, 66, 67]. More recently, collisional MTMs with low perpendicular wavenumber ($k_\perp \rho_{Li} < 1$) have been reported for standard tokamaks, such as ASDEX-Upgrade by Doerk *et al.* [45, 46]. The 2-D mode structures from this global simulation finds the electrostatic potential $\tilde{\varphi}$ localized about the mode rational surface while the magnetic vector potential $\tilde{A}_\parallel$ is more extended radially. MTMs have also been reported for weakly collisional Reversed Field Pinch plasmas [44, 68]. These linear gyrokinetic simulations, using a local flux-tube implementation, have thrown light on several characteristics of the mode, typically for high $\beta$ and relatively moderate temperature and electron temperature gradient length scales. The connection to experimentally observed heat fluxes in devices through linear and nonlinear simulations is only beginning to be explored [40, 45, 65, 69]. A strong dependence of the linear growth rate $\gamma$ of these collisional MTMs on electron temperature gradient is now well established [35, 40, 46]. In these works, the linear growth rate has been found to increase monotonically with $\beta$ (typically upto $\sim 12\%$), with some studies finding the mode to be less unstable for higher $\beta$ in spherical tokamaks, whereas the real frequency $\omega_r$ is reported to be only weakly sensitive to the plasma $\beta$ [35, 39]. The instability is found not to be significantly affected by the presence of $B_\parallel$ fluctuations in Spherical Tokamaks [35].

As indicated earlier, the study of microtearing modes has been focused on finite collision frequency regime. Finite collision frequency has been a requirement for the drive mechanisms theorised, namely: (a) parallel thermal force arising from electron temperature gradient, (b) collisional trapping/detrapping of electrons near the trapped-passing boundary leading to enhanced effective collision rate. Recent investigations have found that MTM remains undamped in the absence of collisions in RFP configurations and spherical tokamaks, respectively [39, 44]. Hence it has been envisaged that collisionless drive mechanisms are necessary to sustain these branches of the mode. In the latter work of Ref. [39], magnetic drift resonance of trapped electrons is found to drive the instability in spherical tokamaks. Further, it has been indicated in the work that the same mechanism would be expected to work for large aspect ratio tokamaks as well. However, as is well known, at larger aspect ratios, since the fraction of trapped particles is relatively small, it is pertinent to investigate in detail as to what is dominant drive mechanism for the MTM instability in large aspect ratio tokamaks. Whereas the contribution from both passing and trapped electron dynamics are important for instabilities such as Ion Temperature Gradient mode and Trapped Electron Mode in large aspect ratio tokamaks at finite $\beta$, the work in the present Chapter attempts to delineate some of the issues concerning the collisionless MTM especially pertaining to its drive mechanism and its nature using global gyrokinetic stability analysis in the large aspect ratio limit considering only passing nonadiabatic electrons and ions.

In this Chapter, using EM-GLOGYSTO, the existence of unstable microtearing modes is demonstrated in purely collisionless plasmas in the context of large aspect ratio tokamaks. The $B_{\|}$ fluctuations are typically important at very high $\beta$. However, as will be seen later in Sec. 3.5, collisionless microtearing modes are only marginally sensitive to these fluctuations. Hence, except in Sec. 3.5, $B_{\|}$ fluctuations are neglected in the rest of the studies in this thesis. The following model simplifications enables one to distinguish the effects due to the passing species' dynamics from other possible drive mechanisms: (i) Shafranov shift is neglected, for simplicity. (ii) with a view to gain insight into the possible drive mechanisms, only highly passing electrons and ions are considered and are modelled as fully gyrokinetic. Particles near the trapped-passing boundary [30], as well as trapped particles are neglected. Microtearing modes exhibit even parity in the magnetic vector potential $A_{\|}$, which is related to $j_{\|}$ (see Sec. 2.1). Since the present formulation is completely collisionless, the extent to which the collisional trapping/detrapping and the role of a boundary layer in velocity space play a role in the destabilization can be brought out. Moreover, the fraction of trapped electrons is relatively small at large aspect ratio. Thus the instability of collisionless microtearing modes found in this thesis, is attributed to a drive coming mainly from the non-adiabatic passing electron dynamics.

To contrast with an opposite-parity mode, the 2-D global mode structure of these MTMs is studied and compared with AITG or KBM modes which have ballooning parity. The properties of the modes in both $r$ and $\theta$ directions are resolved. Also, the mode-averaged wavenumbers are found to be large ( $\overline{k}_{\theta}\rho_{Li} \sim 1.7, \overline{k}_{\perp}\rho_{Li} \sim 2.3$) suggesting the necessity for high resolution studies. The mode is Landau damped by electron species and destabilized by magnetic drift resonance of passing electrons. Ions, on the other hand, do not affect the mode seriously. It is shown that the mode requires a high threshold temperature gradient for typical $\beta$ in tokamaks to be unstable, and that the threshold is downshifted at higher $\beta$. A further investigation shows that the electron temperature gradient (quantified by $\eta_e$) drives the mode while the temperature gradient of ion species has very negligible role. For the $\rho^*$ ($\rho/a$, normalized ion radius) value considered, the mode is found to be sensitive to profile variations. Finally a stability diagram in $\beta$-$\eta_{e,i}$ space is presented. Owing to the absence of trapped electrons, this comparison between MTM and AITG modes is to be seen as to only bring out the mode structure related physics. Trapped electrons may further destabilize the mode in two ways: (a) through contribution to the electrostatic potential $\tilde{\varphi}$ [35] (b) through the drift resonance as reported by other authors [39]. Details of this study is presented in Chapter 4.

Section 3.2 contains the various profiles and input parameters used for the study. In the subsequent sections, comparison of the mode structures of collisionless MTMs and co-existing AITG modes and of the various characteristics of these modes brought out by different parameter scans is presented and discussed. Section 3.10 contains the important conclusions.

| Parameters: | Equilibrium Profiles: |
|---|---|
| • B-field : $B_0 = 1.0$ T | • N-profile and T-profile |
| • Temperature : $T_0 \equiv T(s_0) = 7.5\ keV$ | $N(s)/N_0 = \exp\left(-\frac{a\,\delta s_n}{L_n}\tanh\left(\frac{s-s_0}{\delta s_n}\right)\right)$ |
| • Major Radius : $R = 2.0\ m$ | $T_{i,e}(s)/T_0 = \exp\left(-\frac{a\,\delta s_T}{L_T}\tanh\left(\frac{s-s_0}{\delta s_T}\right)\right)$ |
| • Minor Radius : $a = 0.5\ m$ | $\delta s_n = 0.35,\ \delta s_T = 0.2$ |
| • Radius : $0.01 < s < 1.0,\ s_0 = 0.6$ | • $\hat{s} = \frac{s}{q}\frac{dq}{ds}$ |
| $L_n = 0.4\ m,\ L_{T,e,i} = 0.1\ m$ | • $q(s) = q_0 + q_2\ s^2 + q_3\ s^3 + q_4\ s^4$ |
| (thus, $\eta_{i,e}(s_0) = 4.0,\ a/L_T = 5.0$) | $q_0 = 1.25, q_2 = 0.67, q_3 = 2.38, q_4 = -0.06$ |
| • $\tau(s) = \frac{T_e(s)}{T_i(s)} = 1.$ | such that $q(s_0) = 2.0;\ \hat{s}(s_0) = 1.$ |

Table 3.1: Equilibrium profiles and plasma parameters.

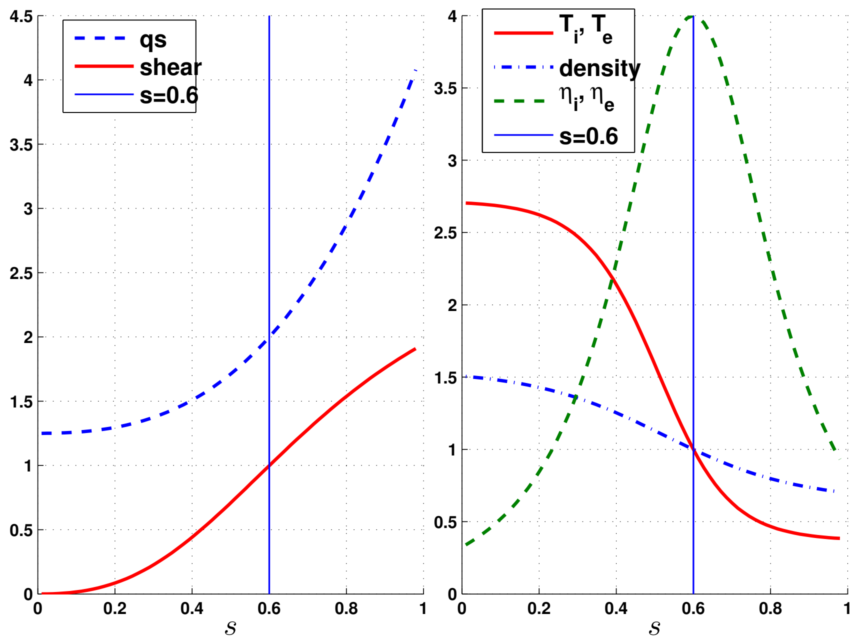


Figure 3.1: Equilibrium profiles for parameters from Table.3.1: Safety factor $q$ and magnetic shear $\hat{s}$ profiles as functions of normalized radius $s$ (left), normalized density, temperature, and $\eta_{i,e}$ (right). $\eta$ peaks at $s_0 = r/a = 0.6$, with $\eta(s_0) = 4.0$

## 3.2 Equilibrium profiles and plasma parameters

Table 3.1 shows the equilibrium profiles and plasma parameters used in this work. The corresponding profiles are plotted in Fig. 3.1. Distances are normalized to minor radius $a$ i.e., $s = r/a$, and velocities to the local thermal velocity $v_{th}$. The radial position where $\eta_j$ peaks is represented as $s = s_0$. The reference plasma density is denoted as $N_0 = N(s_0)$ and is related plasma $\beta_0 = \beta(s_0)$ as:

$$N(s_0) = [\beta_0 B^2(s=0)/(2\mu_0|e|)] \times 1/[T_i + T_e],$$

with temperature $T_j$ in units of $eV$. The potential $\tilde{\varphi}$ is normalized to $T_0 = T(s_0)$, while $\tilde{A}_\parallel$ is normalized to $v_{norm} \sim (e/m)v_{th}$. Frequencies and growth rates are normalized to $v_{th}/a$. With ion and electron temperatures identical, $c_s = v_{th,i}$. Thus, $\omega_0 = c_s/a$. For parameters throughout this Chapter, one has $\omega_0 \simeq 1.7 \times 10^6\ s^{-1}$. Normalized ion-Larmor radius $\rho^*_{s_0} \doteq \varrho_{Li}(s_0)/a \simeq 1/56.5$. For the parameters in Table. 3.1, $N_0 = 8.278 \times 10^{18} m^{-3}$ at $\beta_0 = 5\%$. Thus, typically $2\pi\nu_{ei}/\omega_r \sim 2 \times 10^{-3}$, which, as expected is very small. It is important to note that the calculations reported here are performed in purely collisionless limit i.e. $\nu_{ei} \equiv 0$ [70]. The aspect ratio and equilibrium plasma parameters are chosen to suit a typical large aspect ratio hot tokamak such as KSTAR ($R/a = 3.6$), EAST ($R/a = 4.1$) and SST-1($R/a = 5.1$). For the studies presented in this Chapter, the chosen aspect ratio is 4.0. A range of temperature gradients and $\beta$ typical of H-mode-like plasmas has been used [17, 71, 72, 73]. Studies have been carried out in the range $0.0 < \beta < 0.1$ and $1 < a/L_T < 12.5$ which includes operational regimes of relevance in such tokamaks. The qualitative nature of the modes, including the eigen-mode structures in the poloidal cross-section is found to be similar across the parameter space. A high $\beta$ plasma and a temperature profile with a steep gradient region is considered for representative structures and parameter scans, as MTM draws free energy from this gradient.

The closely spaced mode rational surfaces and the non-adiabaticity of electrons in the thin region near them necessitate a fine resolution over the entire minor radius for convergence. Extensive grid size studies were performed and a convenient grid size which resolves all the different scales sufficiently well is found to be 1586 radial grid points and, 396 radial Fourier modes. A uniform grid spacing is used along the minor radius, resulting in a resolution of about $1.5\varrho_{Le}$ at $s = s_0$. The range of

$v_\parallel$ considered in the parallel velocity integrals is $0 - 5v_{th}$ for each species. A grid density of 16 points per thermal velocity for perpendicular component $v_\perp$ and 20 points for parallel component $v_\parallel$ is used. At this resolution, the relative amplitude of fluctuations at the highest radial wavenumber $k_r$ is $\sim 10^{-3}$ for $\tilde{\varphi}$ and $\sim 10^{-4}$ for $\tilde{A}_\parallel$.

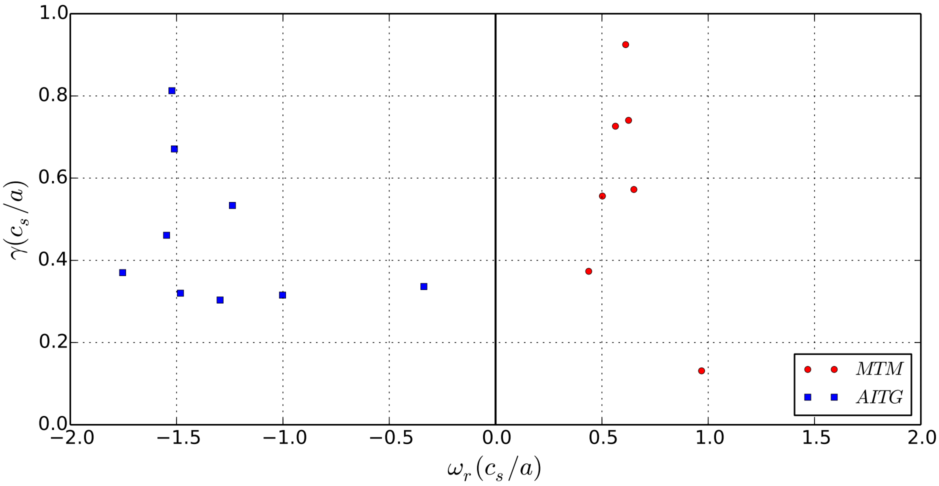


Figure 3.2: Unstable eigenfrequencies of collisionless Microtearing mode and Alfvén-ITG mode in the complex frequency plane for parameters from Table.3.1 and $n = 23, \beta = 5\%$, obtained by Nyquist method. MTMs are in the electron diamagnetic direction with positive real frequency and AITG rotates in the ion direction and has opposite sign for real frequencies.

The dominant and multiple subdominant unstable eigenfrequencies for a given set of equilibrium plasma parameters can be found with the Nyquist method used to solve the eigenvalue problem [49]. Fig. 3.2 shows the many unstable eigenfrequencies of MTM and AITG modes for the used profiles and parameters for $n = 23$. In the following, results obtained for global AITG (or KBM) and global collisionless MTM for exactly the same equilibrium profiles are described, considering the most unstable modes of each type. Wherever possible, qualitative and quantitative comparison of MTM with KBMs are made.

## 3.3 Growth rate spectrum and mode structures of collisionless MTM and AITG

Fig. 3.3 shows the results of a toroidal mode number scan for AITG and MTMs. As described earlier, the scans were performed with $\beta_0 = 5\%$ and temperature gradient length scales corresponding to $a/L_{Tj} = 5,\ j = e, i$ and rest of the parameters as in Table 3.1. In Sec. 3.6, scans for $a/L_T \simeq 1.0 - 12.5$ and $\beta_0 = 1\% - 5\%$ are presented.

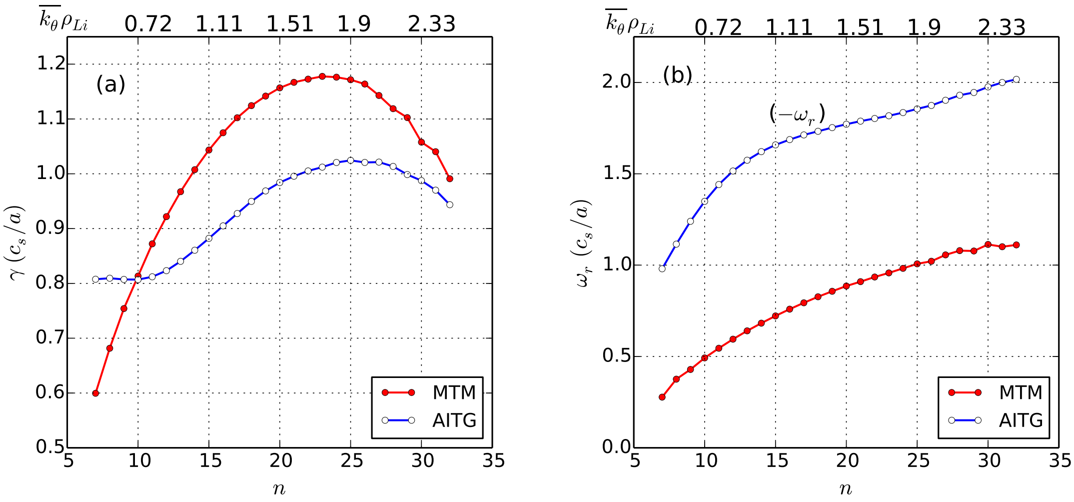


Figure 3.3: (a) Highest growth rates (b) corresponding frequencies for MTM and AITG modes versus toroidal mode number $n$. ($\beta_0$=5%, $\eta_{e,i}$=4). Mode-averaged $\overline{k}_\theta \rho_{Li}$ values are indicated for the corresponding mode numbers on the upper $x$-axis.

Growth rates and real frequencies are plotted as a function of the toroidal mode number $n$ on the lower $x$-axis. As shown in Fig. 3.3(b), note that the MTM mode rotates in the electron diamagnetic direction (positive in our convention) while the AITG mode rotates in the opposite direction, as must be the case. For the equilibrium parameters used here and without trapped electrons, the growth rates for MTM are significantly higher than AITG (nearly 20%), except in very low mode numbers. Interestingly, for both AITG and MTMs, the fastest growing modes are centered around $n = 23$. The upper $x$-axis indicates the mode averaged poloidal wavenumber $\overline{k_\theta}\rho_{Li}$, for the MTM modes $n = 10, 15, .., 30$ where $\rho_{Li} = \rho_{Li}(s_0)$. The mode averaged value $\overline{Q} = \sqrt{< Q^2 >}$ of a quantity $Q$ for any given toroidal mode number $n$ is obtained as follows:

$$< Q^2 >= \frac{\int ds \sum_m |Q\tilde{\varphi}_m(s)|^2 + \int ds \sum_m |Q\tilde{A}_{\|m}(s)|^2}{\int ds \sum_m |\tilde{\varphi}_m(s)|^2 + \int ds \sum_m |\tilde{A}_{\|m}(s)|^2} \tag{3.1}$$

The quantities with suffix $m$ stand for Fourier coefficients of corresponding perturbations. Indeed, the short wavelength modes happen to be more unstable, with $n = 23$ corresponding to $\overline{k_\theta}\rho_{Li} \sim 1.7$. Typically, unstable microtearing modes have been found to have longer wavelengths, with $k_y\rho_{Li} \sim 0.5$ [35, 46, 66]. However, short wavelength modes have been found in spherical tokamaks [38, 39, 74].

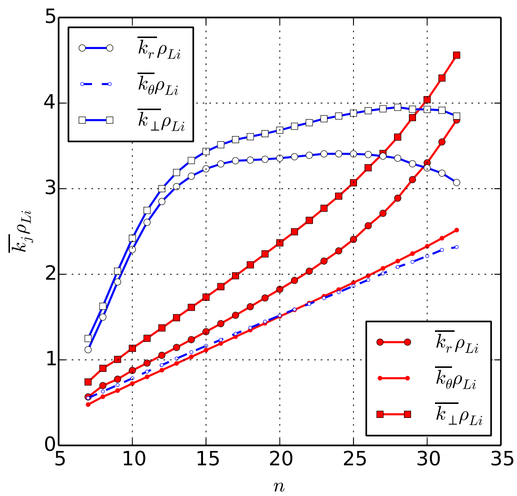


Figure 3.4: Mode - averaged wavenumbers vs toroidal mode number $n$ for MTM (red lines, filled markers) and AITG (blue lines, hollow markers).

Fig. 3.4 shows the different mode-averaged wavenumbers normalized to the ion-Larmor radius, namely $\overline{k_\theta}\rho_{Li}$, $\overline{k_r}\rho_{Li}$ and $\overline{k_\perp}\rho_{Li}$ as a function of the toroidal mode number $n$. The poloidal length scales for MTM and AITG are fairly close, so one may infer that the poloidal dependence is independent of the direction of rotation, unlike the radial dependence. It is further seen that the radial length scales of individual modes are shorter relative to the poloidal length scales, (at $n = 23$, for instance, $\overline{k_r}\rho_{Li} \sim 2.4$ for the MTM while $\overline{k_\theta}\rho_{Li} \sim 1.7$). This is expected as the eigenmodes present sharp radial structures near the mode rational surfaces [18, 19, 16, 75, 76].

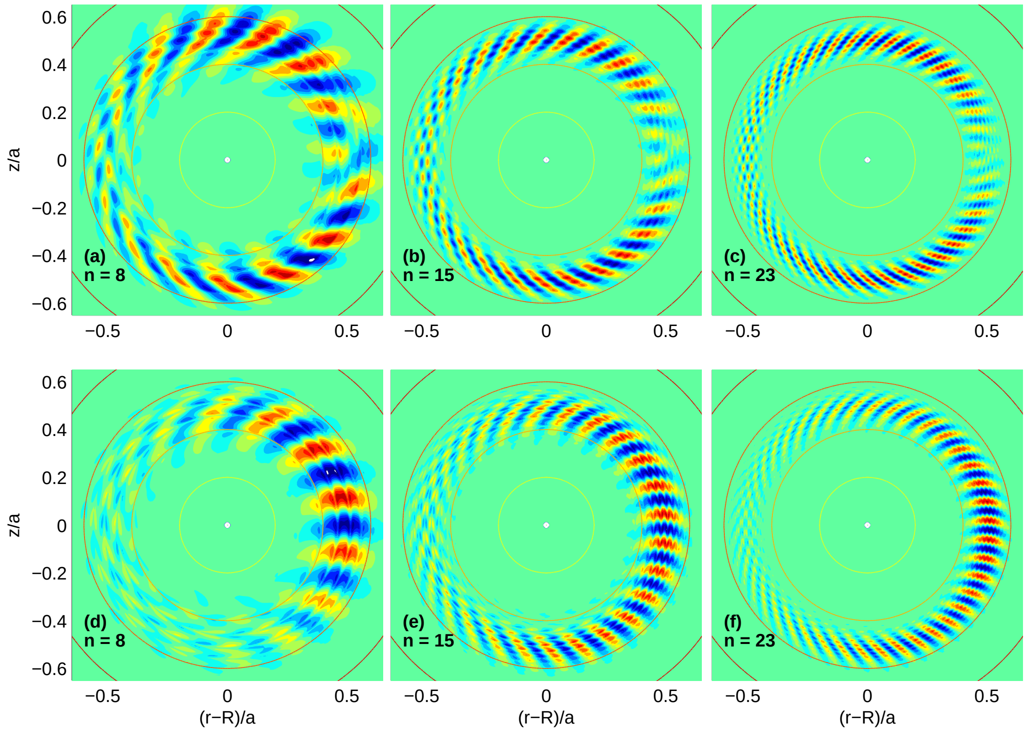


Figure 3.5: Contour plots of Re($\tilde{\varphi}$) for MTM (top row - (a),(b),(c)) and AITG (bottom row - (d),(e),(f)) for the toroidal mode numbers $n = 8, 15$ and 23.

Figs. 3.5- 3.8, upper row plots, show the two-dimensional structures of MTM electrostatic potential fluctuation $\tilde{\varphi} = \tilde{\varphi}(s, \theta)$ and magnetic vector potential $\tilde{A}_{\parallel} = \tilde{A}_{\parallel}(s, \theta)$, respectively, for a set of toroidal mode numbers, viz. $n = 8, 15$ and 23, with 23 being the fastest growing mode. In the lower row, the corresponding mode structures for the AITG instability are shown. Importantly, both the modes are found to be unstable for the same parameters and equilibrium profiles. Moreover, they are co-located in the radial direction. The toroidicity and inhomogeneity of the magnetic field and the resulting magnetic drifts couple several poloidal modes. Consequently, the modes occupy a good portion of the poloidal and radial cross section. In a standard tokamak operation with a monotonic $q$-profile such as the one used in the current study, the mode rational surfaces are very closely spaced. With $\Delta_{MRS} \sim 1/(nq\hat{s})$, the width of the eigen modes span several mode rational surfaces.

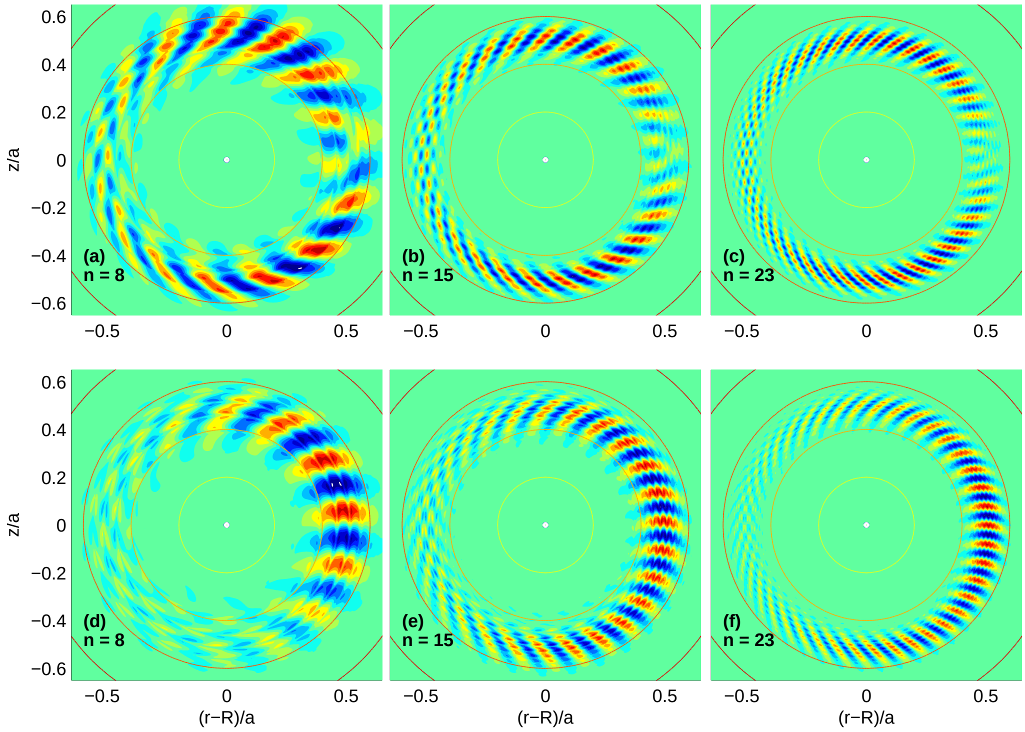


Figure 3.6: Contour plots of Im($\tilde{\varphi}$) for MTM (top row - (a),(b),(c)) and AITG (bottom row - (d),(e),(f)) for the toroidal mode numbers $n = 8, 15$ and 23. The imaginary parts are similar to the real part in nature.

Equilibrium profiles, from which the instabilities draw free energy, vary significantly over the width of these modes, as can be seen from Figs. 3.1, and 3.5- 3.8. As the code is global, the effect of these profile variations is naturally incorporated in the calculation for the whole range of $n$ values and may be important, especially for low-$n$ modes such as $n = 8$. (see Sec. 3.4 for temperature and density profile variation effects). Note that in the poloidal direction, the mode amplitudes show a clear swap - for MTM, the $\tilde{\varphi}$ fluctuations exhibit a dip through $\theta = 0$ midplane ($\theta$ - poloidal angle), whereas that of $A_\parallel$ reach a maximum near $\theta = 0$. This behaviour is more pronounced in the higher mode numbers 15 and 23. In contrast, the AITG potentials exhibit exactly the opposite behavior. In order to understand the nature of $\theta$ dependence more clearly, the potentials $\tilde{\varphi} = \tilde{\varphi}(r, \theta)$ and $\tilde{A}_\parallel = \tilde{A}_\parallel(r, \theta)$ may be averaged and normalized as

$$\bar{\varphi}(\theta) = \frac{1}{a} \frac{\int dr \varphi(r, \theta)}{max(\varphi(\theta))} \tag{3.2}$$

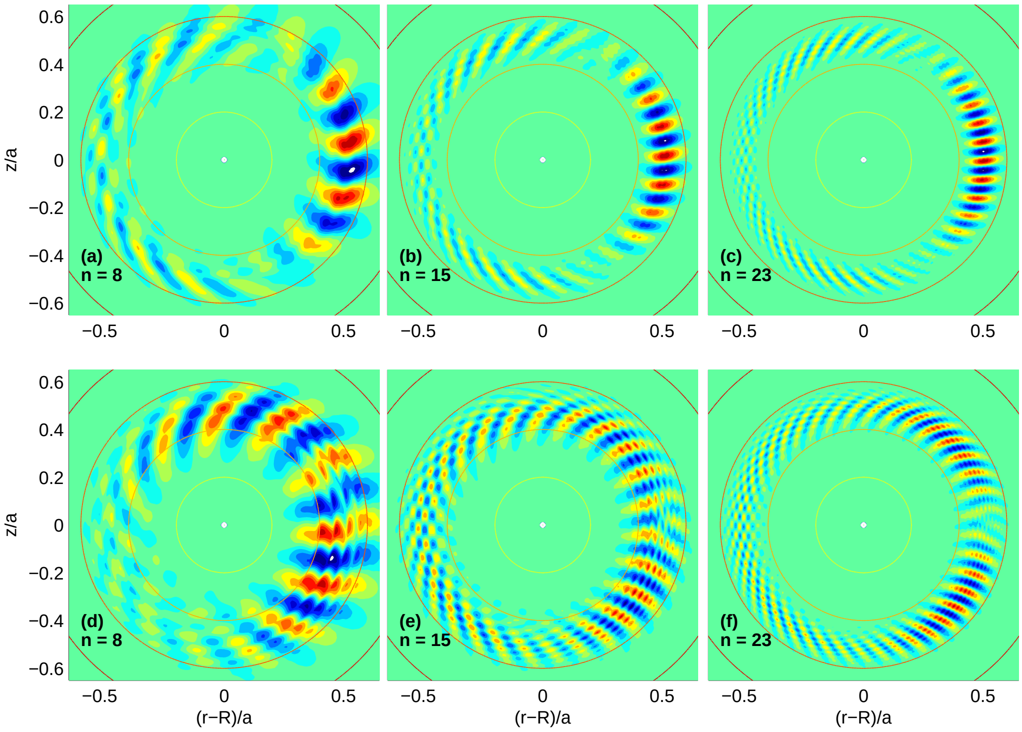


Figure 3.7: Contour plots of Re($\tilde{A}_\parallel$) for MTM (top row - (a),(b),(c)) and AITG (bottom row - (d),(e),(f)) for the toroidal mode numbers $n = 8, 15$ and 23.

to obtain $\bar{\varphi}$ as only a function of $\theta$ and similarly for $\tilde{A}_\parallel$. The resulting functions for the potentials of MTM and AITG from Figs. 3.5 and 3.7 for $n = 23$ mode are plotted in Fig. 3.9, which clearly shows a swap of the envelope of $\tilde{\varphi}$ and $\tilde{A}_\parallel$ amplitudes.

The structures of $\tilde{\varphi}(s, \theta)$ and $\tilde{A}_\parallel(s, \theta)$ in Figs. 3.5 and 3.7 consist of a number of poloidal Fourier components $\tilde{\varphi}(s, m)$ and $\tilde{A}_\parallel(s, m)$ coupled to each other - as it should be for a tokamak equilibrium. In practice nearly 20 poloidal modes are found coupled in well converged results. These individual poloidal modes are plotted in real space in Figs. 3.11 and 3.12. For these plots, $\tilde{\varphi}(s, m)$ is normalized to $\tilde{\varphi}(s, m)|_{max}$ and $\tilde{A}_\parallel(s, m)$ is normalized to $\tilde{A}_\parallel(s, m)|_{max}$, respectively (hereafter denoted $\tilde{\varphi}_m$ and $\tilde{A}_{\parallel m}$. $m$ is the poloidal Fourier mode number) . It is interesting to note that whereas the gradients $\eta_e$ and $\eta_i$ peak at $s = 0.6$, the maxima of the modes are found to be located slightly inwards, near $s = 0.5$. The essential coupling due to toroidal effects are evident from these plots - multiple poloidal modes are seen to have non-zero amplitude at any given radial location $s$, particularly near $s = 0.5$. The modes

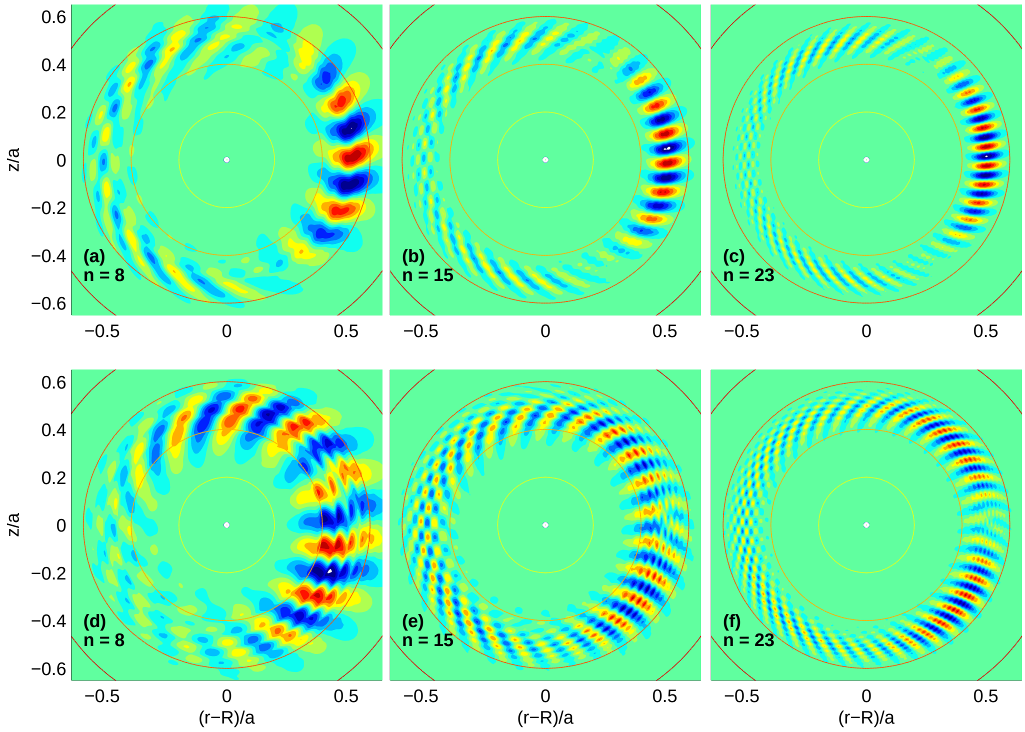


Figure 3.8: Contour plots of $\mathrm{Im}(\tilde{A}_\|)$ for MTM (top row - (a),(b),(c)) and AITG (bottom row - (d),(e),(f)) for the toroidal mode numbers $n = 8, 15$ and 23. The imaginary parts are similar in nature to the real part.

also contain sharp structures close to the mode rational surfaces, where $k_{\|,m,n} = (nq-m)/Rq \simeq 0$ and the phase velocity parallel to the magnetic field $\mathbf{B}_0$ can exceed electron thermal velocity. The non-adiabatic response of the electrons becomes important within a thin layer about these locations and as shown here, can only be captured by the high resolution in Fourier and direct space. This is evident from Figs. 3.13 and 3.14 which show the most dominant poloidal components of MTM (left column) selected from Figs. 3.11 and 3.12 respectively. For comparison, the plots in the right column of the figures are the corresponding poloidal components of AITG (and are not necessarily the most dominant ones).

In Figs. 3.15-3.16, the real and imaginary part of $\tilde{\varphi}_m$ and $\tilde{A}_{\|_m}$ is shown for MTM (top row) and AITG (bottom row) for the fastest growing mode $n = 23$. The imaginary part is similar in nature but are simply negative of the real part. As is clear from Ampère's law, Eq. (2.17), the symmetry properties of $\tilde{\varphi}$ and $\tilde{A}_\|$, resulting in the current density in a 2-D $(r, \theta)$ problem are mathematically related in a similar way in both $r$ and $\theta$ coordinates. For example, for a collisional MTM, it has been shown [35, 46] that $\tilde{\varphi}$ has odd parity and $\tilde{A}_{\|}$ has even parity (tearing parity) in ballooning angle coordinate. Here, in agreement with the Ampère's law, it is seen that for a global collisionless MTM, the tearing parity holds for $\tilde{A}_{\|}$ and odd parity for $\tilde{\varphi}$ in $r$ as well, with respect to the corresponding mode rational surfaces. This is found to be true for each poloidal Fourier component $m$ which together constitute the global structure of MTM. On the other hand, the bottom row shows the opposite symmetries for AITG. Moreover, as noted earlier, the radial width of each component spans several mode rational surfaces, on which the mode interacts with the magnetic drift resonance and transit resonance apart from Landau resonance. The global gyrokinetic formulation for both ions as well as electrons with real electron to ion mass ratio and valid across ion-Larmor to electron-Larmor scale wavelengths captures these important wave-particle resonances realistically, in a large aspect ratio configuration.

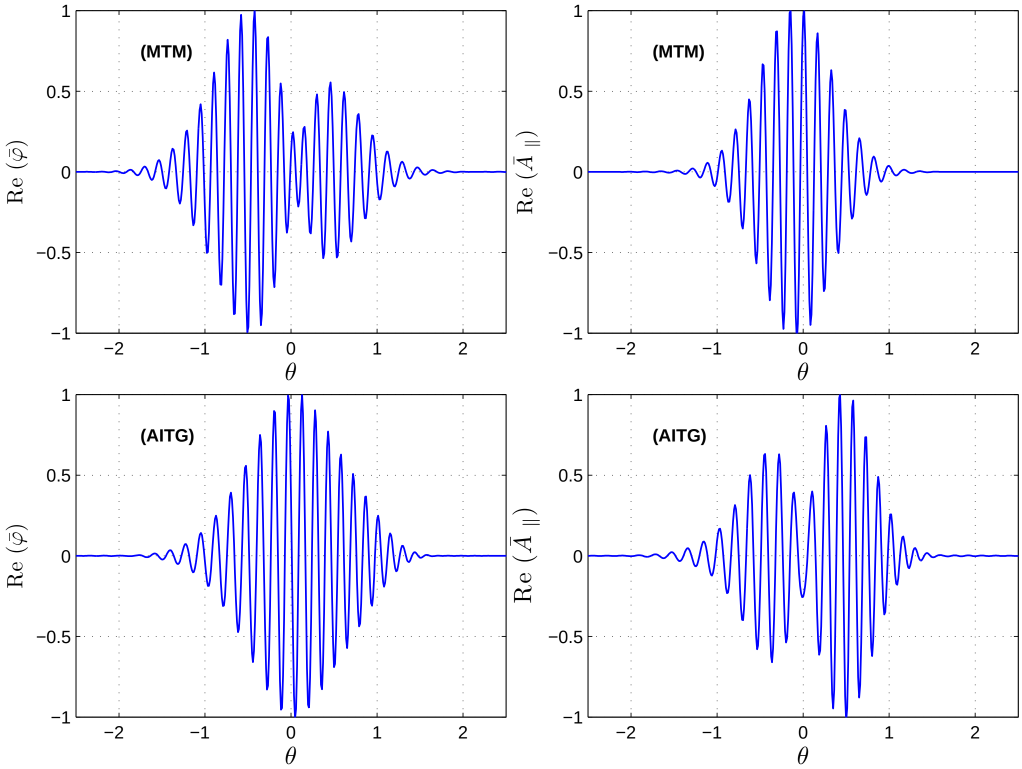


Figure 3.9: Radially integrated plot of Re($\tilde{\varphi}$) and Re($\tilde{A}_{\parallel}$) for MTM and AITG $n = 23$ modes. The imaginary parts also show possess a similar nature, but with opposite sign and is shown in Fig. 3.10.

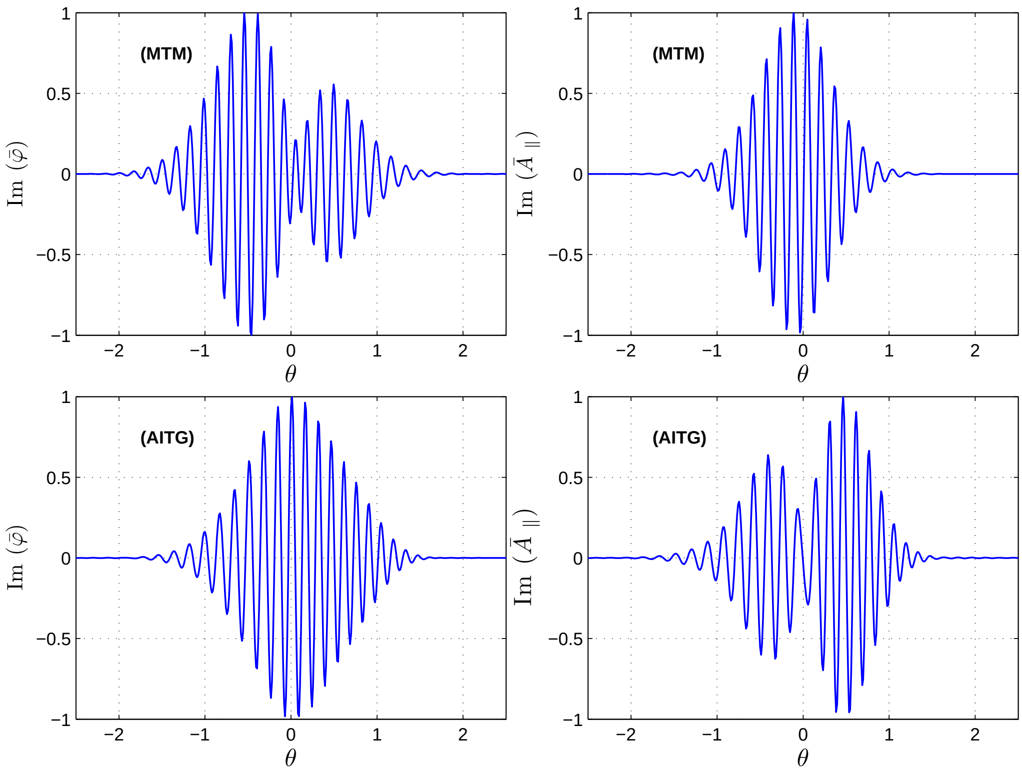


Figure 3.10: Radially integrated plot of Im($\tilde{\varphi}$) and Im($\tilde{A}_{\parallel}$) for MTM and AITG $n = 23$ modes.

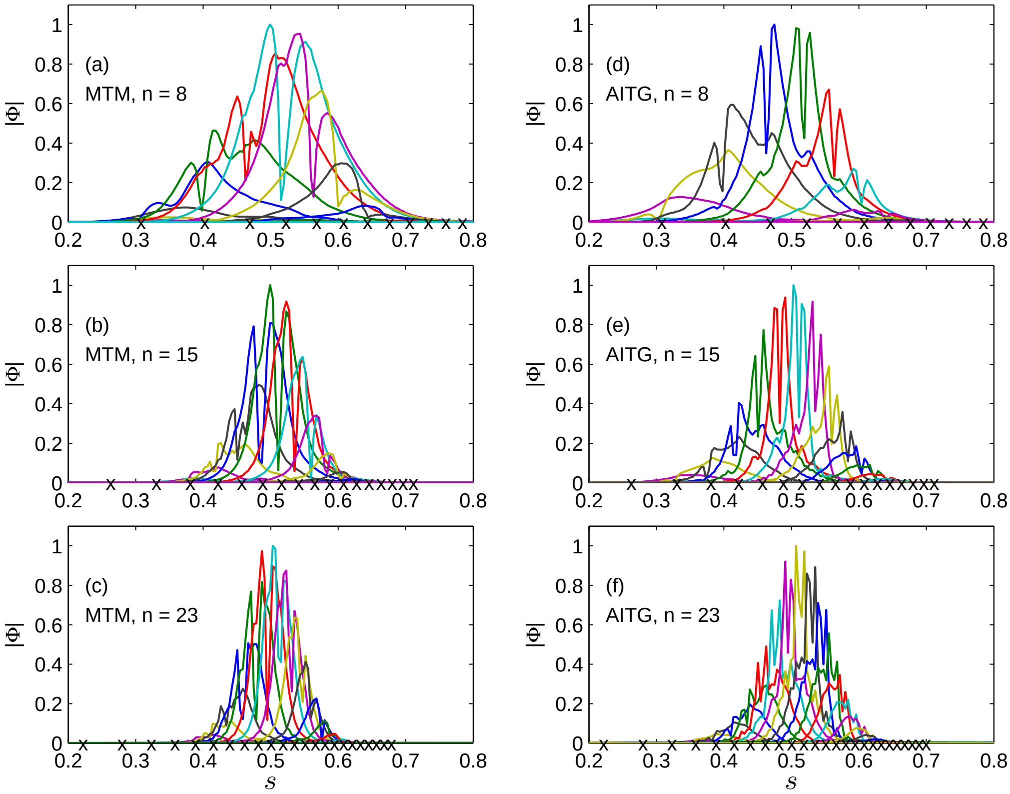


Figure 3.11: Poloidal Fourier modes $\tilde{\varphi}_m$ as a function of normalized minor radius $s$ for toroidal modes $n = 8, 15$ and 23 for MTM (a)-(c) and AITG (d)-(f). The location of MRSs are indicated by markers 'x' on the $x$-axis, at which the corresponding $\tilde{\varphi}_m$ has a sharp dip. (The colors correspond to different modes $m$, but do not correspond to the same $m$ in the right column).

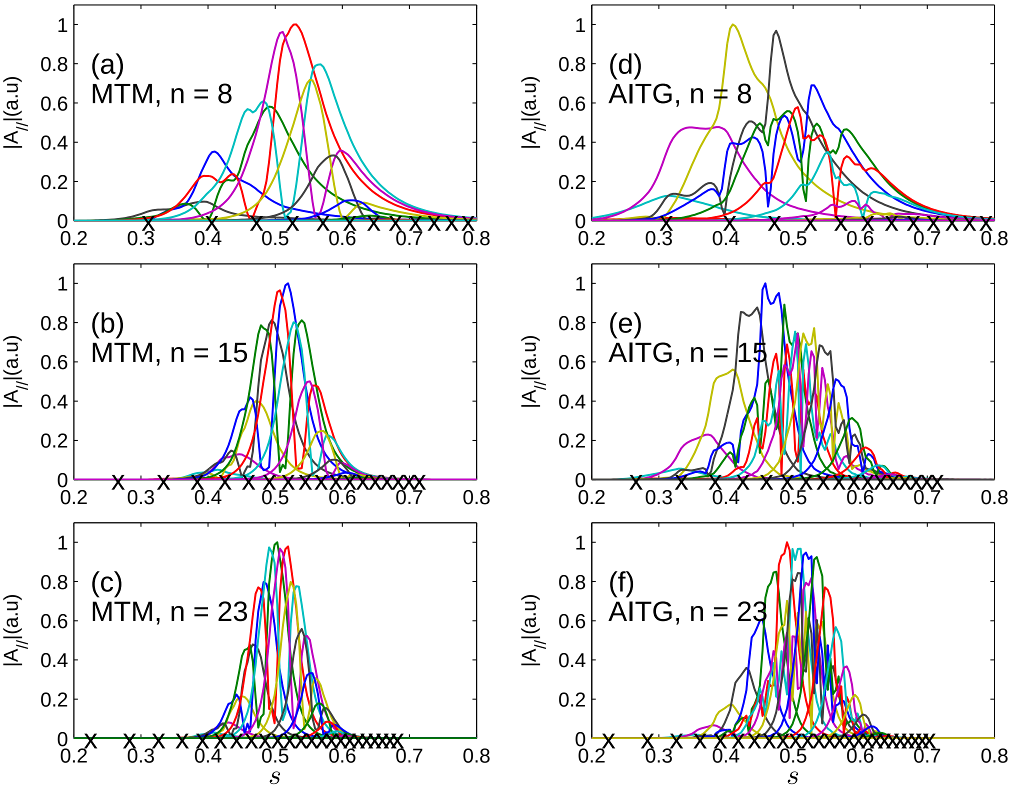




Figure 3.12: Poloidal Fourier modes $\tilde{A}_{\parallel,m}$ as a function of normalized minor radius $s$ for different toroidal modes for MTM (a)-(c) and AITG (d)-(f) shown in Fig. 3.11.

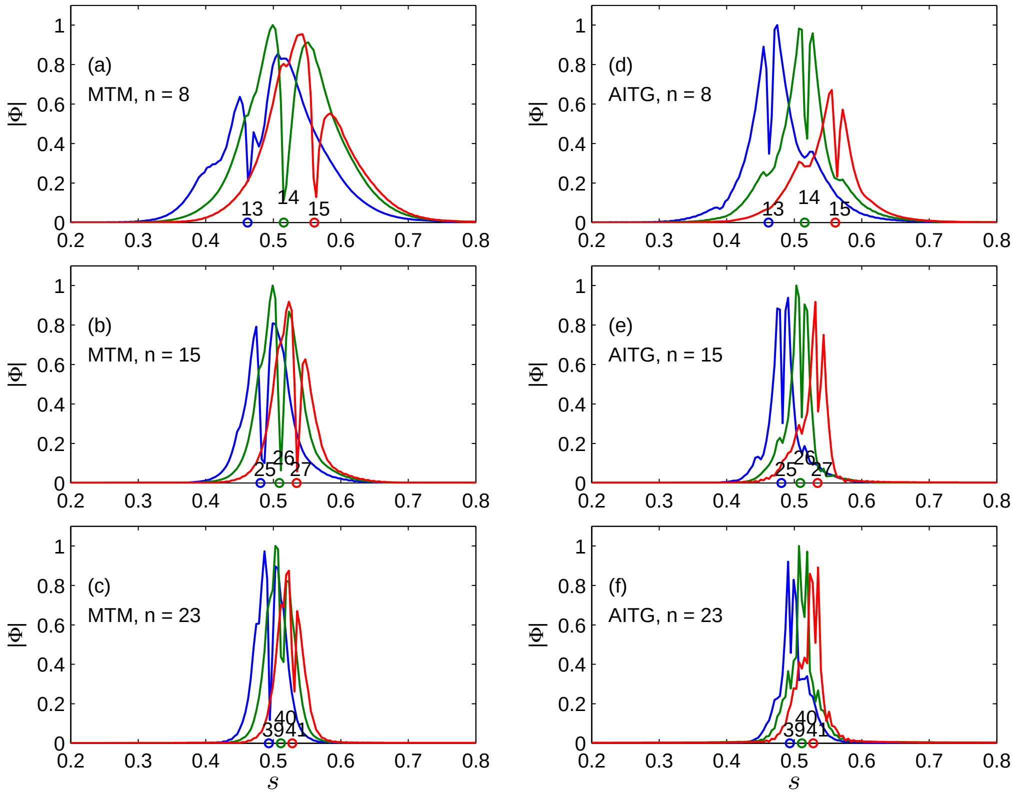


Figure 3.13: Selected dominant modes from Fig.3.11. The circles on the $x$-axis indicate the location of MRSs labeled by $m$. Each mode $(n, m)$ is seen to exhibit sharp dip at the corresponding MRS. (The colors of different modes $m$ in left column is identical to the right column).

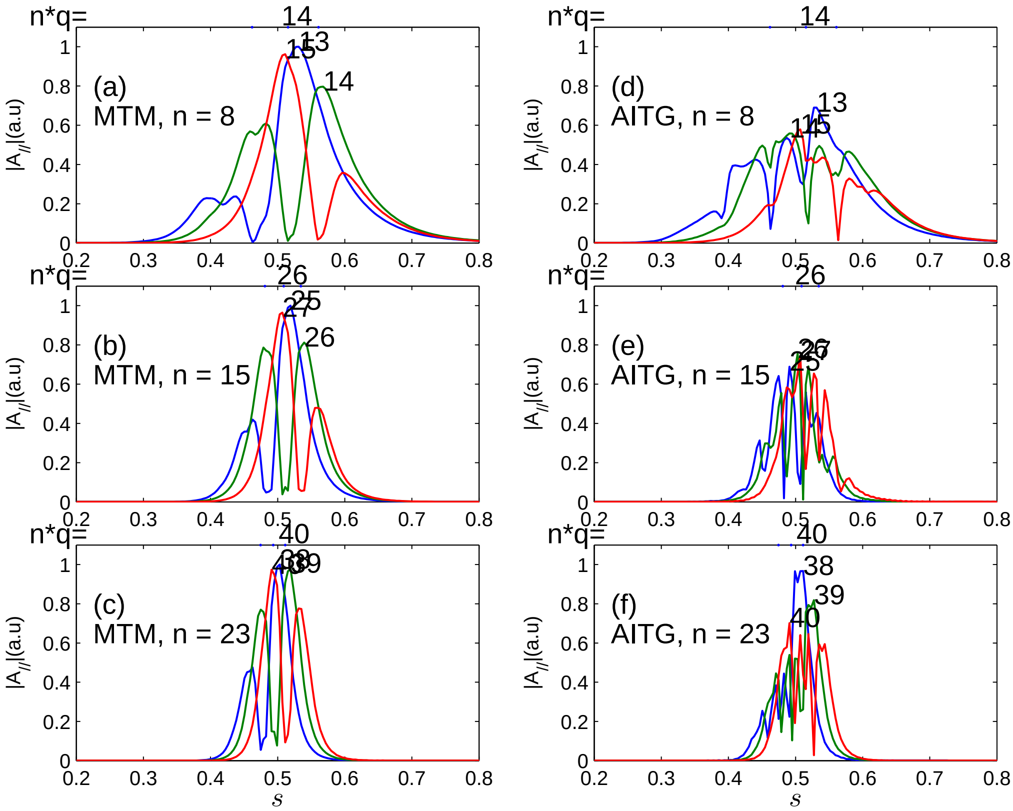


Figure 3.14: Selected dominant modes from Fig.3.12. Each mode $(n, m)$ is seen to exhibit sharp dip at the corresponding MRS. (The colors of different modes $m$ in left column is identical to the right column).

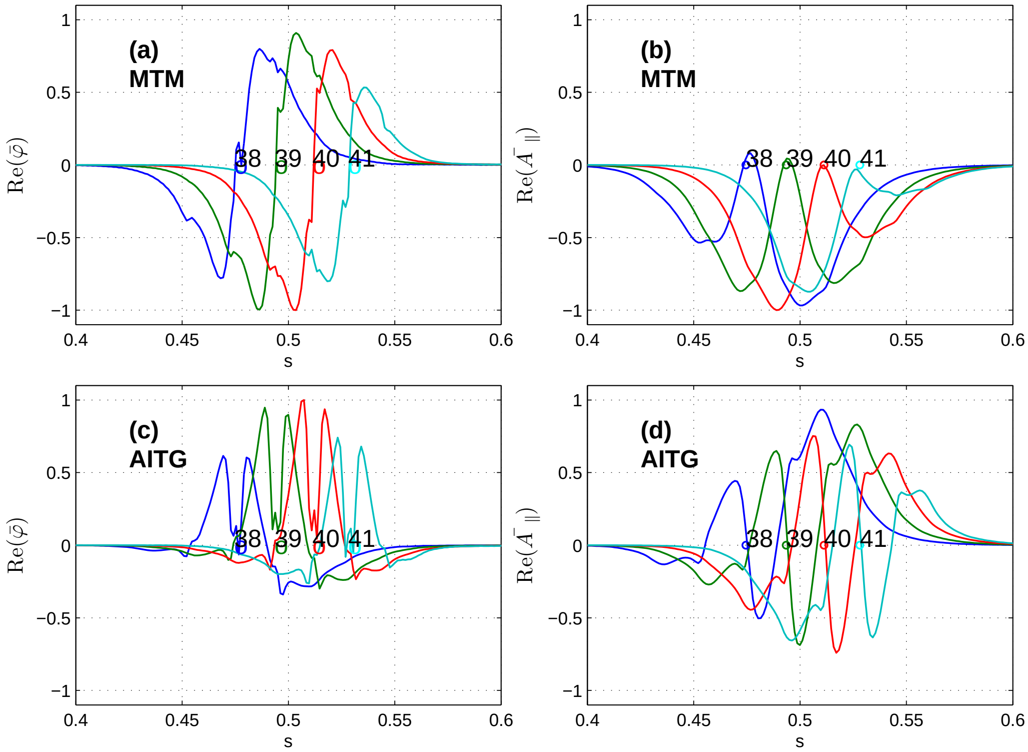


Figure 3.15: Real part of potentials $\tilde{\varphi}$ (left column) and $\tilde{A}_{\parallel}$ (right column) for MTM (top row) and AITG (bottom row). The most dominant poloidal Fourier modes $m$ for $n = 23$ mode in Figs. 3.11, 3.12 are shown. The circles on the $x = 0$-axis labeled by $m$ indicate the location of MRSs. Each poloidal Fourier mode has appropriate parity about its MRS.

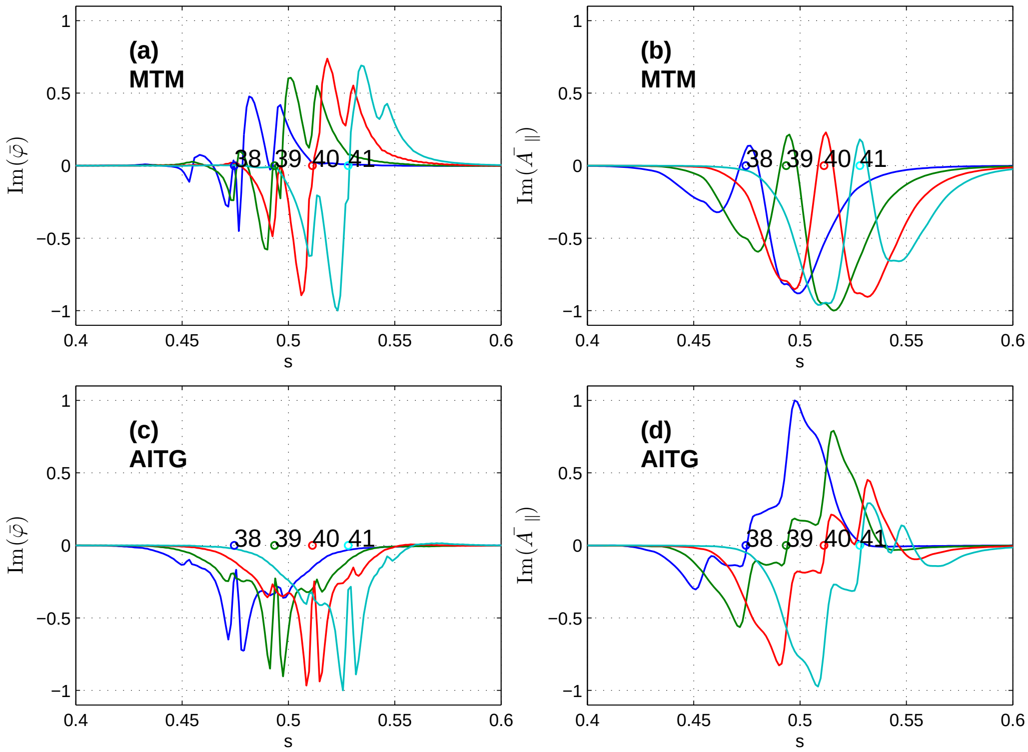


Figure 3.16: Imaginary part of potentials $\tilde{\varphi}$ (left column) and $\tilde{A}_{\parallel}$ (right column) for MTM (top row) and AITG (bottom row). Details are the same as in Fig. 3.15

## 3.4 Sensitivity to temperature and density profiles at finite $\rho^*$

The ratio of ion-Larmor radius $\rho_i$ to the minor radius $a$, denoted as $\rho^*$, characterises the size of the system and is an important parameter in obtaining empirical scaling of transport from Tokamaks of different dimensions. In the limit of small values $\rho^* \to 0$, the equilibrium profiles are nearly constant on the scale of ion-Larmor motion and local analyses can provide efficient account of microinstabilities. Global profile variations important at finite $\rho^*$, however. In the following, the effect of profile variations at finite $\rho^*$ is studied. For the system parameters in this work is $\sim 1/56.5$ using the global analysis. From Figs. 3.5 and 3.7 it is evident that the eigenmode structure spans a width of about $0.2a$, which is significant fraction of the minor radius. Since the equilibrium density and temperature profiles and their gradients vary significantly over this range i.e. the width of the eigenmode, it is of interest to investigate the influence of variation of these profiles on the linear growth rates and global structures of MTM.

The mode draws free energy from the relative logarithmic gradient $\eta$, ($a/L_T$ is seen to be destabilizing, while higher $a/L_n$ is seen to be stabilizing) [66]. By choosing the profile sharpness parameter $\delta s_n = \delta s_T$ ($= \delta s$, say) with the rest of the parameters as in Table 3.1, a constant value of $\eta = 4$ is set over the entire minor radius, so that the free energy source is uniform over the entire range (Fig.3.17(b)). In Fig.3.17 (a),(c) a succession of sharper gradient profiles is depicted, resulting from smaller values of sharpness parameter, all the while maintaining a constant free energy source with $\eta = 4$.

Fig.3.17 (d) shows that the mode width gets reduced as the width parameter $\delta s$ is narrowed, even though $\eta$ is constant through the minor radius. This is also apparent from Fig.3.18 showing the 2-D structures of the eigenmode for $\delta s = 0.05, 0.08, 0.1$

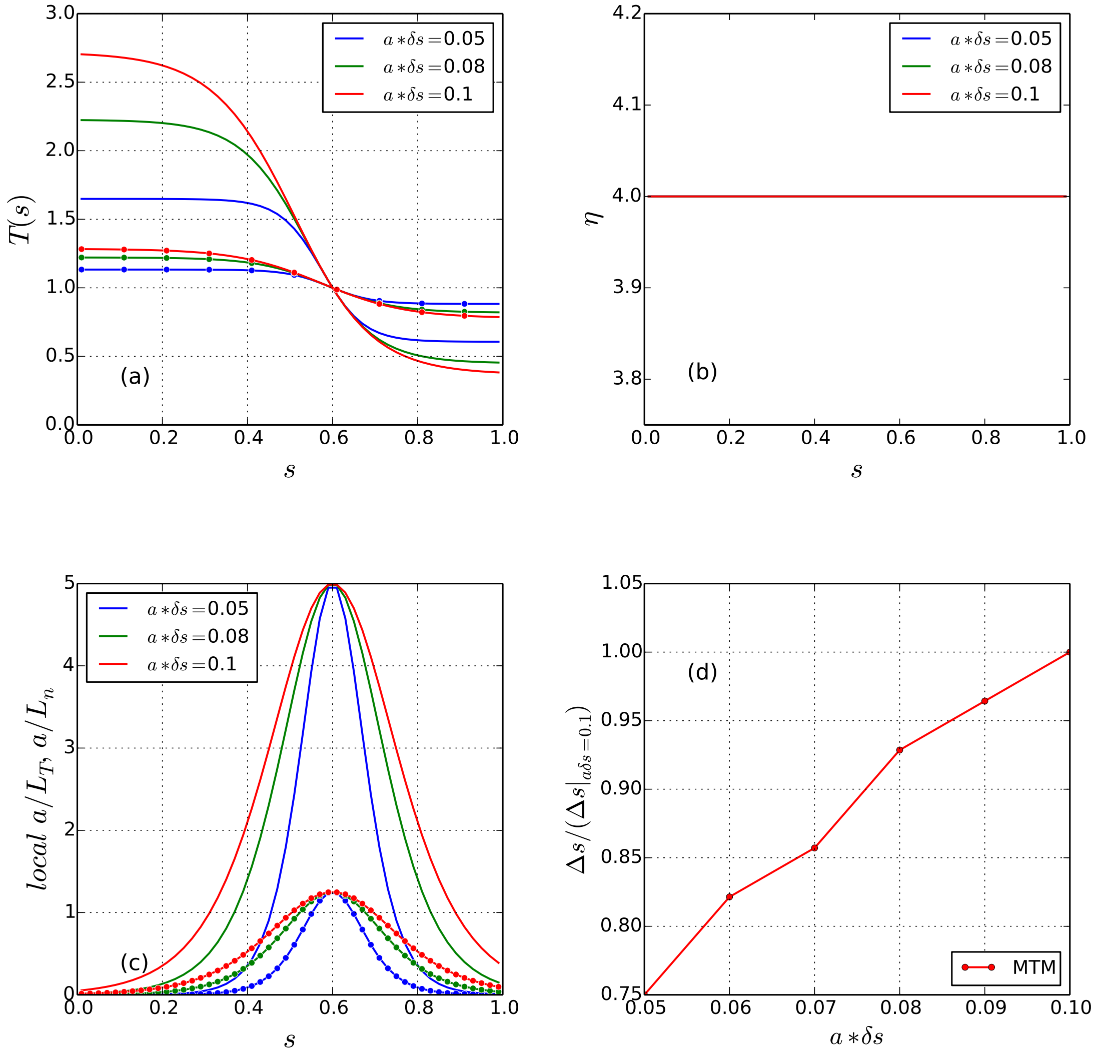


Figure 3.17: Equilibrium profiles of temperature and density for different values of profile sharpness parameter $\delta s$. (a) Temperature (lines), density (with lines-dots). (b) $\eta$ profile corresponding to (a). Note that $\eta = 4$ for the entire minor radius. (c) Logarithmic gradient of temperature (lines) and density (with lines-dots). (d) The resulting radial width of the MTM eigenmode ($n = 23$, $\beta_0 = 5\%$), relative to the width reference unstable mode with $a\delta s = 0.1$ ($\Delta s|_{a\delta s=0.1}) = 0.028$).

(left to right, respectively). This is understood from the fact that the $a/L_T$ profile width narrows, thereby mitigating the peripheral $m$ modes which were previously excited. Consequently, the eigenmode widths also reduce. It may also be noticed that the mode centres closer to $s_0$ at sharper profile variations, whereas the mode is located slightly inwards, as noted before, for broader profiles. Notably, the dominant modes for $\delta s = 0.05$ are $m = 42, 43$, whereas for $\delta s = 0.10$, $m = 38, 39$. The variation

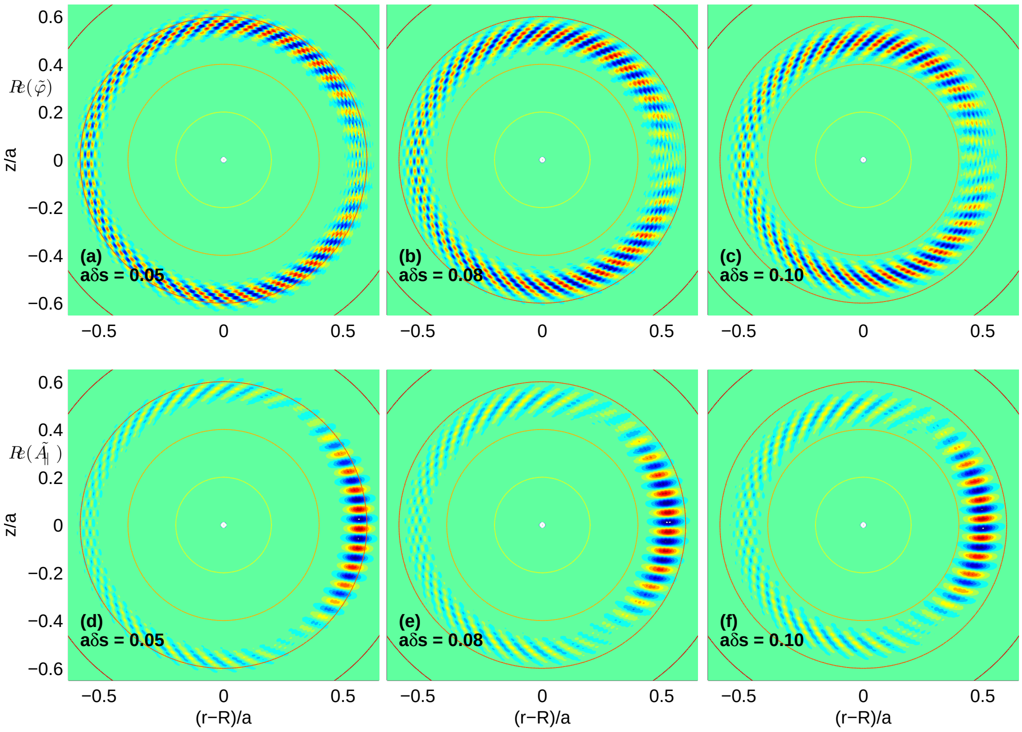


Figure 3.18: Contour plots of Re($\tilde{\varphi}$) (top row (a)-(c)) and Re($\tilde{A}_{\|}$) for MTM (bottom row (d)-(f)) showing change of mode width upon varying $\delta s$, the profile sharpness parameter.

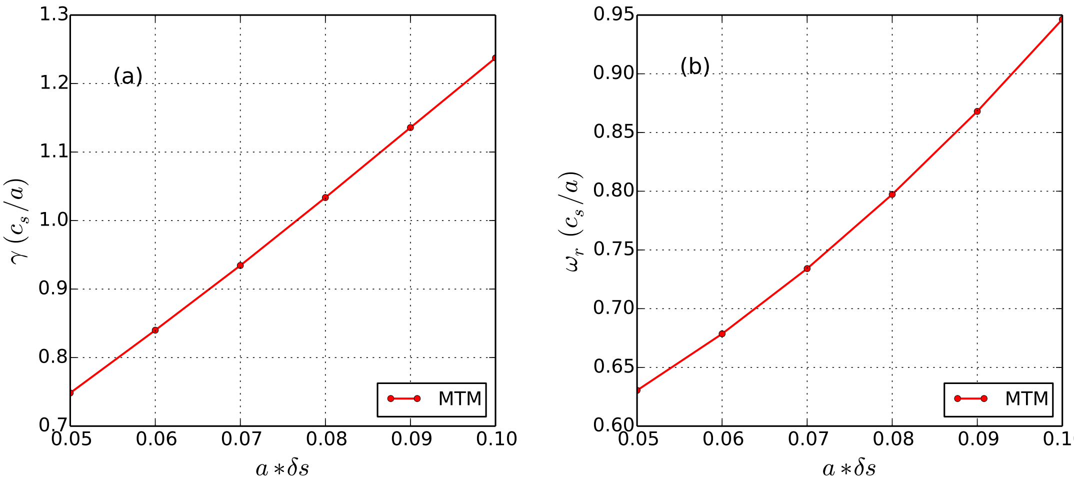


Figure 3.19: MTM ($n = 23$, $\beta_0 = 5\%$) growth rate (a) and real frequency (b) as a function of width parameter $\delta s$.

in the width parameter is observed to strongly influence the linear growth rates and real frequency, as shown in Fig.3.19. The poloidal harmonics $m$ are strongly coupled to each other, due to the toroidicity of the system. Thus the significant reduction in the growth rates is attributed to mitigation of the peripheral $m$ modes.

## 3.5 Dependence on the plasma $\beta$

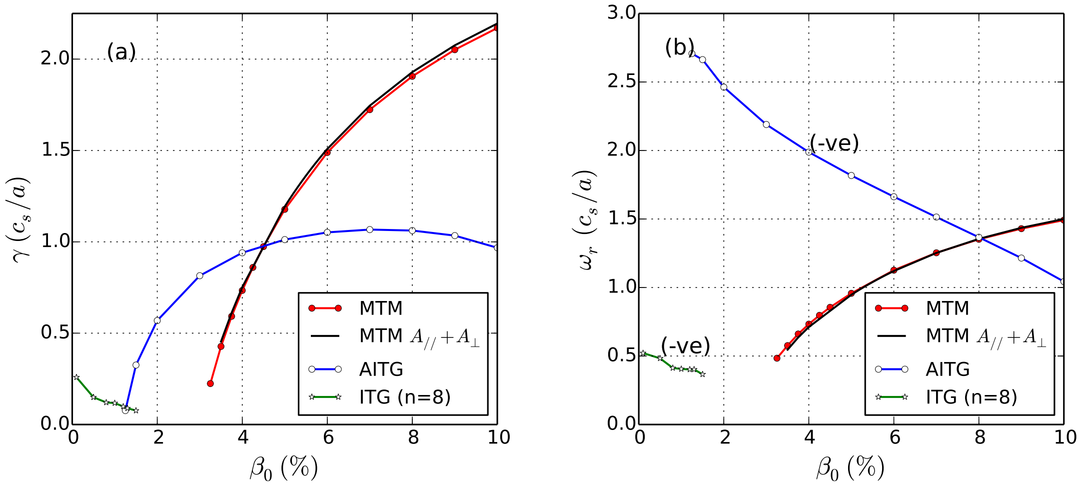


Figure 3.20: Growth rates $\gamma$ and frequencies $\omega_r$ from $\beta$-scan of MTM, AITG and finite-$\beta$ ITG modes for profiles in Fig. 3.1 and $\eta_{e,i}(s_0) = 4,\ n = 23$ (MTM and AITG). For MTM, the inclusion of $B_{\|}$ only marginally affects the growth rates and $\beta$ threshold. For finite-$\beta$ ITG, $n = 8$ is shown which is the fastest growing mode for the equilibrium parameters used.

The plasma $\beta$ is an important figure of merit since fusion power $\propto \beta^2$. Hence a high $\beta$ regime is desired for tokamak operation. However, newer mechanisms of electromagnetic turbulence have been found to be excited at increased $\beta$, such as the AITG. The emergence of such instabilities limits the achievable core temperatures. Thus, $\beta$ scaling of microinstabilities is important to understand the turbulent transport. Fig. 3.20 shows the dependence on $\beta$ of MTMs as well as AITG and ITG modes at finite $\beta$. As mentioned in Sec. 3.2, $\beta$ variation is performed by scaling the normalization density $N_0$. The peak gradient length scales $L_n, L_{Tj}$ as well as the equilibrium profiles and the parameters mentioned in Table 3.1 are kept constant. Thus MHD equilibrium is unchanged. For MTM and AITG, results are for the toroidal mode number $n = 23$, which is the fastest growing mode, while for ITG, the mode studied is $n = 8$, again the fastest growing mode. As can be expected the ITG mode is suppressed at finite $\beta$ - the mode completely stabilises at about $\beta = 1.5\%$. AITG does not retain high growth rates beyond $\beta = 10\%$; after peaking at about 7-8%, [19] the growth rates tend to turn around.

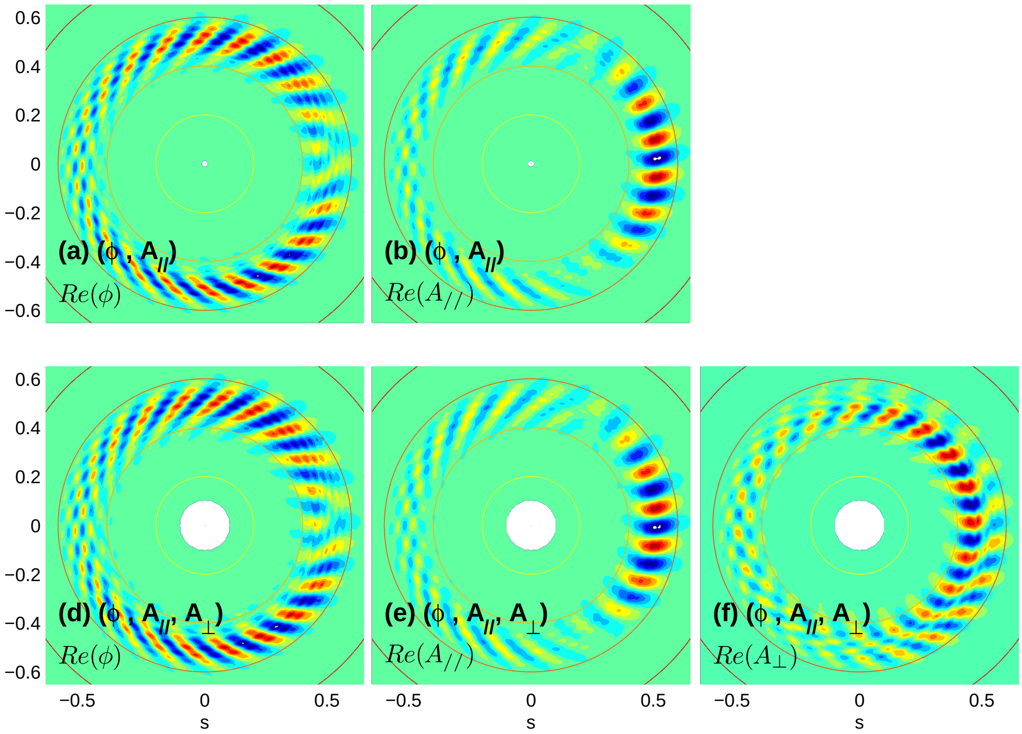


Figure 3.21: (top row) Contour plots of Re($\tilde{\varphi}$) and Re($\tilde{A}_{\|}$), respectively for eigenfunctions obtained without $B_{\|}$ and (bottom row) Re($\tilde{\varphi}$), Re($\tilde{A}_{\|}$) and Re($\tilde{A}_{\perp}$) for eigenfunctions obtained considering all three potentials. Imaginary parts of the components look identical to the real parts shown above.

The onset of MTM for $\eta_{e,i} = 4$, is seen to be at around 2.5% and the growth rate has a strong dependence on $\beta$ - it grows rapidly with $\beta$ and shows no sign of saturation upto about 10%. The inclusion of $B_{\|}$ fluctuations is seen to only marginally affect the growth rates, upto $\beta_0 = 10\%$ and the global mode structures remain unaffected, as shown in Fig. 3.21. Hence, $B_{\|}$ fluctuations are ignored for the other studies undertaken in this thesis. The $\beta$ threshold for the instability is seen to be slightly upshifted, however. (Without considering $\tilde{B}_{\|}$, the $\beta$ - scan upto 40% finds the MTM still growing [Not shown here]). References [66, 68, 69, 77] find a

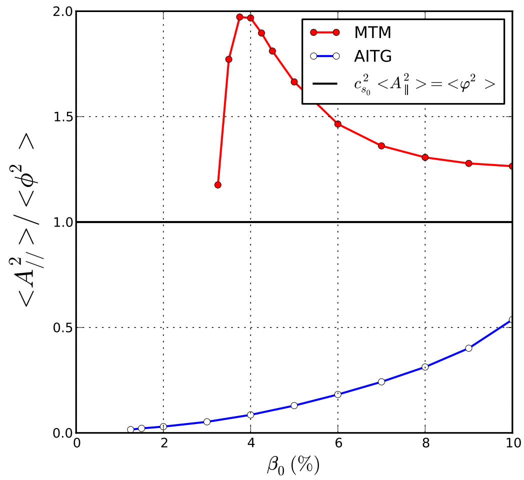


Figure 3.22: Ratio of mode averaged $< A_\parallel^2 >$ and $< \varphi^2 >$ versus $\beta$ for MTM and AITG $n = 23$ modes. Note the strongly electromagnetic nature of MTM (ratio is $> 1$).

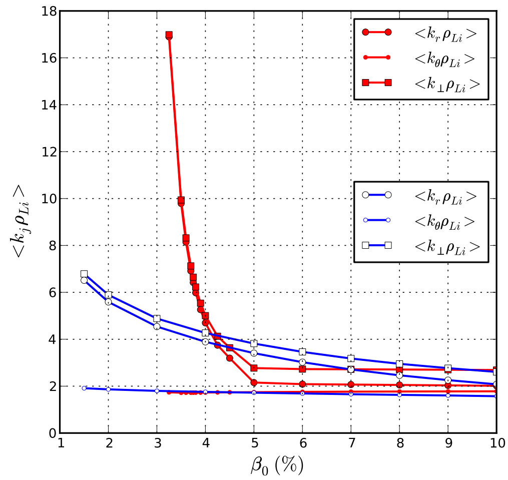


Figure 3.23: Mode averaged perpendicular wavenumbers $\overline{k}_j \rho_{Li}$ vs $\beta$ for MTM (red, filled markers) and AITG $n = 23$ modes (blue, hollow markers).

similar dependence for $\beta \lesssim 12\%$. Interestingly, Refs. [35, 39] find the growth rates decreasing for further higher $\beta$ in spherical tokamaks. The real frequency shows a clear dependence on $\beta$ and grows with $\beta$, in contrast to the very weak dependence seen in earlier works [35, 77]. On the other hand, the real frequencies of AITG and ITG decrease in magnitude.

The relative fluctuation strengths of $\tilde{A}_\parallel$ and $\tilde{\varphi}$ may be obtained as a ratio $< \tilde{A}_\parallel^2 >$ / $< \tilde{\varphi}^2 >$ from the eigen structures as:

$$\frac{< \tilde{A}_\parallel^2 >}{< \tilde{\varphi}^2 >} = \frac{\sum_{k,m} |\tilde{A}_{\parallel(k,m)}|^2}{\sum_{k,m} |\tilde{\varphi}_{(k,m)}|^2},$$

where the subscripts $(k, m)$) are as described before. In Fig. 3.22, the ratio is plotted for AITG and MTMs, establishing the essential electromagnetic nature of both the modes. It is interesting to note that for lower values of $\beta$, for MTM this ratio exhibits a sharp increase, reaches a maximum for $\beta \sim 3.8\%$ and falls monotonically remaining above 1.25 for higher $\beta$ values. On the other hand, for AITG, it increases monotonically for all values of $\beta$. Fig. 3.23 shows the mode averaged $k_\theta$, $k_r$, $k_\perp$ normalized to $\rho_{Li}$ as a function of $\beta$. The $k_r$ spectrum broadens at lower $\beta$, resulting in high mode-averaged normalized perpendicular wavenumbers. The values are in the range of 1.9 to 8 for AITG and 1.9 to 16 for MTM, for the range of $\beta$ values studied, underscoring the necessity of high resolution used here.

## 3.6 Role of temperature gradient

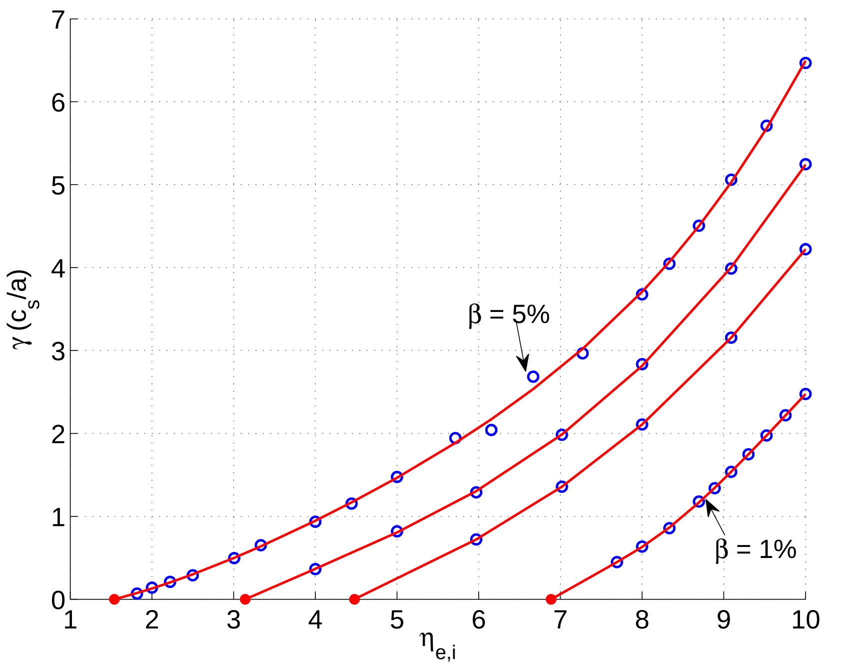


Figure 3.24: MTM growth rates versus $\eta_{e,i}$ at different $\beta$ (5%, 3%, 2%, 1%, ) for $n = 12$. The filled circles at $\gamma = 0$ are extrapolated values which clearly show $\eta_{e,i}^{crit} \propto 1/\beta$.

Fig. 3.24 shows the behaviour of growth rates and real frequencies of the $n = 12$, MTM mode as a function of $\eta_{e,i}$ (meaning $\eta_e$= $\eta_i$). The scans were performed at different $\beta$ values in the range 1% - 5% by keeping the $a$ and $L_n$ fixed at 0.5 and 0.4 respectively, as mentioned in Table 3.1 and appropriately varying $a/L_{Te}, a/L_{Ti}$ simultaneously , in the range 1.0−12.5. The hollow circles correspond to numerically obtained values. The filled circles represent the extrapolated values at $\gamma = 0$ using a

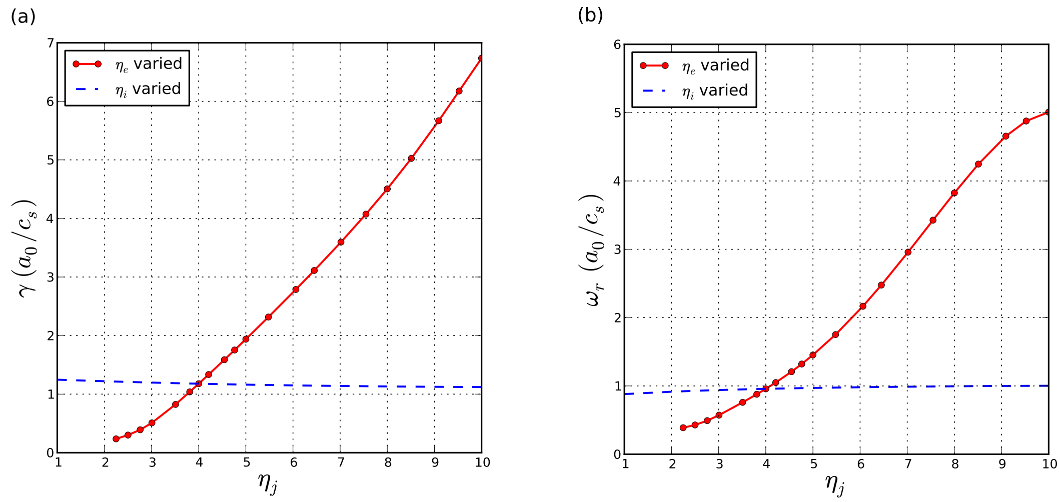


Figure 3.25: MTM growth rates (a) and frequencies (b) versus $\eta_j$, $j = e, i$ for $\beta$=5%, $n = 23$. Separate scans are performed by varying $\eta_e$ keeping $\eta_i = 4$ (red circles) and by varying $\eta_i$ keeping $\eta_e = 4$ (blue dashed lines)

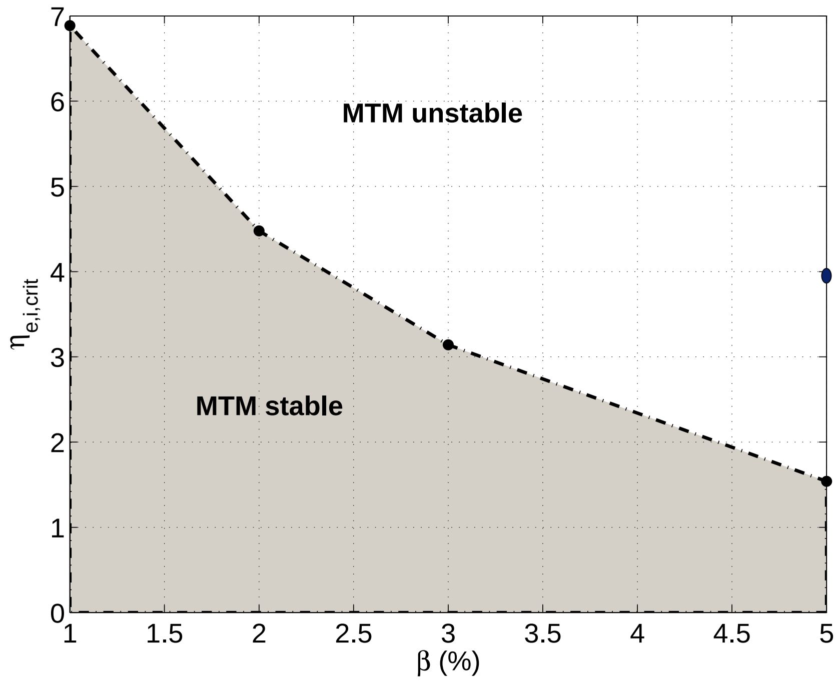


Figure 3.26: Stable and unstable regimes of MTM for parameters in Table.3.1. The mode is stable in the shaded region and unstable in unshaded region. $\eta_{e,i}$ is varied by appropriately varying the value of $L_{Tj}$.

polynomial fit (lines) and represent critical $\eta_{e,i}$. From Fig. 3.24(a), it is clear that for a given $\beta$, the onset of the mode happens only at sufficiently high $\eta_{e,i}$. For example, for $\beta$ of order 5%, MTM appears above $\eta_{e,i}^{crit} \sim 1.5$, whereas at $\beta = 2\%$, $\eta_{e,i} \sim 4.5$

(i.e. $a/L_T \sim 5.6$) in large aspect ratio tokamaks. It would be interesting to study how this threshold is affected with the inclusion of trapped electrons.

A plot of critical $\eta_{e,i}$ values against $\beta$ is shown in Fig. 3.26 using data from Fig. 3.24. This gives an idea of the regime in which MTM is unstable. The shaded region is where MTM is stable, while the white region is where it appears with a positive growth rate. The results of Fig. 3.24 and Fig. 3.26 clearly illustrate the inverse dependence of $\eta_{e,i}^{crit}$ on $\beta$. A similar relation from a study of MTMs in ASDEX-Upgrade has been reported in Ref. [46]. In order to further delineate the effect of $\eta_e$ and $\eta_i$, individual scans are performed by varying $\eta_e$ keeping $\eta_i$ at 4 and vice-versa, while $L_n$ is kept fixed at 0.4 . The results are shown in Fig. 3.25. The scans are performed at $\beta_0 = 5\%$ for the most unstable mode $n = 23$. For the equilibrium profiles used here, it is seen from Fig. 3.25(a) that the growth rate depends strongly on $\eta_e$ and has a critical value of approximately 2.0. However, the dependence on $\eta_i$ is very weak, clearly indicating the electron temperature gradient as the main drive which has been shown to be true for collisional and semicollisional MTMs as well. The real frequency increases almost linearly with $\eta_e$, as expected from the work by Catto *et al.* [30].

## 3.7 Magnetic drift resonance

Early microtearing mode studies considered collisional processes to be necessary to provide a drive for the instability. Recent works, however, have found very weak influence of collision frequency on the microtearing growth rates in low collisionality regimes [39, 44, 46] pointing to the possibility of collisionless mechanisms arising from magnetic drift resonance of electrons providing the drive for the instability [35, 39]. Magnetic drifts lead to the motion of electrons and ions across flux surfaces and accentuate the instability by coupling the different radial and poloidal modes.

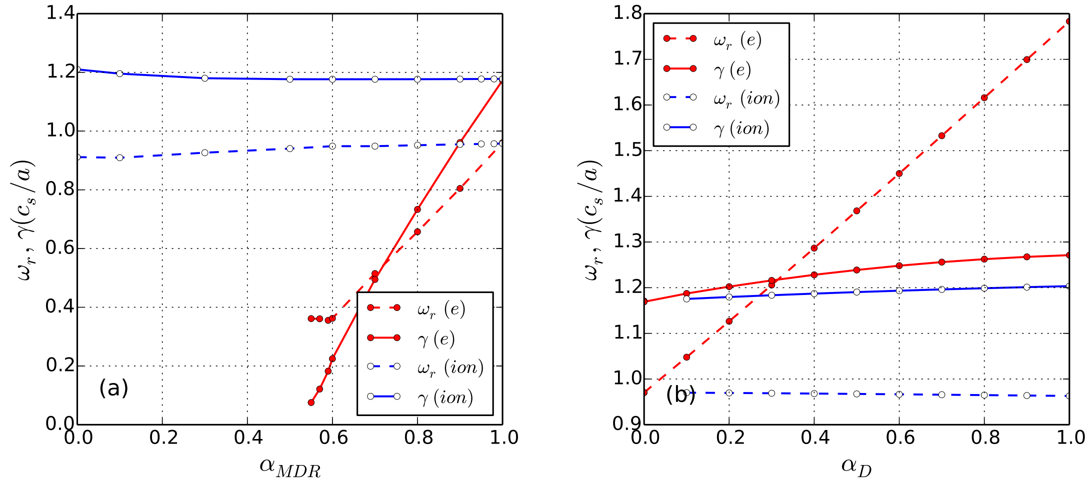


Figure 3.27: Influence of magnetic drift resonance for MTM $n = 23$ mode. Electrons (red, filled circles) strongly destabilize the mode, whereas ions (blue, hollow circles) do not have any effect. In (b), the effect of inclusion of average $k_\theta v_{dz}$ is studied. The real frequency changes by a significant fraction, while the growth rates is not significantly affected by the term.

EM-GLOGYSTO takes into account the resonance due to magnetic drift through the propagator solution, Eq. (2.9), Sec. 2.1:

$$iP = \sum_{p,p'} \frac{J_p(\alpha_{MDR} x_{tj}^{\sigma}) J_{p'}(\alpha_{MDR} x_{tj}^{\sigma})}{\omega + \alpha_D k_\theta v_{dz} - \sigma k_{||} v_{||} - p\omega_t} \exp(i(p-p')(\theta - \bar{\theta}_\sigma)) \tag{3.3}$$

The drift effects appear through the argument ($x_{tj}^{\sigma} = k_\perp v_d/\omega_t$) of Bessel functions $J_p$ and $J_{p'}$ and $k_\theta v_{dz}$ in the denominator. The radial and poloidal coupling would vanish for $v_{dz} = 0$. As noted earlier in this thesis, the parallel and perpendicular velocity are separated for small and negligible values of $k_\theta v_{dz}$, so that $\alpha_D = 0$ in the present version of the code. To study the effect of drift resonance, a weighting factor $\alpha_{MDR}$ is employed in front of $v_{dz}$ (or equivalently, $x_{tj}^{\sigma}$) and numerically scaled from 0 to 1 to obtain the relative importance of the term. The weight factor $\alpha_{MDR}$ for ions is kept at 1 while scaling down that for electrons from 1 to 0 and vice versa. The results are shown in Fig. 3.27 (left). For the electron drifts, below a weight factor of 0.5, the collisionless MTM is stabilized, while ions seem to have no effect. The drift resonance of passing electrons are thus shown to be strongly destabilizing for large aspect ratio tokamaks. The non-adiabatic dynamics of the particles affects the drift resonance through the poloidal component $k_\theta v_{dz}$ as well. The relative effect of this term is studied by setting $k_\theta v_{dz} \simeq \sigma_j(3/2)(m/s)(\rho_j v_{thj})/(aR_0)$, where $\sigma_j$ is the charge of the species. With $\alpha_{MDR} = 1$ for both ions and electrons, the magnitude of this term in the propagator is gradually increased to an approximate velocity-space averaged value by scaling the factor $\alpha_D$ from 0 to 1 separately for ions and electrons as above. It is seen that the ion term has no effect, while the growth rates are only marginally affected by the inclusion of the electron term, although the real frequency is upshifted by a good fraction. The global mode structures are seen not be affected by the change in the real frequency. Hence, the term $k_\theta v_{dz}$ is ignored for the other studies in this thesis. In Ref. [39], Dickinson *et al.* have reported that trapped electrons provide a drive to the instability via the magnetic drift resonance, with the growth rates increasing at larger inverse aspect ratio. The authors also suggest that the drift resonance of trapped electrons could be the driving mechanism for collisionless MTMs in large aspect ratio tokamaks as well. In contrast, it is found here that the magnetic drift resonance of passing electrons is the main drive for collisionless MTM in large aspect ratio tokamaks.

## 3.8 Landau resonance

The formulation used in the code allows one to study the effect of Landau resonance of individual species on the stability of the mode while keeping all other factors unaffected. If the parallel resonance term $k_\parallel v_\parallel$ in the denominator of Eq. (2.9) is replaced with $\alpha_{LD} k_\parallel v_\parallel$ where $\alpha_{LD}$ is simply an artificial multiplying factor, $\alpha_{LD} = 1$ would correspond to properly taking into account Landau resonance while 0 would correspond to no Landau resonance. To investigate electron Landau damping, $\alpha_{LD}$

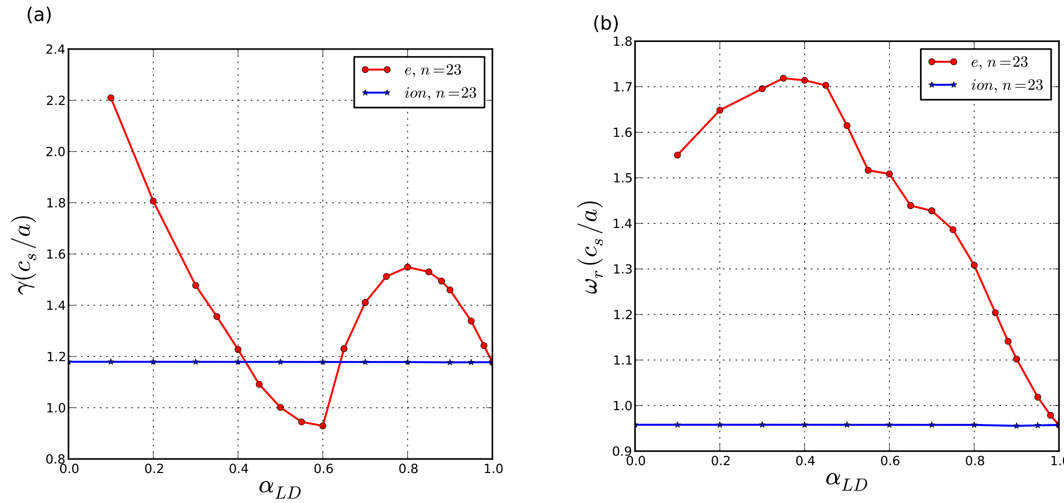


Figure 3.28: Ion and electron Landau damping for fastest growing MTM $n = 23$ mode. (a) Growth rates (b) frequencies.

for electrons is scaled down from 1 while that for ions is set to 1. This procedure helps to maintain numerical continuity to track the roots. Similarly, to investigate ion Landau damping $\alpha_{LD}$ for electrons is set to 1 and that for ions is scaled down. The observations are shown in Fig. 3.28. It is clear that the mode is unaffected by ion resonance. The electron species damps the mode, since the growth rate $\gamma$ at $\alpha_{LD} \simeq 0$ is higher than that at $\alpha_{LD} \simeq 1$, though the behaviour is non-monotonous through intermediate values. This is perhaps due to an interplay with the other resonance term in the denominator of Eq. (2.9) namely the transit frequency and its harmonics. It may be noticed that the change in the trend coincides with a changeover in real frequency too (Fig. 3.28 (b)).

## 3.9 Mixing length transport

The transport due to the microtearing instability is expected due to stochasticization of magnetic fields resulting out of overlapping magnetic islands driven by nonlinearities [21]. Flux-tube calculations [45, 65] have observed that the saturated amplitudes from the non-linear simulations closely follow the predicted values in [21]. In the

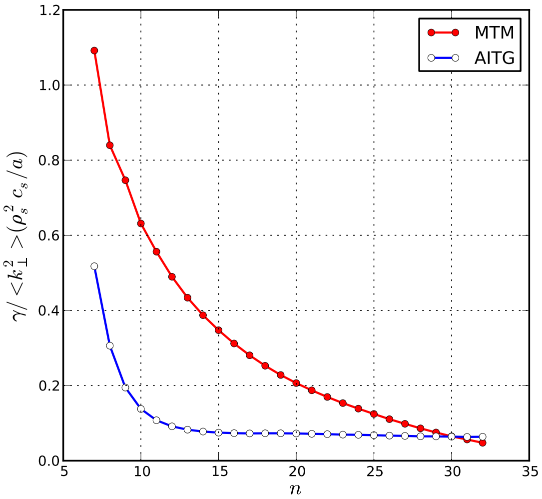


Figure 3.29: Comparison of mixing length estimates for MTM and AITG

following, for comparison from linear growth rates is made for mixing length transport due to MTM and AITG from the global simulations which include passing particle dynamics alone. The transport spectrum obtained from these non-linear simulations show that the electron heat flux peaks at low wavenumbers, coinciding with the linear growth rate spectrum. Fig. 3.29 shows a mixing length estimate obtained from linear growth rates as $\gamma/\overline{k_\perp}^2$, using data from Fig. 3.3(a) and Fig. 3.4. For the present set of parameters, it is noticed that MTM is predicted to have a significantly higher level of transport as compared to that from AITG. The mixing length estimate settles to a relatively low value of 0.1 for the AITG, while MTM has twice the value for $n = 23$ and more for lower mode numbers.

## 3.10 Conclusion

For large aspect ratio, collisionless tokamak plasmas, a high resolution 2D global gyrokinetic stability study of MTM and AITG considering only passing ions and electrons is presented. The trapped electrons are not considered. Linear, full radius, electromagnetic, gyrokinetic calculations show the existence of unstable microtearing modes in purely collisionless, high temperature, large aspect ratio tokamak plasmas. The present study takes into account fully gyrokinetic highly passing ions and electrons. The global 2-D structures of the collisionless mode with full radius coupling of the poloidal modes is obtained and compared with another electromagnetic mode, namely the Alfvén ITG Mode (or Kinetic Ballooning Mode) for the same equilibrium profile. Several important characteristics of the modes are brought out and compared, such as a clear signature in the symmetry properties of the two modes, the plasma - $\beta$ dependence and radial and poloidal length scales of the electrostatic and magnetic vector potential fluctuations. Extensive parameter scans for this collisionless microtearing mode reveal the scaling of the growth rate with $\beta$ and the electron temperature gradient $\eta_e$. Scans at different $\beta$ values show an inverse relationship between the $\eta_e$ threshold and $\beta$, leading to a stability diagram, and implying that the mode might exist at moderate to strong temperature gradients for finite $\beta$ plasmas in large aspect ratio tokamaks. In contrast to small aspect ratio tokamaks where the trapped electron magnetic drift resonance is found to be important, in large aspect ratio tokamaks, a strong destabilization due to the magnetic drift resonance of passing electrons is observed and is identified as a possible collisionless drive mechanism for the collisionless MTM.

The main findings are the following:

- Completely collisionless unstable Microtearing Modes are found in large aspect ratio hot tokamaks in the finite temperature gradient region with a finite-beta plasma for a broad range of relevant parameters. ($\beta \sim 1\% - 5\%$, $a/L_{Te} \sim 1.5 - 12.5$).
- Electron magnetic drift resonance of the passing electron population is shown to be the main destabilizing mechanism. The poloidal component $k_\theta v_{dz}$ of the drift resonance is observed to affect the microtearing instability and mode structures only marginally
- Global 2D mode structures are obtained for MTM. For the same equilibrium

profiles and parameters, co-existing AITG modes are also found and co-located in the radial direction.

- The MTM and AITG modes exhibit appropriate parities. Real and Imaginary parts of $A_{\|}$ of all the poloidal modes which constitute the global mode structure show even parity (tearing parity) about the mode rational surfaces in case of MTM and odd parity in case of AITG. On the other hand, $\tilde{\varphi}$ fluctuations show the opposite parity. $\tilde{\varphi}$ fluctuations of the AITG mode exhibit charge accumulation on MRS, as observed from the sharp structures near the MRSs. This is the first time the radial features of MTM has been brought to the fore, importantly the tearing parity along the radial direction.

- Along the poloidal direction $\hat{\theta}$, a symmetry swap in the $r$-averaged mode structure is observed between MTM and AITG.

- The inclusion of $B_{\|}$ fluctuations is seen to only marginally affect the growth rates, upto $\beta_0 = 10\%$ and the global mode structures remain unaffected.

- Profile variation studies at the system parameters considered, show that the mode structures and the linear growth rate depend strongly on the equilibrium density and temperature gradient width.

- The mode spectrum is characteristically mesoscale, extending to shorter wavelength than the typical ion-scale modes. For example, mode averaged wavenumbers are $\overline{k}_\theta \rho_i \sim 0.75 - 2.5$, $\overline{k}_r \rho_i \sim 0.9 - 3.5$ and $\overline{k}_\perp \rho_i \sim 1.0 - 4.0$.

- Linear growth rates from $n$-scan and $\beta$ - scan for $\eta_{e,i} = 4$ show that if trapped electrons are neglected, MTMs are more unstable than AITG. MTM becomes unstable for $\beta = 3\%$ and the growth rate monotonically increases with $\beta$. The MTM growth rate increases with $\eta_e$ for a given $\eta_i$ whereas for a constant $\eta_e$, variation in $\eta_i$ has minimal effect.

- A clear inverse relationship between $\eta_{e,i}^{crit}$ and $\beta$ is seen. In large aspect ratio machines, at low $\beta$, it can be expected that MTM would become unstable at large $\eta_{e,i}$ and vice-versa, resulting in a stability diagram in the $\beta$-$\eta_{e,i}$ space.

- Real frequency shows a clear and strong dependence on different parameters, including $\beta$ and $\eta_e$ and increases with them. This is in contrast to a nearly constant $\omega_r$ with $\beta$ found by others [35]. The real frequency increases almost linearly with $\eta_e$.

- Mixing length estimates for MTM and AITG show transport due to MTM is likely to far exceed that due to AITG over the full range of the spectrum. Significant transport may be expected lower/median $n$ since typical fluctuation length scales are longer than those of the higher $n$ modes.

- Electron Landau Resonance weakly damps MTM. An interplay with transit resonance harmonics is seen.

- Ion-dynamics is nearly ineffective in Landau resonance and drift resonance.

The studies exploring the linear and nonlinear nature of microtearing modes have been revived recently, spurred by new numerical techniques and the availibility of improved computational resources to resolve both electron and ion scales. It is important to establish the relevance of these modes as an effective means of electron channel of transport. This necessitates further extensive work that includes other effects such as the influence of trapped electrons, the role of equilibrium magnetic shear profiles, coupling to the ETG mode using realistic parameters. The role of non-adiabatic trapped electron dynamics on the microtearing modes is addressed in the next Chapter.

# Chapter 4

# Microtearing modes with non-adiabatic trapped electrons

## 4.1 Introduction

Turbulent electron and ion transport affects the plasma confinement and heating in Tokamaks and limits the achievable core temperatures required for fusion, as described in Chapter 1 [8]. Several plasma parameters, such as the ratio of electron temperature to ion temperature $T_e/T_i$, the density and temperature gradients, the magnetic shear, and the safety factor are found to be important in determining the achievable core temperature and profiles in plasma heating experiments. Despite the disparity between ion and electron mass and consequent dynamics, the hot plasmas in Tokamak are observed to have similar ion and electron temperatures and experimental data suggest similar levels of ion and electron heat fluxes [78]. The perpendicular wavenumber spectrum of these fluxes range from several ion-Larmor radii to ion-Larmor radius or less in standard aspect ratio Tokamaks and to sub ion-Larmor scales in smaller aspect ratio Tokamaks. Thus ion-driven instabilities, which occur at longer wavelengths of a few ion-Larmor radii have been studied extensively.

Gyrokinetic simulations of several ion-driven microinstabilities have been studied, such as the ITG, ITG-TEM and KBM, which are found to contribute to the ion channel of transport.

Understanding electron transport however, has been a challenge and study of electron-driven microinstabilities are in progress. Until recently, electron transport was believed to be caused by the electron-dynamics driven modes, in the presence of equilibrium electron temperature and/or pressure gradients, such as the ETG mode [57] and Trapped Electron Mode (TEM) [3, 17, 79, 80] which have been found to be unstable in Tokamaks and trapped electron-coupled ITG modes [8, 61, 81]. In the presence of electron temperature gradient above a certain threshold, the Electron Temperature Gradient (ETG) mode is unstable. Analogous to the ITG mode which is driven by non-adiabatic ions, the ETG mode is driven by non-adiabatic electrons. The ETG mode occurs at very short length scales of electron-Larmor radii leading to fairly low estimates of transport, except when radially elongated cells, or streamers develop [82]. It is important to here that these modes are ballooning parity modes and do not rupture the magnetic field structure. The ETG mode is stabilized by $B_{\|}$ magnetic fluctuations [17].

In the presence of pressure gradients, the pure Trapped Electron Mode (TEM) becomes unstable due resonance of electrostatic perturbations with the toroidal precessional drift of trapped electrons, so that the mode is unstable at zero $\beta$. The pure TEM is unaffected by magnetic perturbations and remains unstable at finite $\beta$ [17]. In purely collisionless plasmas, the TEM mode is found to be unstable [81], whereas in the presence of collisionality, the TEM mode is stabilized by collisional detrapping of electrons [8]. The TEM occurs at ion-Larmor scales and hence is expected to cause high levels of transport. From theoretical investigations, the relative contribution of these three modes have been found to be different under different experimental conditions of plasma heating [8]. Thus, a clear understanding of the electron channel of transport is still under development.

Microtearing Modes (MTM) have emerged as an important electron-dynamics driven electromagnetic microinstability vis-a-vis transport in recent years [3]. A resurged interest on MTM has been brought about by two recent developments: (i) availibility of fully electromagnetic gyrokinetic formulations to handle inherent multiscale nature required for MTM studies and (ii) "high-performance plasma" experiments (high plasma pressure $\beta$ and large logarithmic temperature gradient length scale $a/L_T$) which allow collisional/semi-collisional regime in Spherical Tokamaks such as MAST and NSTX [35, 40, 65, 66, 67]. MTMs have subsequently been found unstable in a number of other magnetic confinement devices, including Standard Tokamaks and Reversed Field Pinch [44, 45, 46, 68].

Recent electromagnetic gyrokinetic simulations with both passing and trapped electrons have investigated MTMs with collisional drives which sustain parallel current fluctuation $\tilde{j}_{\parallel}$ [35, 40, 65, 66, 67]. Studies of collisional MTM in [35] found magnetic drifts as the main destabilization mechanism, a high $\beta$ and steep temperature gradient as main requirements, rather than the shaping of flux surfaces or large the fraction of trapped particles in Spherical Tokamaks. In contrast, collisionless MTMs were found unstable in Spherical Tokamaks [39], in which a collisionless drive due to the drift resonance of trapped electrons was found to be the main destabilization mechanism for these modes, arising from an asymmetry in the parallel velocity $v_{\parallel}$ integrals for trapped electrons leading to a finite $\tilde{j}_{\parallel}$, which is necessary to sustain the microtearing instability. Using a local flux-tube approach, this study found the MTM to be stable at larger aspect ratios by scaling the inverse aspect ratio parameter, considering a weak collisional drive.

On the other hand, as described in Chapter 3, global gyrokinetic simulations have found the existence of unstable collisionless MTM in large aspect ratio systems [70]. Passing electron dynamics alone is found to be sufficient to destabilize the collisionless MTM in large aspect ratio Tokamaks, with a drive coming from the magnetic drift resonance of passing electrons. In Chapter 3, this was demonstrated by explicitly suppressing the contribution from nonadiabatic trapped electron population. To sum up, while on one hand, weak collisions and trapped electrons are reported to be essential for the MTM mode to be unstable in Spherical Tokamak-like devices [35, 46], there are findings which support that the mode survives in collisionless regimes as well [39, 70]. The nature of MTMs thus appear to have simultaneous dependencies on plasma equilibria, configuration and particle dynamics, with different drives depending on the system parameters.

The Collisionless MTM is envisaged to be a potentially important channel for mesoscale electron transport in the light of its global characteristics as described in Chapter 3. Trapped electrons constitute a significant fraction of the electron population in large aspect ratio as well. Hence, the role of non-adiabatic trapped electrons on the passing electron-driven MTM studied in Chapter 3 is investigated in this Chapter by a systematic inclusion of bounce-averaged contribution of the nonadiabatic trapped electrons to gain insight into the nature of these modes in this Chapter. A comprehensive investigation of the nature of collisionless MTM is performed by including both the passing and trapped electrons to shed light on the contribution of nonadiabatic trapped electrons to the instability. As described in Chapters 2 and 3, the global gyrokinetic code EM-GLOGYSTO models electrostatic and electromagnetic microinstabilities in purely collisionless plasmas based on a global spectral approach valid at arbitrary wavelength, with gyrokinetic ions and electrons, and full electromagnetic fluctuations. The linearized Vlasov-Maxwell equations with fluctuations of electrostatic potential $\tilde{\varphi}$ and magnetic vector potential $\tilde{A}_\parallel, \tilde{A}_\perp$ is closed with Poisson Equation and Ampère's Law. For modes which are ion-Larmor scale or larger, such as the ITG modes, the Poisson Equation is replaced by quasi-neutrality. The parallel magnetic perturbations are found to not affect the MTM instability significantly, as seen in Sec. 3.5, hence $\tilde{B}_\parallel$ fluctuations are not considered. It is well known that the guiding centre of the electrons trapped in the low-field region of the tokamak execute a banana-orbit with a toroidal precession. The banana-orbit averaged non-adiabatic response of these trapped electrons, obtained from the drift kinetic equation, contributes to the electrostatic potential fluctuations. A brief description of the trapped electron formulation is presented in the Chapter 2.

The rest of the Chapter is organised as follows: Section 4.2 describes the various characteristics of collisionless MTMs with and without trapped electrons. Using a drift kinetic model [19, 49], for the equilibrium considered, it is found that at low toroidal mode numbers $n$, the mode is insensitive to the trapped electron dynamics while the growth spectrum of high-$n$ modes are affected significantly. 2-D global mode structure in the poloidal cross-section and characteristics of the linear instability at a given large aspect ratio $A = 4$ is presented. The $\beta$ threshold for the instability is found to be generally downshifted by the inclusion of trapped electrons. Subsequently, in Section 4.3, the MTM instability with and without trapped electrons is studied at different aspect ratios from medium to large values, i.e. $A = 3.0$ to 6.0. The study clearly indicate that at large aspect ratios, the passing electrons contribute predominantly to the drive, and at lower aspect ratios, the contribution from trapped electrons significantly alter the growth rates of collisionless MTMs. Section 4.4 contains the important conclusions.

## 4.2 Role of non-adiabatic trapped electrons at large aspect ratio

General features of Collisionless MTM considering only passing electrons and passing ions discussed in Chapter 3 are as follows: Collisionless MTM is unstable above a threshold $\beta$ and grows more unstable with higher plasma $\beta$ The threshold temperature gradient necessary for the instability is found to be lower at higher plasma $\beta$,and vice-versa. The global mode structure spans several, closely spaced, Mode Rational Surfaces (MRS), has a width of about 20% of the minor radius, and is sensitive to the global temperature and density profiles. For the equilibrium profiles considered (Table 3.1), the linear instability is found to peak at high poloidal wavenumbers $k_\theta$ and . The global mode-averaged values for the most unstable modes are $\overline{k}_\theta \rho_i$ ($\sim 1.5 - 1.9$) [See Eq( 3.1) for definition]. The threshold for the onset of the instability is found to be $\beta_0 \sim 3\%$ for $k_\theta \rho_i \sim 1.7$. The transverse length scale of the fluctuations extends to much shorter scales than ion-Larmor radius, i.e. $\overline{k}_\perp \rho_i \sim 1-4$. Moreover, the span of actual radial wavenumber $k_r$ spectrum necessary to resolve the eigenfunctions of MTM is found to be very broad ranging from ion-Larmor scales to electron-Larmor scales, hence making the mode truly mesoscale. It is found that the required spectrum width is narrower and hence numerically less demanding for modes which are deep into the unstable region [see Fig. 3.26], but closer to the marginal stability boundary, the fluctuation spectrum of these MTMs broadens considerably from ion-Larmor radii to a few electron-Larmor radii scales. Computationally, the $k_r$ spectrum width is a major factor in determining the numerical requirements of the simulation. Moreover, the Nyquist method makes it difficult to obtain eigensolutions closer to the marginal stability boundary (i.e. as $\gamma \to 0$). Consequently, stronger drives are computationally less demanding than near-marginal ones for the study of these MTMs. This is reflected in all the data presented in this Thesis.

In the following Sections, the effect of inclusion of trapped electrons on the growth rate spectrum and mode structures is investigated. The tearing parity of the modes is found to be preserved. An increase in the radial Fourier harmonics is found to be required to resolve the short scales introduced by trapped electrons in $\tilde{\varphi}$. The $\beta$ scaling performed shows that different toroidal modes are likely to have different threshold for instability and is downshifted by the inclusion of trapped electrons. In

Sec. 4.3, the results from an aspect ratio study carried out including the trapped electrons is discussed, followed by Conclusion.

### 4.2.1 Growth rate spectrum and mode structures:

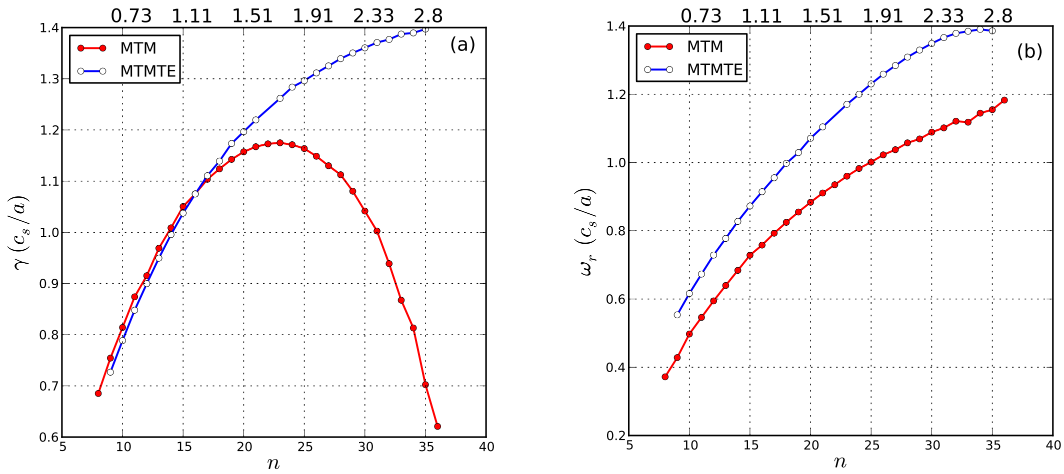


Figure 4.1: (a) Growth rates (b) frequencies for MTM (without trapped electrons) and MTMTE (with trapped electrons) versus toroidal mode number $n$ at $\beta_0 = 5\%$, $\eta = 4$. For mode numbers $n = 10, 15, ...35$, the corresponding mode-averaged $\overline{k}_\theta \rho_{Li}$ values are indicated at on the upper $x$-axis.

Fig. 4.1 shows the growth rate spectrum for the Microtearing Modes. The microtearing mode with only passing electrons is labelled MTM, while the modes with non-adiabatic trapped electrons included are denoted as MTMTE. The contour structure of the fluctuations for these modes with $n = 23$ and $n = 32$ is shown in Fig. 4.2 and Fig. 4.3. The essential tearing parity nature of the mode, as described in Chapter 3 is found to be preserved with the inclusion of trapped electron contribution. The envelope of the $\tilde{\varphi}$ amplitude in Fig. 4.2 and Fig. 4.3 has a minimum at the outboard midplane, i.e. poloidal angle $\theta = 0$. The envelope of the $\tilde{A}_\parallel$ amplitudes, on the other hand, have the opposite nature, i.e a maximum at $\theta = 0$. The real part of the individual poloidal Fourier components of $\tilde{\varphi}$ and $\tilde{A}_\parallel$ are shown in Fig. 4.4. As described earlier in Chapter 3, the toroidal effects couple the differ-

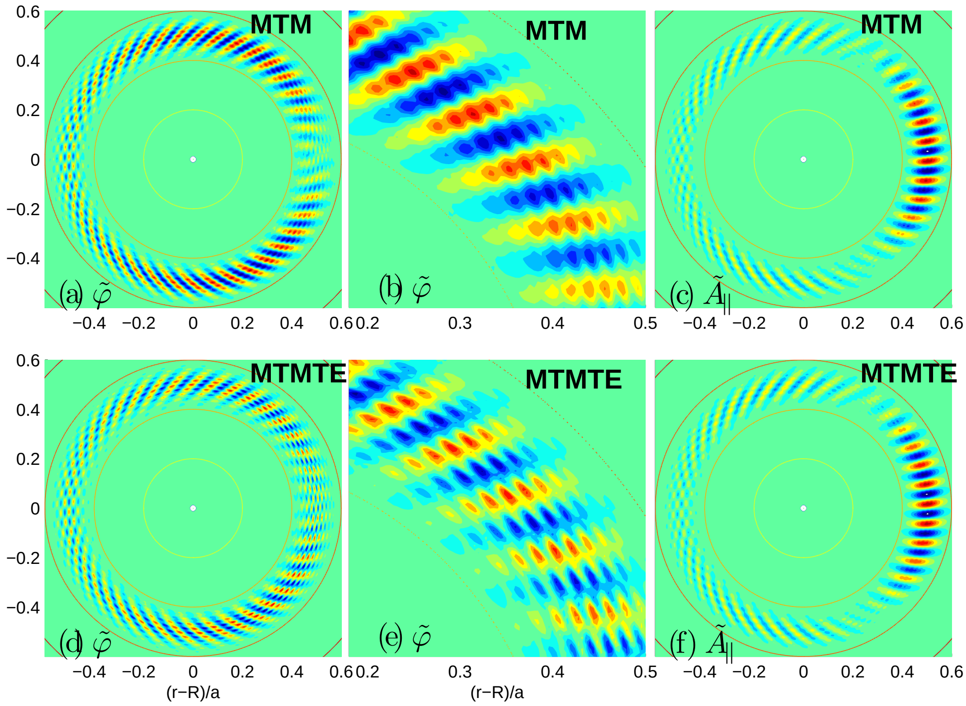


Figure 4.2: Contour plots of Re($\tilde{\varphi}$) and Re($\tilde{A}_{\|}$) for MTM [(a) and (c), respectively] and MTMTE with trapped electrons included [(d) and (f), respectively] for the $n = 23$ toroidal mode at $\beta_0 = 5\%$, $\eta = 4$. A close-up of the Re($\tilde{\varphi}$) contours for MTM in (b) and for MTMTE in (e). The non-adiabatic electrons are seen to create small-scale sharp gradient regions in Re($\tilde{\varphi}$).

ent poloidal components of the perturbation, resulting in extended functions in the radial direction, spanning several mode rational surfaces. Correspondingly, on each MRS, several modes are found to have non-zero amplitude. For MTM in Fig. 3.15 in Chapter 3, each poloidal component was found to have appropriate parity in the radial direction about corresponding MRS. With the inclusion of trapped electrons, whose bounce averaged dynamics do not contribute to $\tilde{A}_{\|}$, such a nature is found to be preserved in $\tilde{A}_{\|}$ structures as well - in Fig. 4.4(d), each poloidal Fourier component is locally even about its corresponding MRS. However, the trapped electrons contribute to $\tilde{\varphi}$ and here in Fig. 4.4(c), it is found that each poloidal component is affected on several mode rational surfaces within its radial extent, in addition to its own MRS. Each of the poloidal Fourier components is seen to be odd-natured about its corresponding MRS and significantly damped in the region near the other MRS.

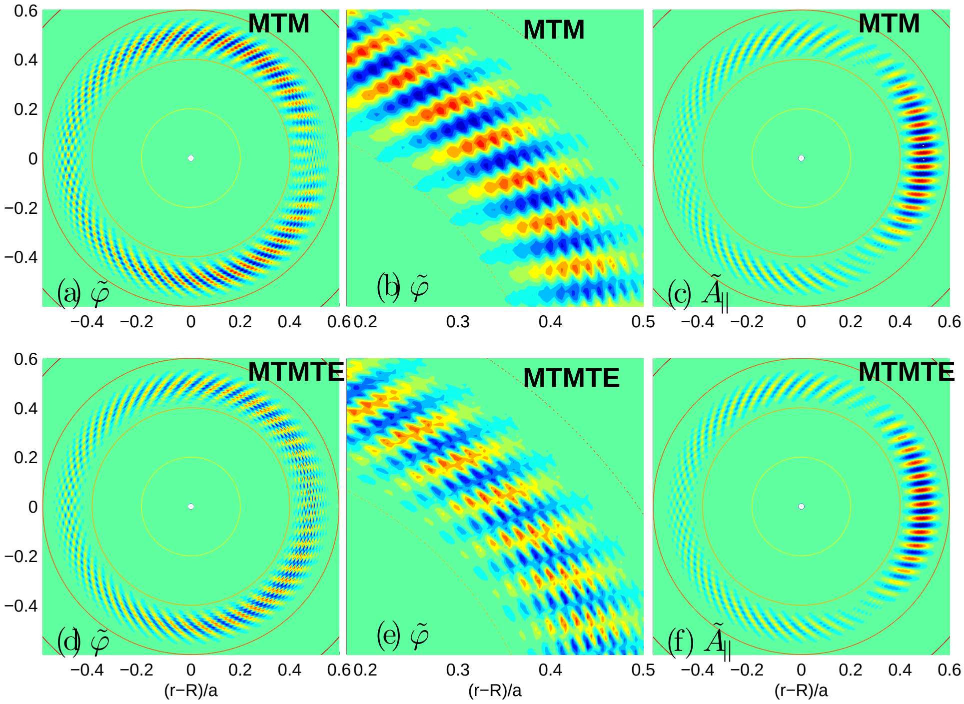


Figure 4.3: Contour plots of Re($\tilde{\varphi}$) and Re($\tilde{A}_{\|}$) for MTM [(a) and (c), respectively] and MTMTE with trapped electrons included [(d) and (f), respectively] for the $n = 32$ toroidal mode at $\beta_0 = 5\%$, $\eta = 4$.

The linear growth rates for MTM at $\beta_0 = 5\%$ is found to bear a peaked structure dependence on toroidal mode number $n$ with a peak $\gamma$ at $n = 23$, as seen earlier in Chapter 3. This can be understood in the following way. For higher $n$ values, the growth rates reduce due to the Finite Larmor Radius (FLR) stabilization. At lower $n$, the perturbation wavelengths are much longer than Larmor radii leading to lesser growth rates. All the plasma parameters being identical, the mode number $n$ at which growth rate typically peaks is determined by the gradient scale lengths - at higher $a/L_T$ the spectrum peaks at relatively higher $n$.

The non-adiabatic trapped electron contributions couple via electrostatic potential fluctuations $\tilde{\varphi}$ which adds to the destabilization. In fact, previous studies have reported that $\tilde{\varphi}$ is destabilising [35]. The trapped electron drive appears ineffective at the lower toroidal mode numbers $n = 10 \sim 20$. However, the growth rates are significantly higher due to trapped electron dynamics at shorter scales of $n \gtrsim 25$. The contribution of the trapped electrons to the instability comes via the resonant

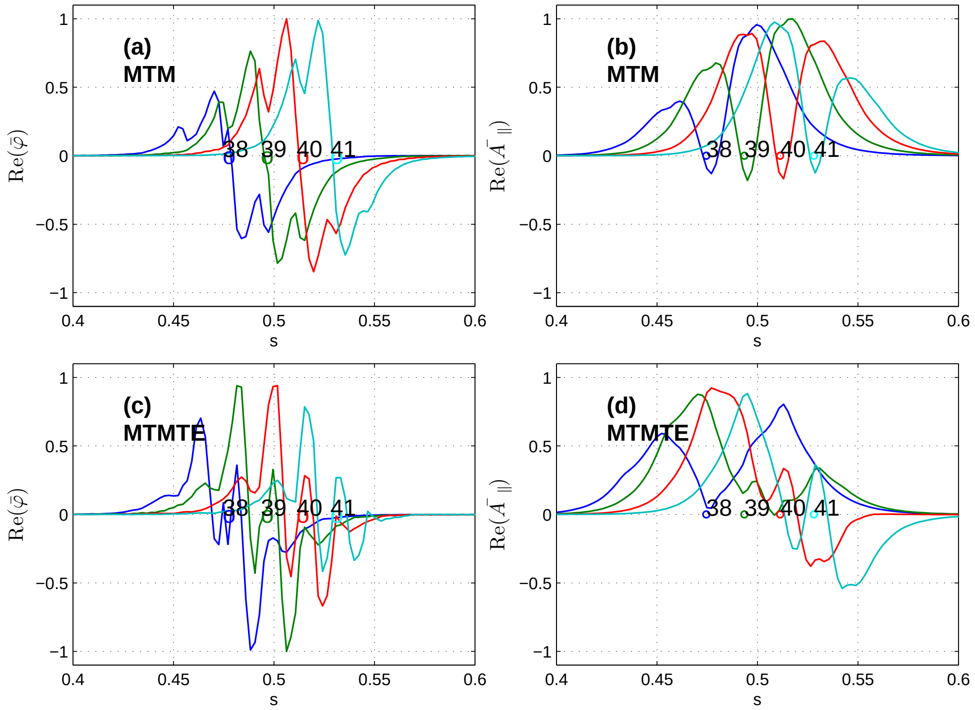


Figure 4.4: $\mathrm{Re}(\tilde{\varphi})$ (left column) and $\mathrm{Re}(\tilde{A}_{\|})$ (right column) for MTM ((a) and (b)) and MTMTE with trapped electrons included ((c) and (d)) for the $n = 23$ toroidal mode at $\beta_0 = 5\%$, $\eta = 4$. The most dominant poloidal Fourier modes $m$ are shown. The circles on the axis $y = 0$ labeled by values of $m$ indicate the location of MRS $(m, n)$. Each poloidal Fourier mode has appropriate parity about its MRS.

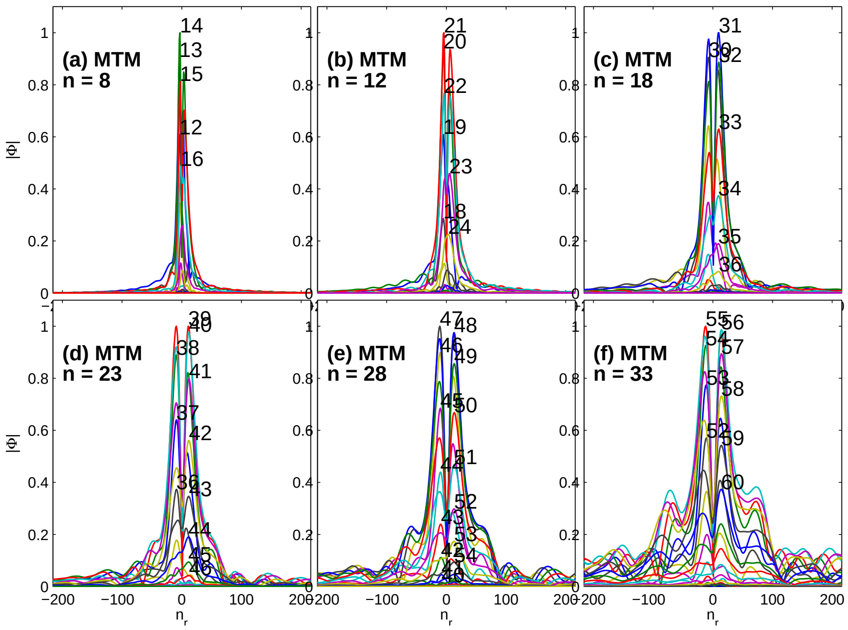


Figure 4.5: Radial Fourier space plots for MTM $\tilde{\varphi}$ fluctuations $n = 8, 12, .., 33$, excluding trapped electrons.

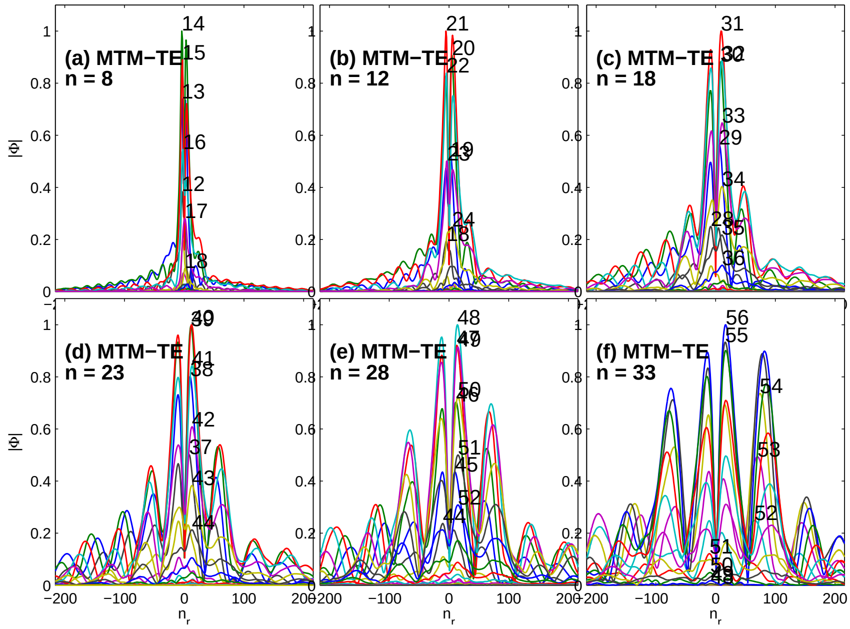

Figure 4.6: Radial Fourier space plots for MTMTE $\tilde{\varphi}$ fluctuations $n = 8, 12, .., 33$, inlcuding trapped electrons.

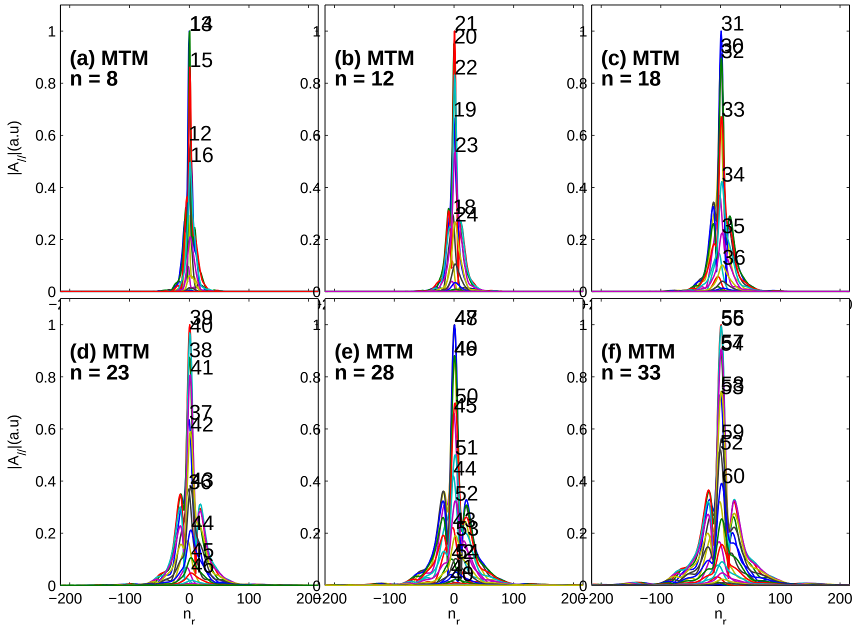

Figure 4.7: Radial Fourier space plots for MTM $\tilde{A}_{\parallel}$ fluctuations $n = 8, 12, .., 33$, excluding trapped electrons.

denominator in the non-adiabatic part of distribution function. For the parameters considered, the average toroidal precessional drift of the banana-orbit averaged guiding centre is $< \dot{\phi} >\sim -1/2\frac{v_{the}^2}{\Omega_e}\frac{1}{R}\frac{q_s}{r} = [0.1 - 0.01]c_s/a$. Thus, a resonance due to the toroidal phase velocity of the wave $\omega_r/k_\phi$ ($k_\phi = n/R$) being close to the av-

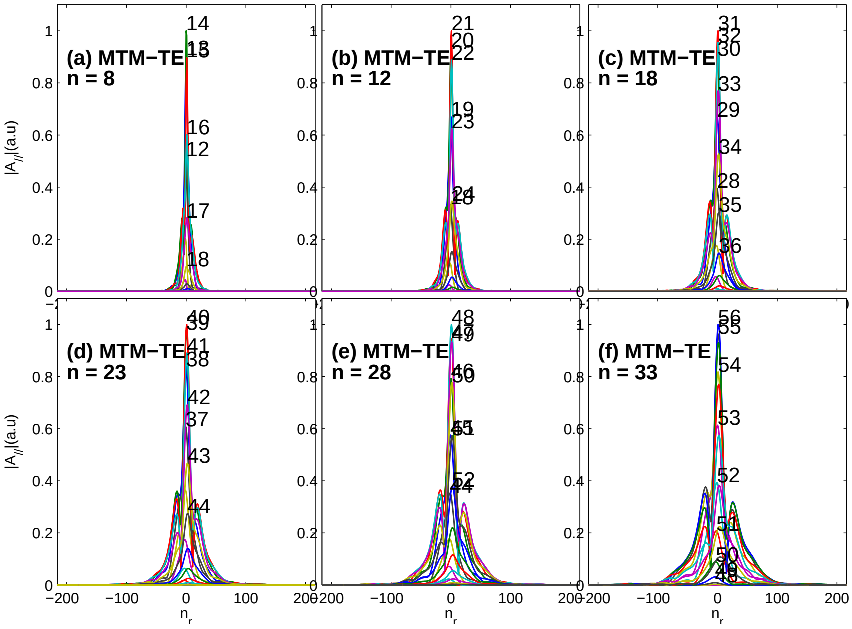


Figure 4.8: Radial Fourier space plots for MTM $\tilde{A}_{\parallel}$ fluctuations $n = 8, 12, .., 33$, including trapped electrons.

erage toroidal precessional drift of the guiding centre causes a destabilization. For instance, it is seen in Figs. 4.5 and 4.6 that at higher $n$, the coefficients $C_{(k_r,m)}$ are much higher for MTMTE than MTM, where $k_r\rho_i = 2\pi n_r/\Delta\rho \simeq 2\pi\rho^* n_r/\Delta s$ (see Sec. 2.1) At higher $n$, the resonance becomes stronger, leading to destabilization, whereas at lower $n$, the trapped electron destabilisation is ineffective. However, the growth rates may not increase continuously for indefinitely higher values of $n$. With the gyrokinetic formulation taking the FLR effects to all orders in $k_\perp\rho_{i,e}$, it is seen from Figs. 4.5 that at higher toroidal mode numbers $n$, the radial Fourier spectrum spreads to near-electron-Larmor scales $k_r\rho_i \sim \rho_i/\rho_e$. This is accompanied by a relative reduction in the ion-scale Fourier amplitudes $k_r\rho_i \sim 1$, with respect to the amplitudes at shorter scales, leading to an FLR stabilization via the argument of the Bessel functions $J_0$. The eigen-function (and hence $\gamma$) for resonance is a result of the combined effect of the passing electron resonance due to the magnetic drifts and transit frequency harmonics, and the trapped electron resonances discussed above and FLR stabilization and may result in a saturation or stabilization.

In Fig. 4.9 the dependence of the instability on $\beta_0$ is shown. At larger plasma $\beta$,

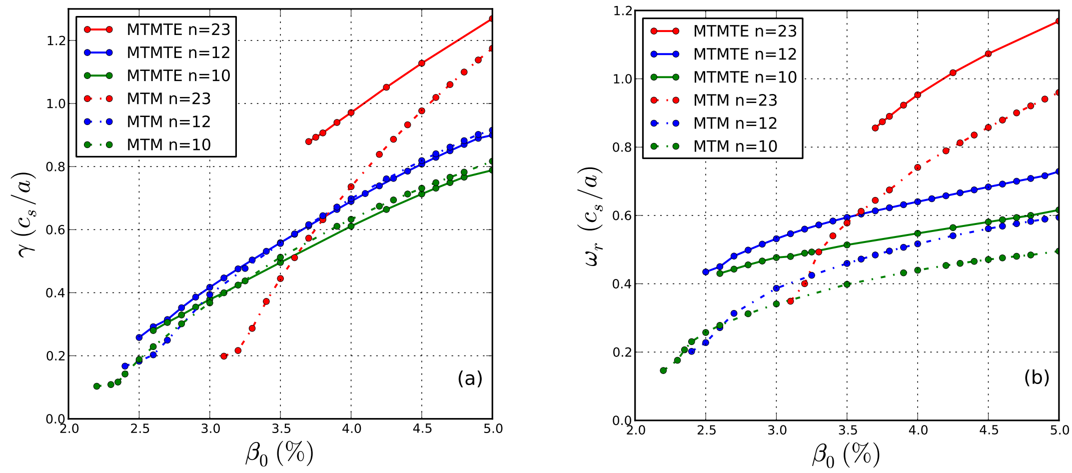


Figure 4.9: (a) Growth rates (b) frequencies versus plasma $\beta_0$ for MTM (without trapped electrons) and MTMTE (with trapped electrons) $n = 10, 12$ and 23 modes at $\eta = 4$.

larger toroidal modes $n$ are more unstable. The lower toroidal modes span a larger width across the minor radius, and can thus sample a larger free energy. Consequently, the lower toroidal modes $n$ remain more unstable as $\beta$ is lowered, with the $n = 10$ mode having a threshold of $\beta_c = 2.0 \sim 2.5\%$. At lower $\beta$, the modes acquire a broader $k_r$ spectrum [discussed later] extending to Debye and electron-Larmor scales, and the shielding becomes more relevant. This necessitates Poisson equation rather than quasi-neutrality condition for consistency and convergence. Since the nonadiabatic trapped electrons couple to the destabilizing $\tilde{\varphi}$, it is apparent that MTMTE modes remain more unstable than MTM. It is observed that the critical $\beta_c$ of MTMTE for $n = 10$ may well be below 2% for the profiles considered here. The Pure trapped electron modes and ITG-TEMs survive at finite $\beta$. Microtearing mode branches may coexist or mode-couple to finite $\beta$ branches of these modes as one lowers $\beta$. In general multiple unstable, multiple unstable modes are found some of which have mixed parity structure. Mixed parity modes without trapped electrons for different magnetic shear profiles will be addressed in Chapter 5.

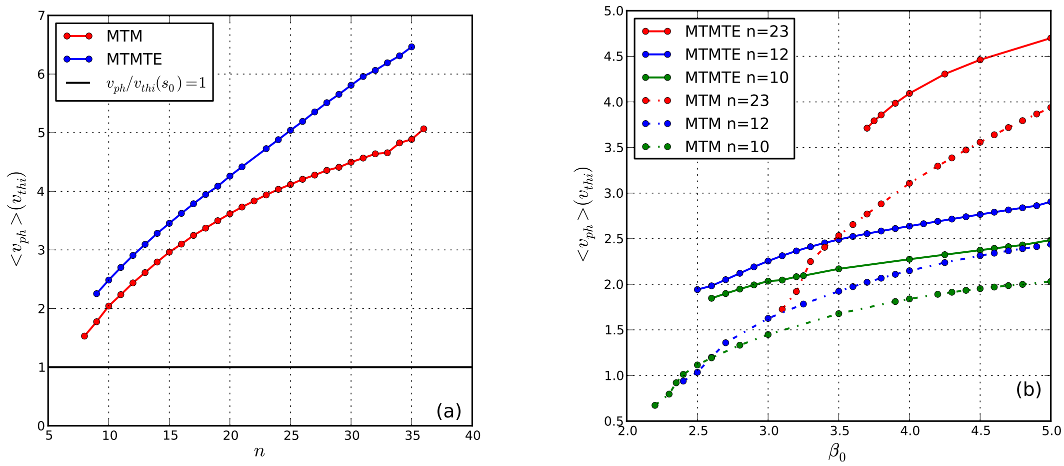


Figure 4.10: Mode-averaged parallel phase velocities for MTM and MTMTE at $\eta = 4$ (a) at $\beta_0 = 5\%$ versus toroidal mode number $n$ and (b) dependence on plasma $\beta$

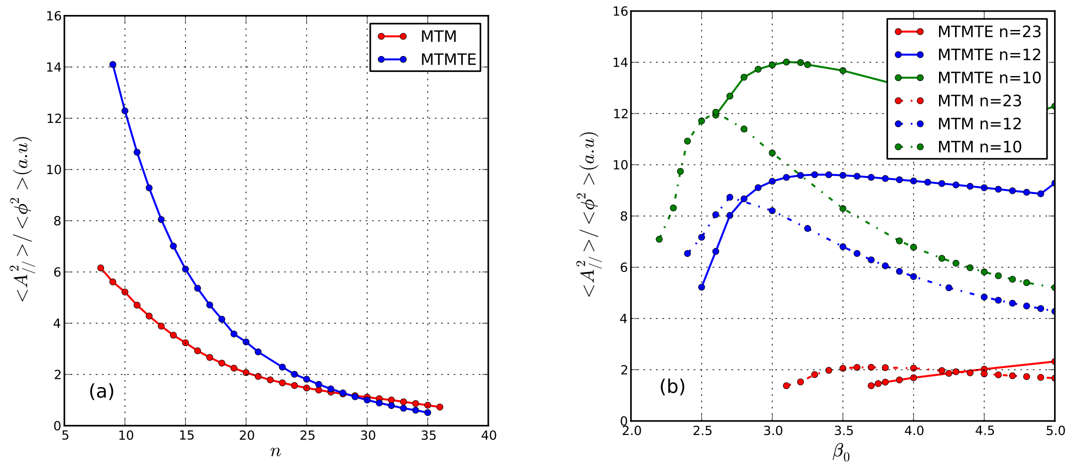


Figure 4.11: Ratio of strength of $\tilde{A}_{\|}$ and $\tilde{\varphi}$ for MTM and MTMTE. (a) dependence on $n$ at $\beta_0 = 5\%$, at $\eta = 4$, and (b) dependence on $\beta$ at $\eta = 4$

### 4.2.2 Mode averaged characteristics

Several physical characteristics can be obtained from the 2D global mode structures, weighted by the eigenfunctions as defined in Eq.( 3.1). Microtearing modes have been found not too strongly damped by the Landau resonance in earlier works [70]. This is borne out by the magnitude of the mode-averaged parallel phase velocity, denoted as $v_{ph}$ in Fig. 4.10 which is fairly large as compared to the average ion-thermal velocity $v_{th,i}$ and disparately different from the electron thermal velocity $v_{th,e}$. This makes the Landau resonance ineffective, especially for high mode numbers. The relative strengths of the potentials $\tilde{A}_{\|}$ and $\tilde{\varphi}$ can be obtained as the so-called electromagnetic ratio $<\tilde{A}_{\|}^2>/<\tilde{\varphi}^2>$ as shown in Fig. 4.11. It is observed that the strength of $\tilde{A}_{\|}$ is enhanced with the inclusion of trapped electrons. The non-adiabatic trapped electrons contribute only to $\tilde{\varphi}$ and are observed to significantly change the overall electron response and particularly on the MRS. As a result, the poloidal Fourier components $\tilde{\varphi}_m$ are seen to be changed on all MRS and not just their respective $(m, n)$ surface. This is observed to lead to the creation of more localised and sharper gradient regions of $\tilde{\varphi}$ fluctuations, as shown in Figs. 4.2 and 4.3. At values closer to the threshold $\beta_c$ required for the onset of the instability, the strength of $\tilde{A}_{\|}$ is reduced owing to lesser $\beta$, while $\tilde{\varphi}$ being insensitive to the $\beta$ is relatively sustained due to the nonadiabatic trapped electron contribution. This appears to lower $<\tilde{A}_{\|}^2>/<\tilde{\varphi}^2>$ ratio for MTMTE than for passing particle MTM.

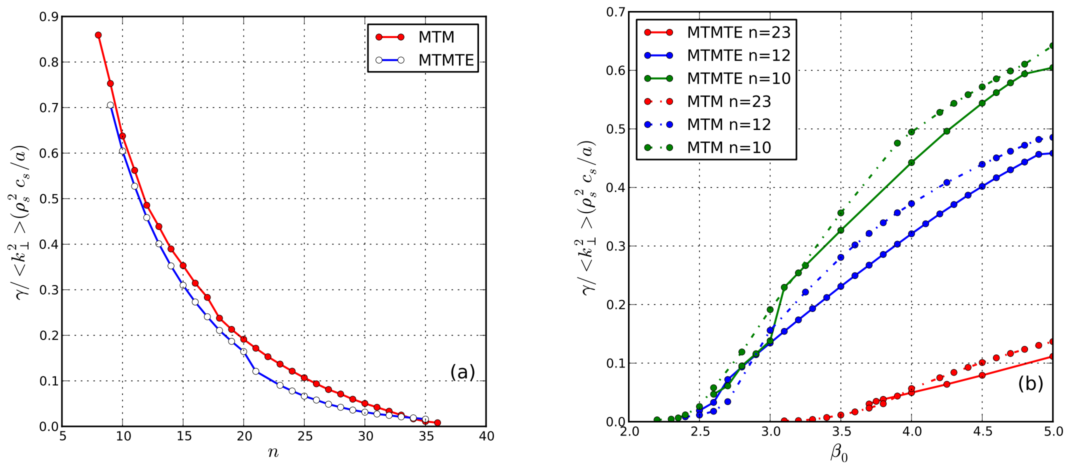


Figure 4.12: Mixing length estimates for MTM and MTMTE (a) for different toroidal mode numbers $n$ at $\beta_0 = 5\%$, at $\eta = 4$, and (b) dependence on $\beta$ at $\eta = 4$

The mode-averaged transverse wavenumbers are shown in Fig. 4.13. The radial spectrum of $\tilde{\varphi}$ fluctuations are found to span ion and electron-Larmor scales, particularly at high toroidal modes $n$ and/or near the marginal stability boundary,

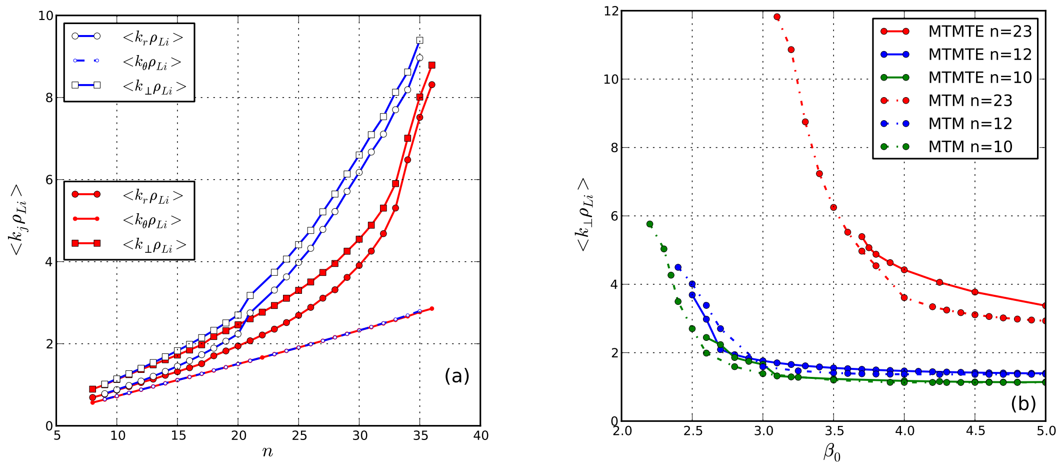


Figure 4.13: Mode averaged values of perpendicular wavenumbers for MTM and MTMTE (a) for different toroidal mode numbers $n$ at $\beta_0 = 5\%$, at $\eta = 4$, and (b) dependence on $\beta$ at $\eta = 4$

while $\tilde{A}_{\|}$ spectrum is found to remain of the order ion-Larmor scale. Consequently, the mode-averaged $k_\perp$ is dominated by $\tilde{\varphi}$. In the radial direction, the numerically-converged mode structures have significant amplitude of Fourier space coefficients, symbolically represented as $C_{(k_r,m)}$. For instance, for the $n = 23$ mode, [see Fig. 4.5] $C(k_r\rho_e = 0.5)/C(k_r\rho_e \sim 0.0) \approx 20\%$ for MTM. (Subscripts are dropped hereafter for simplicity). With the inclusion of trapped electrons, the shorter scale fluctuation amplitudes is found to be further enhanced, $(C(k_r\rho_e = 0.5)/C(k_r\rho_e \sim 0.0) \approx 35\%$ [Fig. 4.6]). Thus mode averaged $< k_\perp\rho_i >$ is relatively large for MTMTE than MTM. Similarly, closer to the marginal stability boundary [ Fig. 3.26] the amplitudes at electron scales are significant for MTM and, again, is further enhanced with the inclusion of nonadiabatic trapped electrons. Larger wavenumbers have been reported in earlier works as well [38, 39, 74]. In spite of the destabilisation of the mode by non-adiabatic trapped electrons, the implication on transport maybe relatively small due to the reduced fluctuation length scales. A mixing length estimate in Fig. 4.12(a) shows a reduced estimate for MTMTE than MTM for the parameters used. With an increase in $\beta$ however, the transport is observed to increase, as shown in Fig. 4.12(b). Since the $< k_\perp\rho_i >$ values asymptote to a finite constant value at larger $\beta_0$, while the growth rate increases with $\beta_0$, the transport is observed to increase with larger beta.

## 4.3 Dependence on aspect ratio

Collisionless MTM has been reported in the past in Spherical Tokamak simulations, where the collisionless drive due to the drift resonance of trapped electron population is found to lead to the destabilisation. A finite contribution from trapped electrons to the parallel current fluctuations $\tilde{j}_{\|}$ is observed, which arises from an asymmetry in the parallel velocity dependence of the distribution function. In contrast, collisionless MTM reported in large aspect ratio has been found to be driven by the magnetic drift resonance of passing electrons. Since the trapped electron fraction is relatively smaller at larger aspect ratio, a gyrokinetic model with the liberty of ignoring the non-adiabatic trapped electrons provided essential characteristics of these passing particle driven MTMs.

At a specified aspect ratio, a systematic study with the inclusion of trapped electrons as described in the earlier section demonstrates that these modes remain unstable due to the toroidal precessional drift of the guiding centre. Thus, it is worthwhile investigating the MTMTE across varied aspect ratio geometries. Such as study is carried out by varying the major radius $R$ while maintaining a constant system minor radius $a$ as well as the rest of the equilibrium profiles and the parameters of Table 3.1. The major radius $R$ is varied in the range $1.5 - 3m$, corresponding to aspect ratio $A = 3 - 6$. The normalizations are independent of the major radius, while local Larmor radii, local safety factor $q$ and magnetic shear are identical across the different simulations. The poloidal wavenumber $< k_\theta \rho_{Li} >$ values are seen to remain constant within 1% percent in this aspect ratio range, as seen in Fig. 4.15. The important change in the dynamics coming due to change in major radius $R$ are the fraction of trapped/passing particles, the parallel and toroidal wave vectors $k_{\parallel}$, $k_{\phi}$ respectively, the transit frequency $\omega_{t,j}$ and the trapped particle bounce frequency $\omega_{b,j}$ of the species $j = e, i$, leading to changes in the nature of the mode.

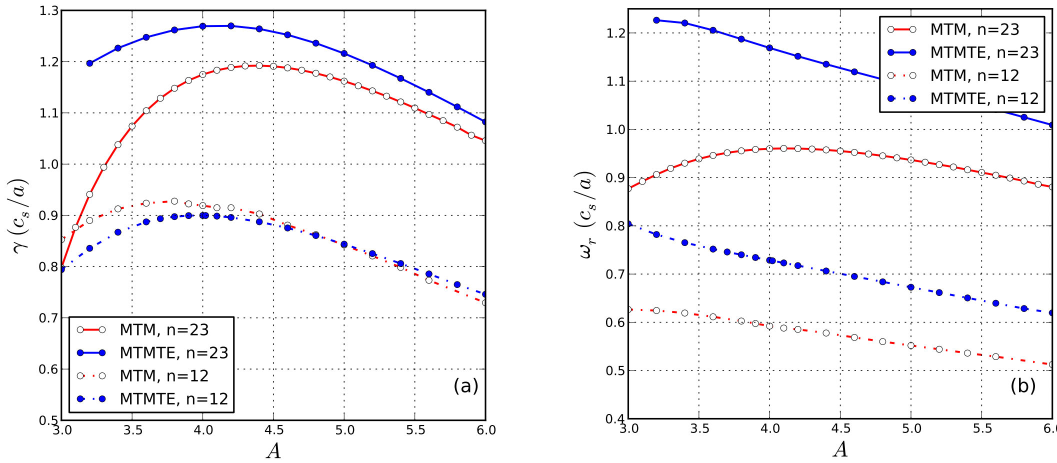


Figure 4.14: (a) Growth rates (b) frequencies versus aspect ratio $A$ for MTM and MTMTE modes $n = 12, 23$ at $\beta_0 = 5\%$, $\eta = 4$,.

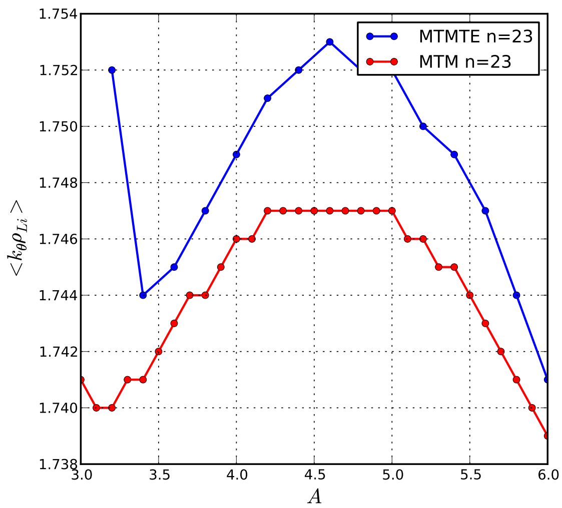


Figure 4.15: Mode averaged values of $k_\theta$ versus aspect ratio $A$ for MTM and MTMTE $n = 23$ mode at $\beta_0 = 5\%$ and $\eta = 4$. For the range of aspect ratio $(A)$ variation studied here, variation in $\overline{k}_\theta \rho_{Li}$ is less than 1%.

With the change in aspect ratio $A$, the resonance of the mode with the transit harmonics, Landau resonance, magnetic drift resonance and precessional drift is altered. This is also reflected in the mode averaged parallel phase velocities, Fig. 4.16, which are seen to increase at larger aspect ratio. As seen earlier, the Landau damping

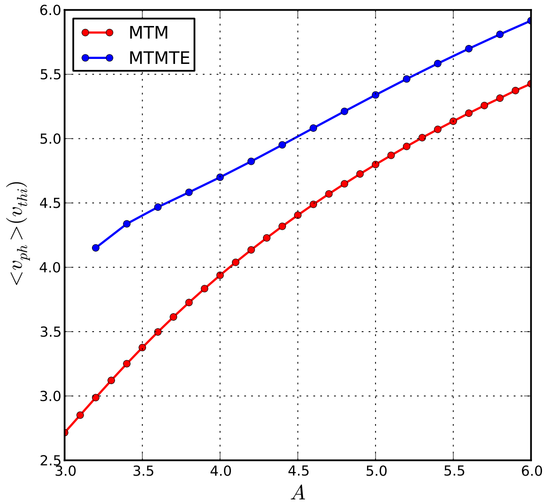


Figure 4.16: Mode averaged values of parallel phase velocity versus aspect ratio $A$ for MTM and MTMTE $n = 23$ mode at $\beta_0 = 5\%$ and $\eta = 4$.

is ineffective for the MTM frequencies at the equilibrium profiles considered here. Fig. 4.14 shows the results of the Aspect Ratio study. The growth rates are shown for the toroidal modes $n = 12, 23$ for the case without including the trapped electrons and for the case including them. The growth rates show a general tendency to peak at a particular aspect ratio and declining for lower and higher values of $A$. The growth rates without the trapped electrons are seen to be close to that including the trapped electrons, consistent with the fact that at large aspect ratios, the relative fraction of trapped electrons is reduced.

## 4.4 Conclusion

The microtearing modes, which are low-frequency, electron-driven electromagnetic microinstability are studied for collisionless hot plasmas in large aspect ratio tokamaks.

- In this comprehensive 2D global gyrokinetic study considering fully gyrokinetic trapped and passing particles, the nonadiabatic electrons are found to contribute to electrostatic fluctuations $\tilde{\varphi}$ via a resonant toroidal precessional drift and destabilize them.

- This is observed to lead to the creation of more localised and sharper gradient regions of $\tilde{\varphi}$ fluctuations near the mode rational surfaces.

- The aspect ratio scan within a finite range by varying the major radius $R$ shows that the trapped electron destabilization adds to the predominant passing electron drive, significantly altering the growth rates at smaller aspect ratios.

- At a given aspect ratio and plasma $\beta$, the resonant destabilization is relatively more effective the for the high-$n$ modes than at low $n$.

- The $\beta$ threshold for the onset of the instability with only passing electrons is found to be lower for the low $n$ modes. The non-adiabatic trapped electron drive further downshifts the threshold.

- The ratio of the strength of the magnetic vector potential and electrostatic potential fluctuations is seen to be strongly dependent on $k_\theta \rho_i$ and plasma pressure $\beta$.

- The mixing length transport estimate obtained from linear growth rates show that the transport is increased at higher plasma $\beta$.

Steady state operation of tokamaks is an essential requirement for a commercial fusion reactor, which entails improved confinement. Fusion power $\propto \beta^2$, hence high $\beta$ is desired for tokamak operation. However, several instabilities set in at higher $\beta$. For identification of the operating regime that is benevolent to these twin objectives, experiments in several present day tokamaks have been performed to explore different magnetic shear configurations and are known as advanced tokamak scenarios. Understanding the possible transport in such scenarios is again of much importance. The characteristics of linear electromagnetic instabilities is studied in such scenarios in the next Chapter.

# Chapter 5

# Electromagnetic microinstabilities in weak reversed shear configuration

## 5.1 Introduction

Collisionless microtearing modes are found to be unstable in finite $\beta$ plasma in large aspect ratio Tokamaks and are described in Chapter 3 and Chapter 4. In the presence of a steep electron temperature gradient in such plasmas, the nonadiabatic passing electron dynamics destabilizes the mode. Considering a monotonic safety factor profile $q(s)$ typical of L and H mode plasmas in several tokamaks [8], the mode is found to be unstable in a wide range of $\beta$ and $\eta$ values. The trapped electrons affect the shorter scale, or higher-$n$ limit. As the aspect ratio is reduced, the trapped electrons strongly destabilize the modes further. For the same equilibrium profiles and parameters, the ion temperature gradient driven electromagnetic mode AITG or Kinetic Ballooning Mode (KBM) is also found to be unstable. The AITG mode is found unstable above a $\beta$ threshold which is lower than the threshold for MTM. The monotonically increasing $q$-profile is obtained in plasmas when the electric current is fully diffused to the core or the magnetic-axis. Such profiles used in Chapters 3 and 4 will be referred hereafter as “reference $q$-profile”.

Operation of tokamaks as commercial fusion power reactors require steady state or quasi-steady state plasma, which is possible only with improved confinement. Reversed magnetic shear operations in existing Tokamaks such as JET and DIII-D, obtained by an off-axis current drive have shown the formation of an Internal Transport Barrier (ITB) near the location of mode rational surfaces in the low shear or $q_{min}$ region, which results in improved confinement in these discharges. Steady state experiments, including ITER, thus envisage a reversed magnetic shear profile as one of the “advanced scenarios” of operation. The plasma current profile, which determines the safety factor profile, is hence one of the main parameters in these advanced scenarios. An equally important configuration is the hybrid configuration with near-zero magnetic shear in the core region and monotonically increasing $q(s)$ with positive shear for $s \gtrsim 0.5$. In practice, such advanced $q$-profile configurations are realized by non-inductive current drive mechanisms such as EECD, N-NBI and LHCD. A detailed account of the progress in steady state operational scenarios is compiled in ITER Physics Basis 2007 [8].

Since the ITB is formed in the $q_{min}$ region, the detailed nature of MTM and AITG is of interest for transport studies in such advanced configurations as described above. Global gyrokinetic simulations are well suited to bring out the response of MTM and AITG to the underlying equilibrium in these scenarios. The results from such a study is discussed in this Chapter, in particular, for sensitivity to global $q$ profile changes, keeping a constant $q$ value at $s = 0.5$ and constant temperature profiles.

The influence of non-adiabatic trapped electrons on the MTM was studied in Chapter 4 and it was found that their dynamics is significant in altering the linear growth rates. For collisionless MTMs in the reference scenario $q$-profiles, the trapped electron dynamics was found to be particularly important at smaller aspect ratios whereas they were found to become negligible for low-n values at larger aspect ratio. For example, at a typical large aspect ratio of 4, the toroidal mode number scan showed that trapped electron dynamics is significant for high-$n$, and arose from the toroidal precessional drift resonance with the mode frequency and was fairly ineffective at low-$n$. It was also shown that in the presence of trapped electrons, the short scale structures in $\tilde{\varphi}$ necessitate a large $n_r$ spectrum (radial spectrum) and are numerically demanding. Hence, in order to better delineate the dynamics of passing particles from that of trapped particles on the primarily passing electron-driven collisionless MTMs, and to reduce the numerical demand, the effect of trapped electrons are not considered in this Chapter.

The rest of this Chapter is organized as follows: In Sec. 5.2, the sensitivity of MTM and AITG to global $q$ profile changes, (with the associated shear) is studied, keeping a constant $q$ value at $s = 0.5$ and constant temperature profile. Multiple modes of MTM and AITG are found to be unstable, with several subdominant branches showing complex dependence on shear, including a transformation to mixed parity modes. The 2-D global mode structures of MTM and the mixed parity modes at various values of shear are presented in detail in Sec. 5.3. In Sec. 5.4, the toroidal mode number scan for MTM and AITG is obtained and compared in reference $q$-profile and weak reverse shear $q$-profiles. The $\beta$ dependence of MTM and AITG modes in weak reverse shear configuration is studied in Sec. 5.5. An investigation of the dependence of the mode location of MTM and AITG on variation of temperature gradient location in these magnetic configurations is carried out in Sec. 5.6. This is followed by Conclusion.

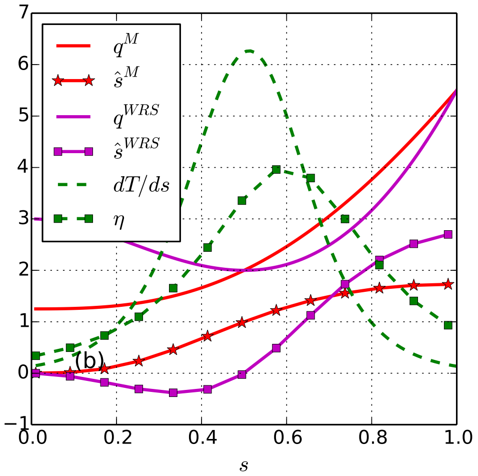


Figure 5.1: The safety factor profiles - standard $q^M$ and reversed shear $q^{WRS}$ as functions of normalized radius $s$. The corresponding magnetic shear $\hat{s}$ profiles and $dT/ds$ profile are also shown. $\eta$ profile peaks at $s_0 = 0.6$, while $dT/ds$ peaks near $s \simeq 0.5$

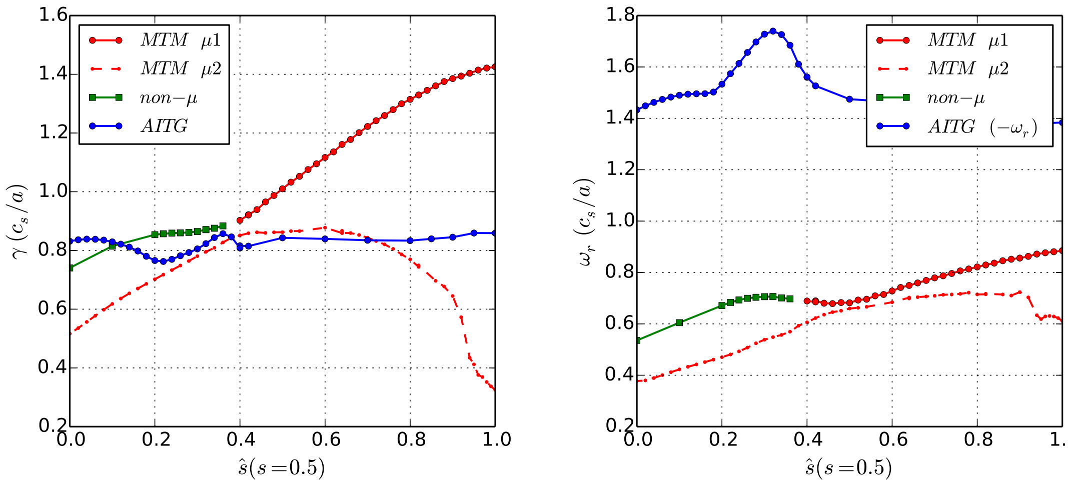


Figure 5.2: (a) Growth rates and (b) real frequencies of MTM and AITG for $n = 12$ as $q$ profile is changed from regular $q^M$ to reversed shear $q^{WRS}$. Multiple subdominant MTM branches are found, apart from the two studied here.

## 5.2 Sensitivity to safety factor profile

The advanced scenarios of tokamak operation envisage a reversed shear $q$-profile with a zero shear at an off-axis location having $q_{min}$ lower than the central $q$ and a

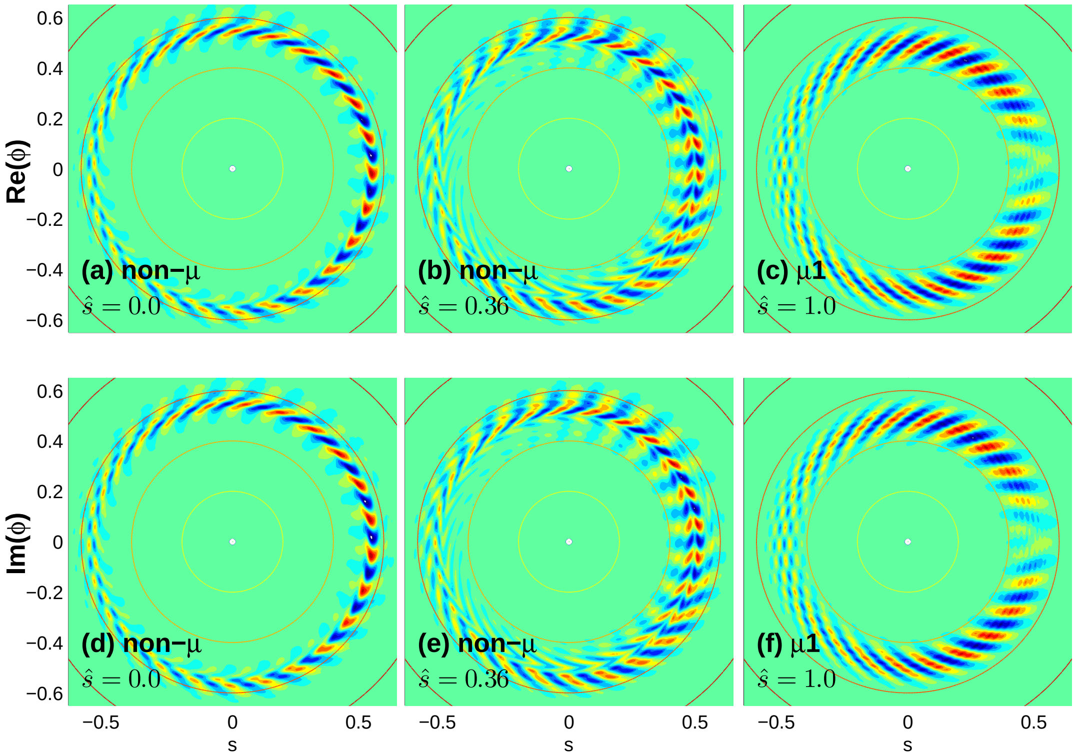


Figure 5.3: Contour plots of real and imaginary parts of $\tilde{\varphi}$ for $n = 12$ MTM mode $\mu 1$ and non-$\mu$ mixed parity mode in Fig. 5.2. Re($\tilde{\varphi}$) and Im($\tilde{\varphi}$) has a null through $\theta = 0$ in (c) an (f), respectively as required for the tearing parity of MTM, unlike the mixed-parity non-$\mu$ mode in (a),(b),(d) and (e).

negative shear region towards the core. Previously, global linear studies have shown that the magnetic shear has a complex influence on the growth rates of the ion-driven modes such as ITG and AITG at different plasma parameters [48, 49, 50]. Thus, it is pertinent to investigate the nature of MTM in such advanced configurations using the global approach. In this Section, MTM and AITG modes are studied for their sensitivity towards dependence on global $q$ profiles considering only passing particles.

The study is performed starting from the known MTM and AITG eigenmodes for monotonic $q$ profiles from Chapter 3. Using a quartic polynomial form for $q(s)$ as in Table. 3.1, a monotonic $q$ profile $q^M$ is obtained for $q_0 = 1.25,\ q_2 = 0.25,\ q_3 = 7.0,\ q_4 = -3.0$. With this profile, $q = 2$ and $\hat{s} = 1$ at $s = 0.5$. A weak reversed shear (WRS) profile $q^{WRS}$ is obtained for $q_0 = 3.0,\ q_2 = -13.5,\ q_3 = 22.0,\ q_4 =$

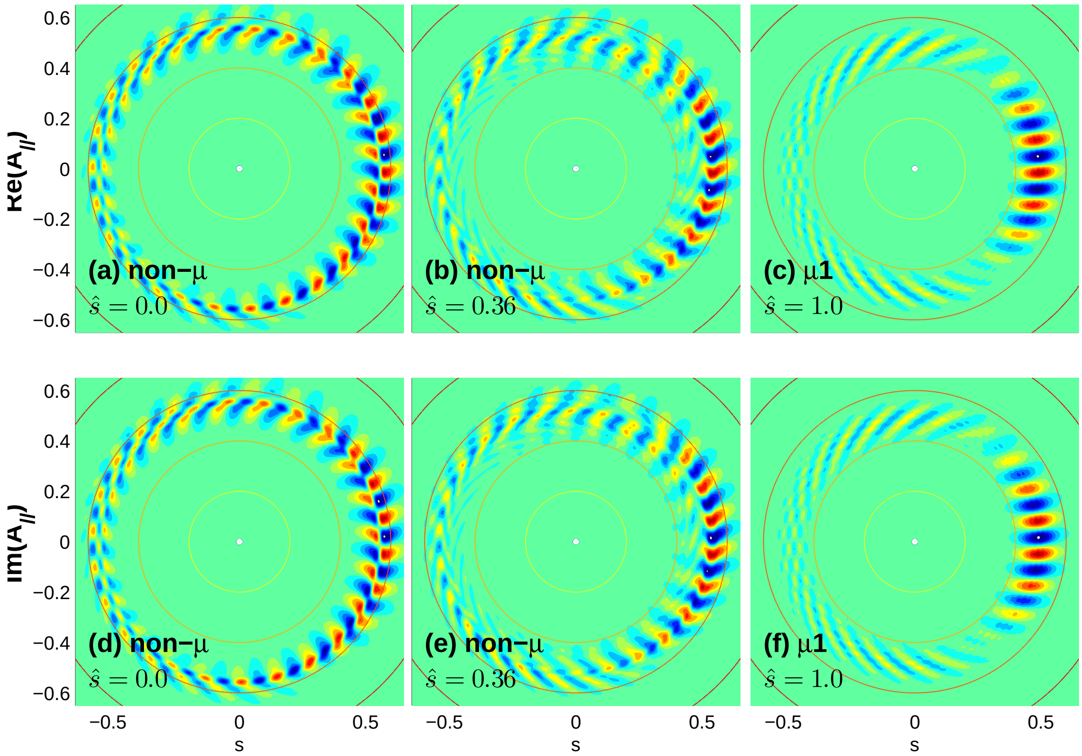


Figure 5.4: Contour plots of real and imaginary parts of $\tilde{A}_{\|}$ for $n = 12$ MTM mode $\mu 1$ and non-$\mu$ mixed parity mode in Fig. 5.2. Re($\tilde{A}_{\|}$) and Im($\tilde{A}_{\|}$) have a maxima through $\theta = 0$ in (c) an (f), respectively, as required for the tearing parity of MTM, unlike the mixed-parity non-$\mu$ mode in (a),(b),(d) and (e).

$-6.0$. With these coefficients, $q = q_{min} = 2$ and $\hat{s} = 0$ at $s = 0.5$. As will be seen in Sec. 5.6 for the monotonic $q^M$ profile, the MTM mode has a mean radial location at $s = 0.5$. Hence, the temperature profile is fixed such that $T = T_0$ at $s = s_0 = 0.6$ so that the free energy drive $(dT/ds)_{max}$ appears at the mean location of the mode $s = 0.5$. Fig. 5.1 shows the radial variation of the safety factor profiles $q^M, q^{WRS}$ and the corresponding shear profiles $\hat{s}^M, \hat{s}^{WRS}$, as well as the temperature gradient profile $-dT/ds$. Intermediate $q$ profiles $q^{IM}$ are generated by setting $q^{IM} = \alpha_{IM} q^M + (1 - \alpha_{IM}) q^{WRS}$, where $\alpha_{IM}$ is a constant [48, 49]. For any given value of $\alpha_{IM} = 0.0 - 1.0$, the safety factor $q(s = 0.5) = 2.0$ and local magnetic shear $\hat{s}(s = 0.5) = \alpha_{IM}$.

In Chapter 4, it was seen that the trapped electron dynamics is negligible at low toroidal mode numbers at large aspect ratio, for monotonic $q$ profile. Hence,

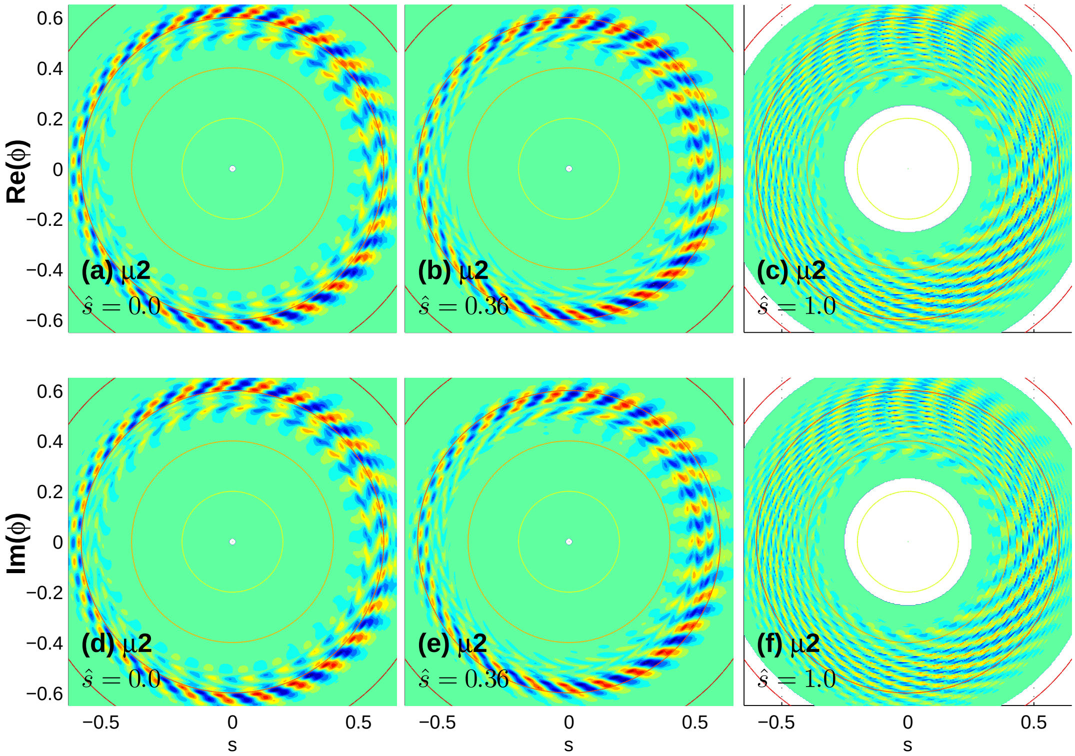


Figure 5.5: Contour plots of real and imaginary parts of $\tilde{\varphi}$ for $n = 12$ MTM mode $\mu 2$ in Fig. 5.2.

$n = 12$ is considered and a scan in the global $q$ profiles with the above constraints is performed. Fig. 5.2 shows the sensitivity of such a global shear profile variation on the MTM and AITG modes for $n = 12$. The intermediate $q$ profiles corresponding to the eigenvalues shown in Fig. 5.2 are uniquely identified by the value of shear at the radial location $s = 0.5$, although it is to be noted that the mode eigenvalue and characteristics are a net result of the global profiles. As observed in Chapter 3, multiple eigenmodes are unstable for any given plasma profile and can be identified by the Nyquist method. The fastest growing MTM mode at $\hat{s} = 1$ (that is, for safety factor profile $q^M$) labeled $\mu 1$, has mode characteristics similar to that in Fig. 3.1, Chapter 3, which was obtained by considering similar monotonically increasing $q$-profile. A subdominant mode labeled $\mu 2$ forms a separate branch as do several other subdominant modes [not shown here]. Similarly, AITG has several eigenmodes, the fastest growing of which is studied here. The MTM modes $\mu 1$ and $\mu 2$ are found to be very sensitive to shear profiles. As $\hat{s}$ is changed, the growth rates change by

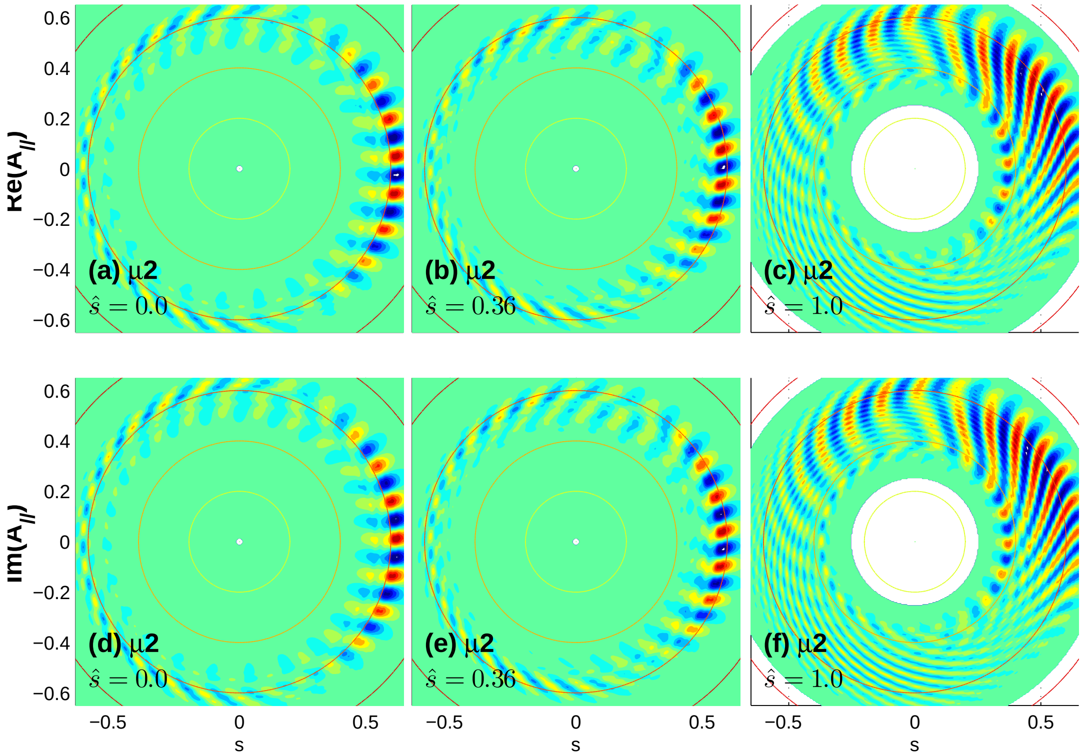


Figure 5.6: Contour plots of real and imaginary parts of $\tilde{A}_{\|}$ for $n = 12$ MTM mode $\mu 2$ in Fig. 5.2.

nearly 40% relative to the reference case. The $\mu 1$ branch is significantly stabilized at lower shear values and growth rate decreases monotonically as shear is reduced. In contrast, the $\mu 2$ branch grows more unstable as shear reduced from $\hat{s} = 1$ and attains a maximum growth rate around $\hat{s} \sim 0.5$. The growth rate decreases for even lower values of shear. Such a non-monotonic behaviour is reported for ITG, AITG as well [49, 83]. The growth rates of AITG mode, however, are seen to be relatively less sensitive to changes in the shear profiles at the plasma parameters considered [47]. Also, an AITG mode is found unstable in the negative shear region as well, and is discussed in Sec. 5.6. The change in the growth rates is accompanied by a change in the mode structures as well, as discussed in the next section. As discussed in Chapter 2, for the studies in this thesis, the underlying plasma current profile, resulting in the safety facor profiles here, and the equilibrium pressure gradients are assumed to be close to an ideal MHD equilibrium but are ad-hoc in the sense that they may not satisfy the MHD force balance. Hence, an element of caution is to be exercised with

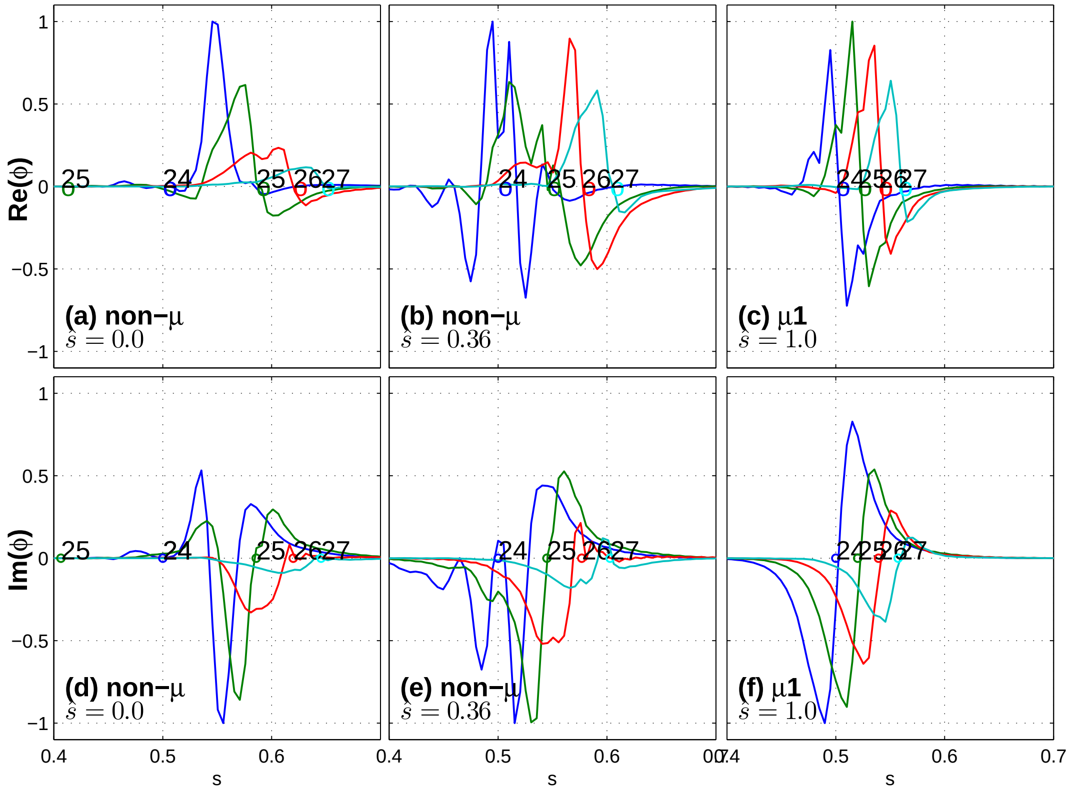


Figure 5.7: Real and imaginary parts of $\tilde{\varphi}$ for $n = 12$ MTM mode $\mu 1$ and non-$\mu$ mode in Fig. 5.2. Individual poloidal Fourier components of Re($\tilde{\varphi}$) and Im($\tilde{\varphi}$) are odd about their corresponding MRS in (c) an (f), respectively as required for the tearing parity of MTM, unlike the mixed-parity non-$\mu$ mode in (a),(b),(d) and (e).

respect to the quantitative observations from the present study and is discussed in Chapter 6.

## 5.3 Global mode structures and emergence of mixed parity modes

The dominant and subdominant unstable eigenmodes (of MTM and AITG) possess different characteristics in different shear configurations as noted in previous section. The dominant MTM mode at $\hat{s} = 1$ has similar growth rates and global mode structures as the mode studied in Sec. 3.3, Chapter 3. The mode structures are shown in Fig. 5.3, 5.4. At $\hat{s} = 1$, the mode $\mu 1$ is located near $dT/ds|_{max}$. In contrast,

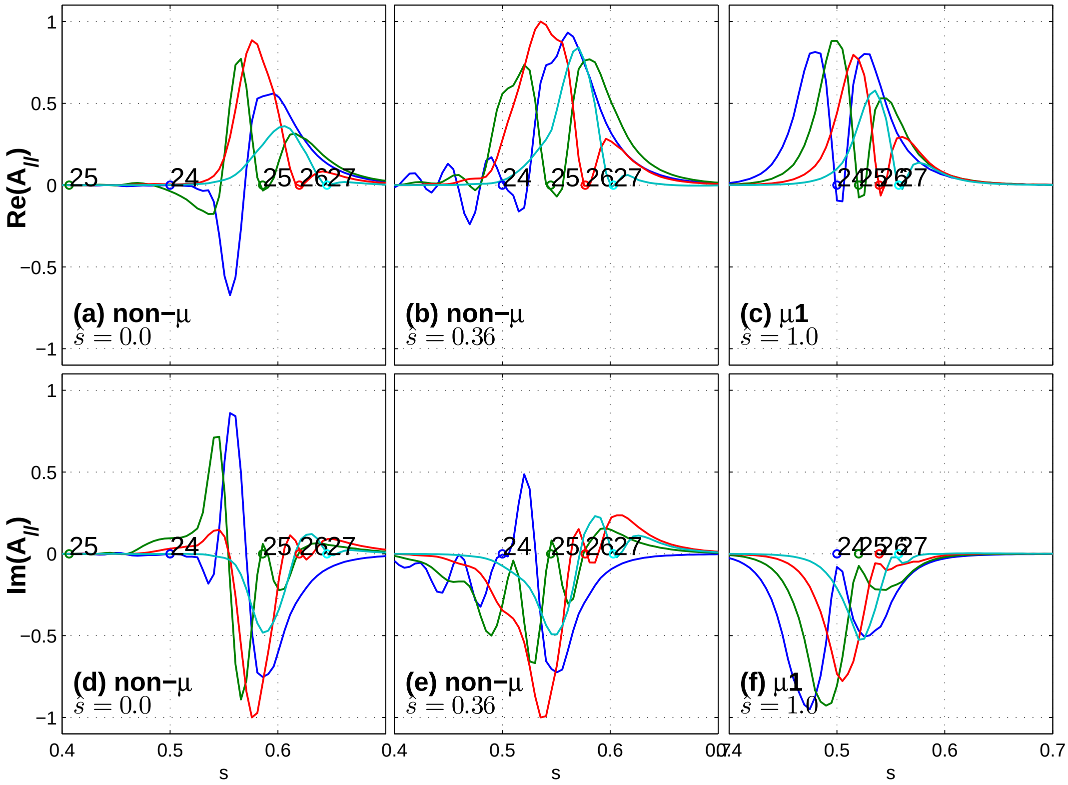


Figure 5.8: Real and imaginary parts of $\tilde{A}_{\parallel}$ for $n = 12$ MTM mode $\mu 1$ and non-$\mu$ mode in Fig. 5.2. Individual poloidal Fourier components of Re($\tilde{A}_{\parallel}$) and Im($\tilde{A}_{\parallel}$) are even about their corresponding MRS in (c) an (f), respectively as required for the tearing parity of MTM, unlike the mixed-parity non-$\mu$ mode in (a),(b),(d) and (e).

electrostatic modes such as ITG and ETG centre at the location of $\eta_{max}$, i.e. at $s_0$ [48, 84]. The mode is well converged in Fourier space [not shown], and balloons clearly on the outboard side. The poloidal Fourier modes $m$ have perturbations that are odd in $\tilde{\varphi}$ and even in $\tilde{A}_{\parallel}$ about the corresponding mode rational surface $(m, n)$. This is also reflected in the envelope of the amplitude of potentials that show a clear symmetry swap about the poloidal angle $\theta = 0$, as seen in Fig. 5.3(c,f), Fig. 5.4(c,f), Fig. 5.7(c,f) and Fig. 5.8(c,f). At reduced shear values, the symmetry properties of MTM is affected significantly, resulting in a dilution of clear tearing parity. Indeed, as indicated by green square symbols in Fig. 5.2, the eigenmode structures for shear values below $\hat{s} \sim 0.4$ are no longer identifiable with the clear tearing parity properties in $\tilde{\varphi}$ and $\tilde{A}_{\parallel}$. These modes are dubbed as non-$\mu$ or Mixed Parity Modes.

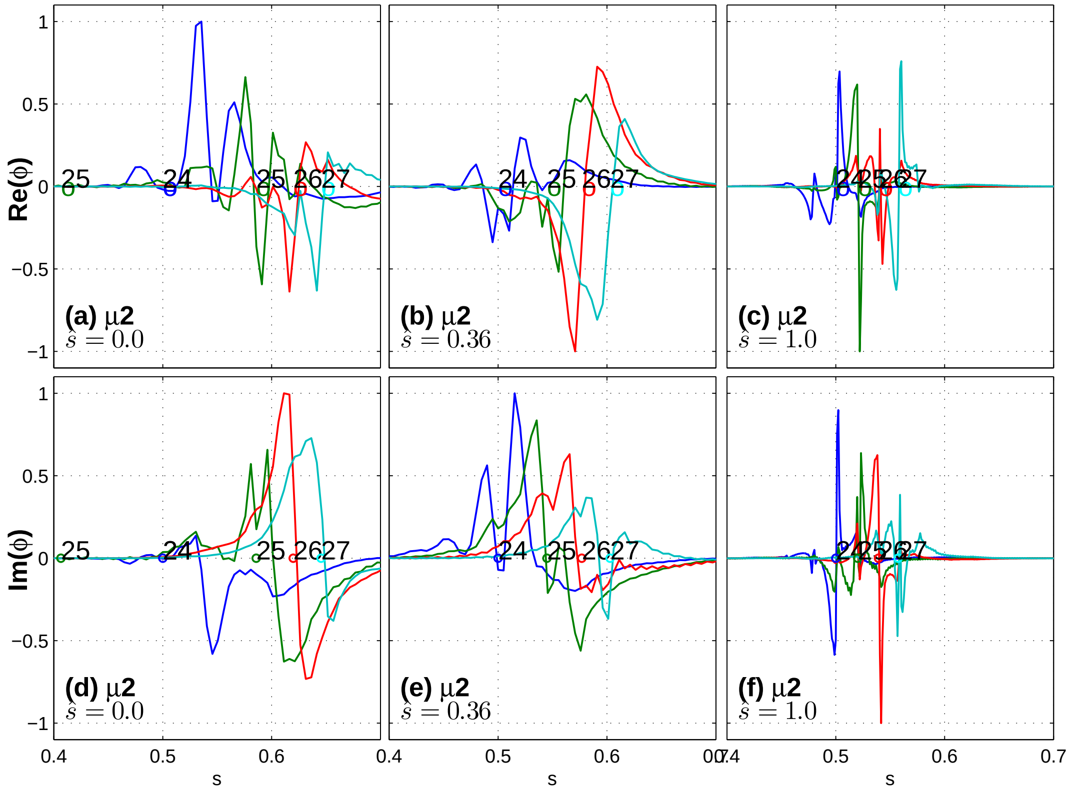


Figure 5.9: Real and imaginary parts of $\tilde{\varphi}$ for $n = 12$ MTM mode $\mu 2$ in Fig. 5.2.

The gradual loss of tearing parity is evident in Figs. 5.3, 5.4, in the contour plot of $\tilde{\varphi}$ and $\tilde{A}_{\|}$ for shear values $\hat{s} \simeq 0$ and $\hat{s} \simeq 0.36$ and labeled as non-$\mu$. The poloidal Fourier components in these modes do not all possess a clear parity but are, rather, a mix of even and odd natured functions. Fig. 5.11, 5.12 show the $\theta$ dependence of 2D potentials $\tilde{\varphi}$ and $\tilde{A}_{\|}$ upon averaging in the radial direction (see Sec. 3.3, Chapter 3). The envelope of $\tilde{\varphi}$ fails to retain a minimum through $\theta = 0$, accompanied by a similar change in $\tilde{A}_{\|}$, which fails to retain a maximum through $\theta = 0$. This is reflected in the plot of individual poloidal Fourier components $m$ of $\mathrm{Re}(\tilde{\varphi})$ and $\mathrm{Re}(\tilde{A}_{\|})$ in Fig. 5.7, 5.8, where it is seen that at the lower shear values $\hat{s} \simeq 0$ and $\hat{s} \simeq 0.36$, the modes do not possess an odd and even parity respectively about their corresponding mode rational surfaces $(m, n)$. The imaginary parts shown in the bottom rows show similar behaviour. The emergence of such linearly unstable mixed parity modes is reported here perhaps for the first time. Lower growth rates modes are known to be important for the understanding of the energy dynamics during

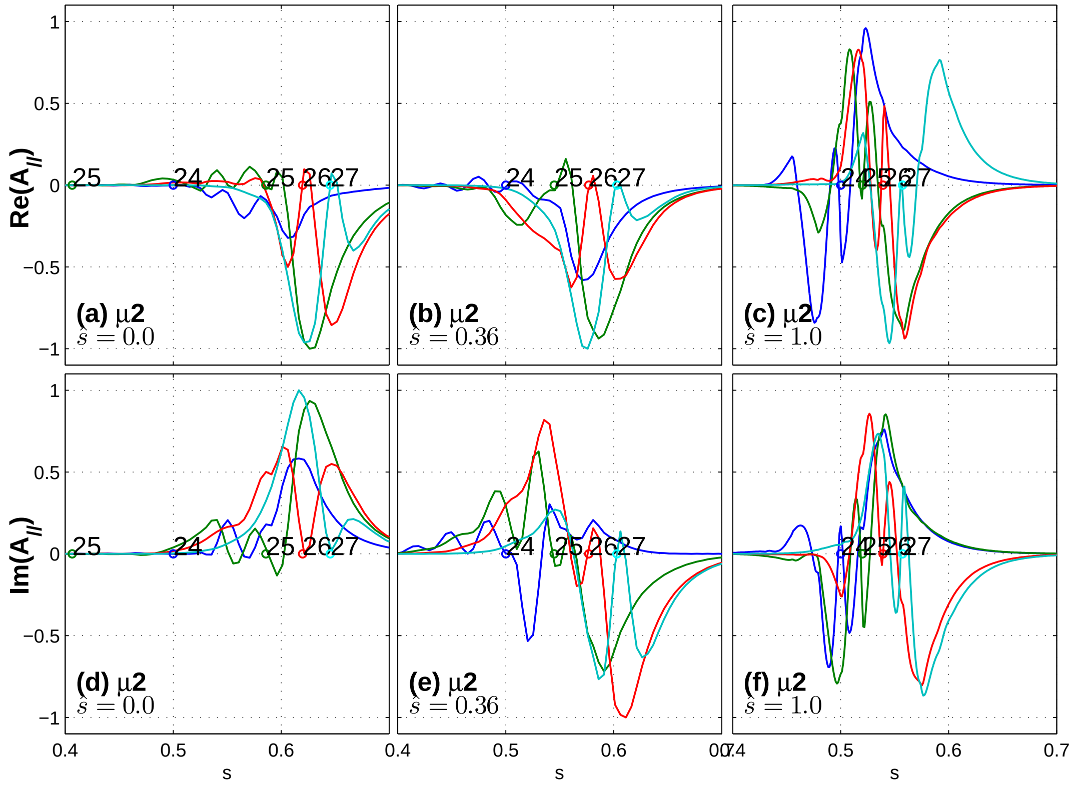


Figure 5.10: Real and imaginary parts of $\tilde{A}_{\|}$ for $n = 12$ MTM mode $\mu 2$ in Fig. 5.2.

turbulence saturation in finite $\beta$ gyrokinetic simulations [20, 85, 86, 87]. These modes are believed to play potentially an important role in the non-linear saturation of turbulence and hence necessitate more comprehensive simulations considering these aspects. Mixed parity modes are again of importance in L-H transitions when a steep pedestal formation is believed to trigger along with ballooning parity modes, other mixed parity modes as well. Parity mixing has been investigated in the past with respect to the resistive ballooning modes and found to enhance the growth rates of these MHD modes [88, 89].

For a fixed $n$, the relative spacing between the mode rational surfaces increases with gradual reduction in $\hat{s}$. This changes the particle response to fluctuations, since the resonance depends on the cross-field magnetic drift of the electrons, affecting the coupling of adjacent poloidal Fourier components. The net result is a characteristic change in the radial mode structures as seen in Fig. 5.7 and 5.8. With reduced shear, the relative amplitude of the dominant mode at $\hat{s} = 1$, namely $(m, n)$=$(24, 12)$

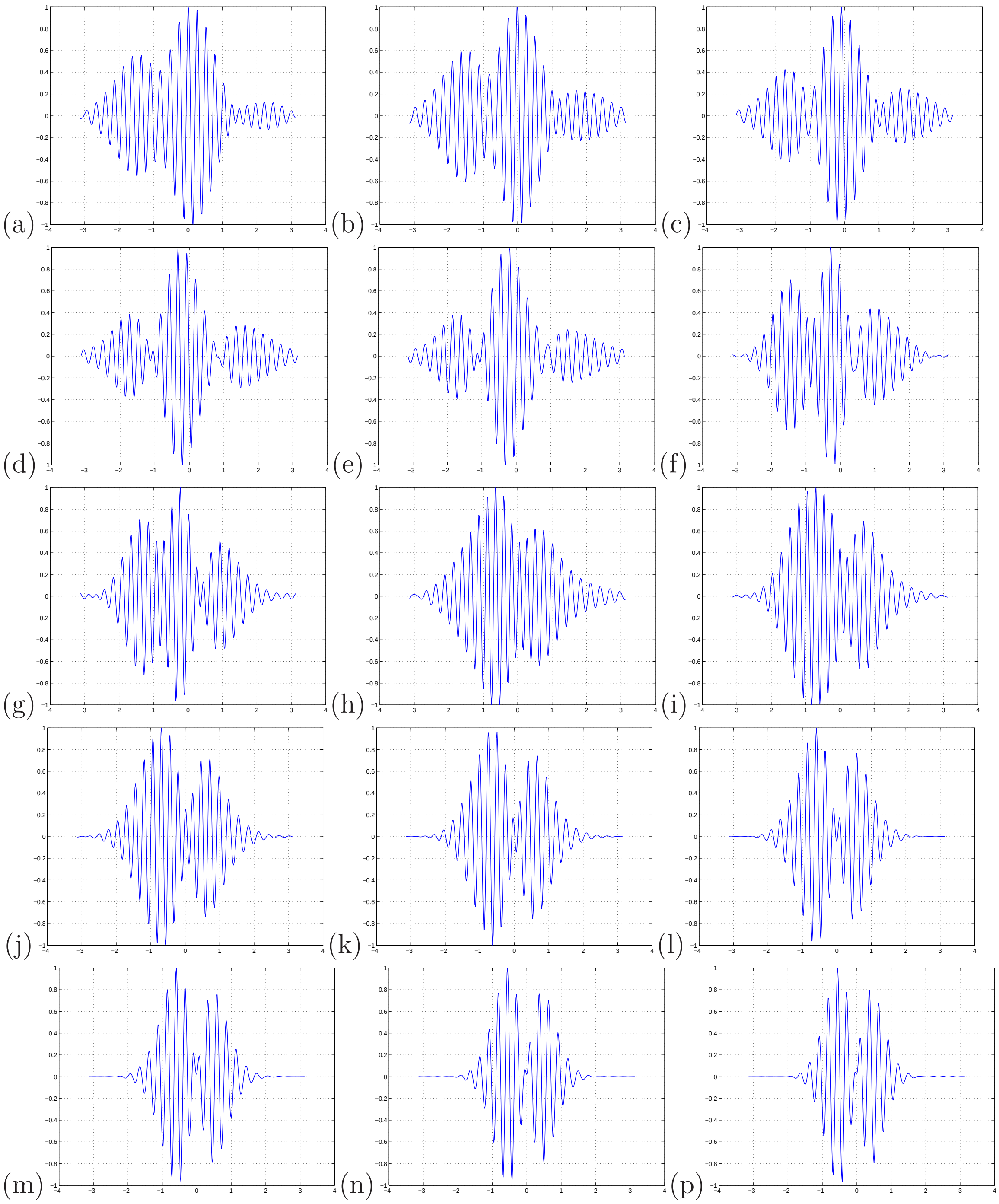

Figure 5.11: $s$-averaged plots of Re($\tilde{\varphi}$) for $n = 12$ MTM mode $\mu 1$ and non-$\mu$ mode shown in Fig. 5.2. For the subplots (a)-(n) and (p) $\hat{s} \in (0, 0.20, 0.28,\ 0.34, 0.36, 0.46, 0.52, 0.58, 0.64, 0.70, 0.76, 0.82, 0.88, 0.94, 1.0)$

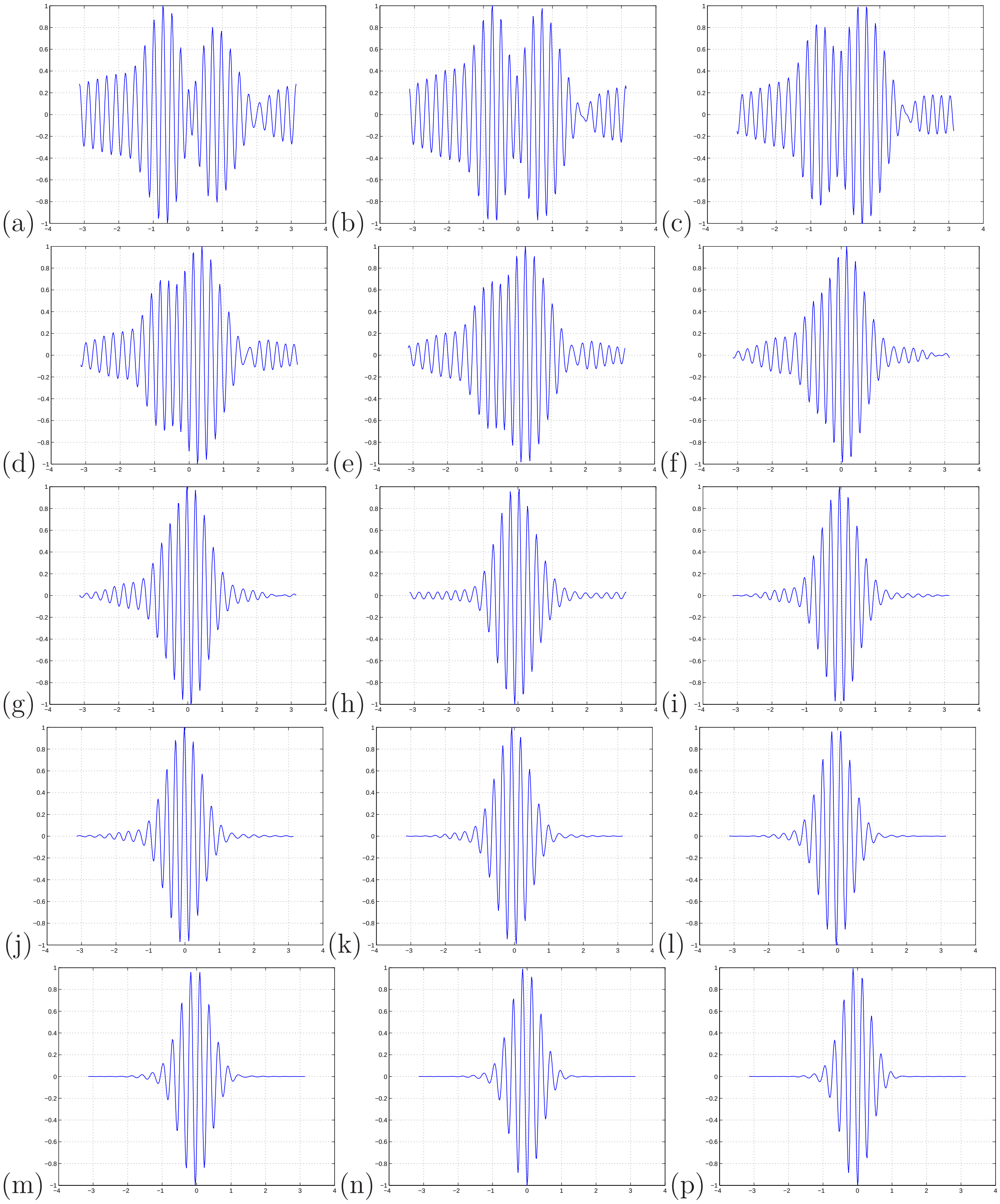

Figure 5.12: $s$-averaged plots of Re($\tilde{A}_{\|}$ ) for $n = 12$ MTM mode $\mu 1$ and non-$\mu$ mode shown in Fig. 5.2. For the subplots (a)-(n) and (p) $\hat{s} \in (0, 0.20, 0.28, 0.34, 0.36, 0.46, 0.52, 0.58, 0.64, 0.70, 0.76, 0.82, 0.88, 0.94,\ 1.0)$

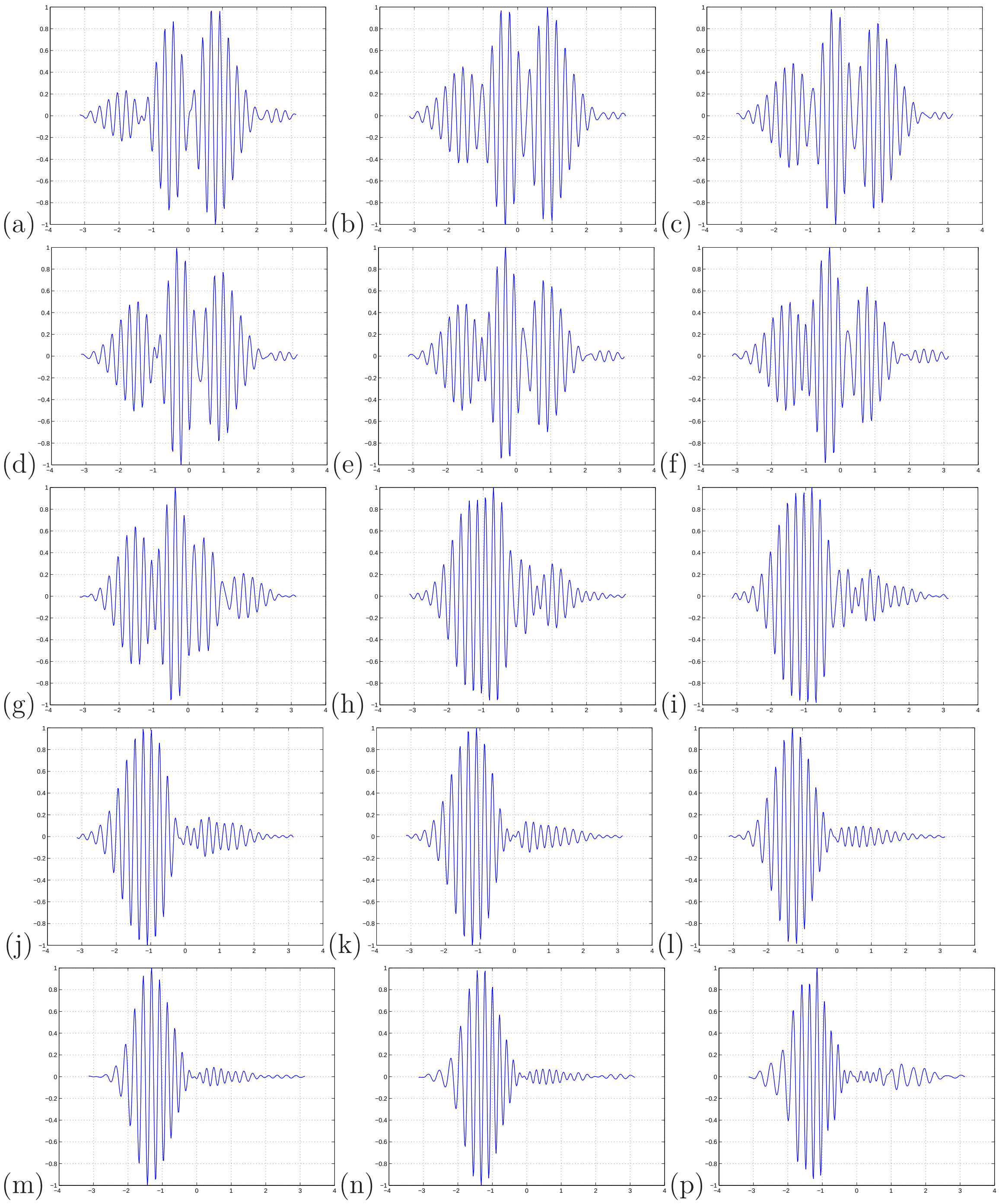


Figure 5.13: s-averaged plots of $\mathrm{Re}(\tilde{\varphi})$ for $n = 12$ MTM mode $\mu 2$ mode shown in Fig. 5.2. For the subplots (a)-(n) and (p) $\hat{s} \in (0, 0.02, 0.16, 0.22, 0.28, 0.32, 0.36, 0.46, 0.4, 0.64, 0.7, 0.76, 0.82, 0.88, 0.94, 0.98)$

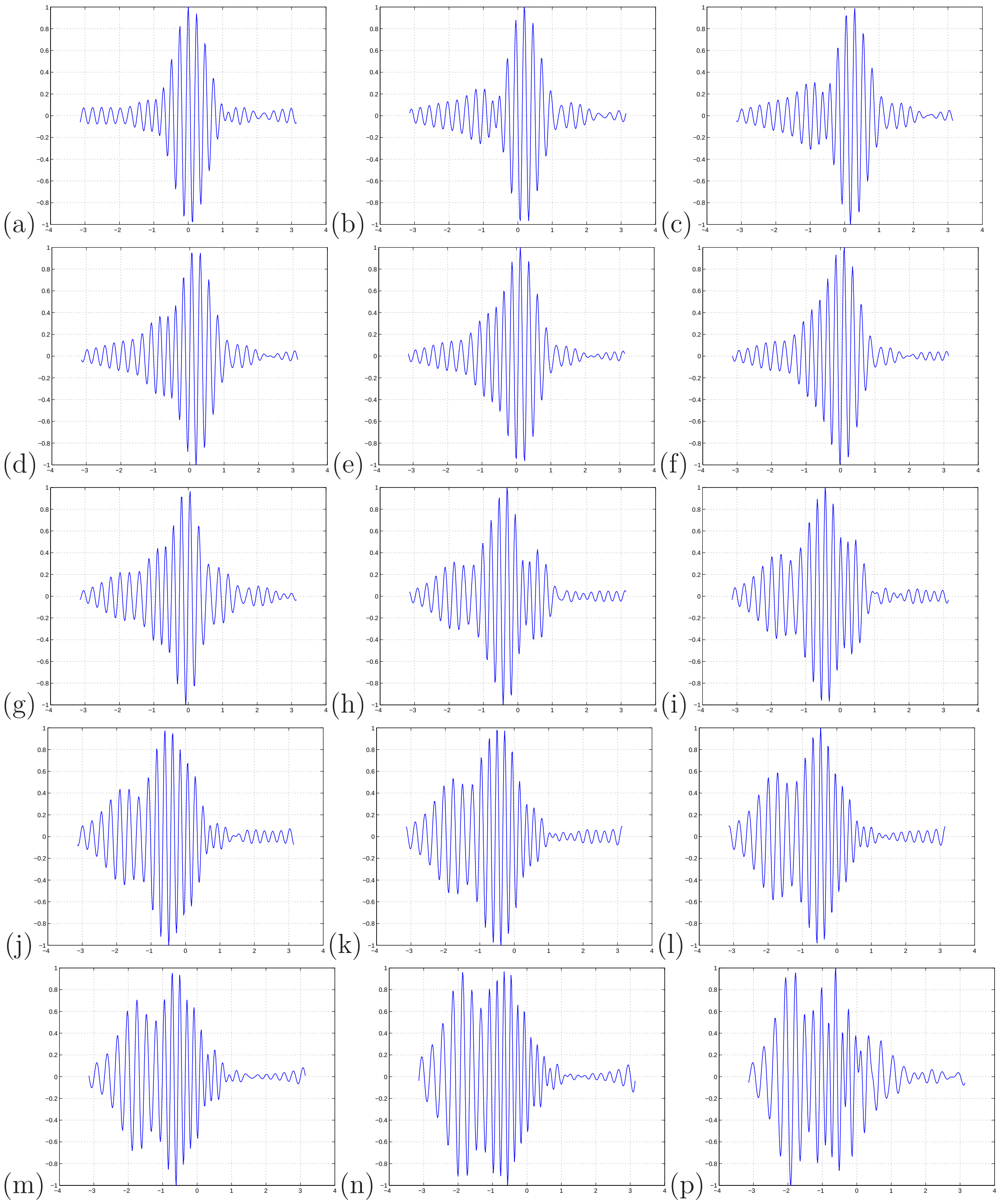

Figure 5.14: s-averaged plots of $\mathrm{Re}(\tilde{A}_{\parallel})$ for $n = 12$ MTM mode $\mu 2$ mode shown in Fig. 5.2. For the subplots (a)-(n) and (p) $\hat{s} \in (0, 0.02, 0.16, 0.22, 0.28, 0.32, 0.36, 0.46, 0.4, 0.64, 0.7, 0.76, 0.82, 0.88, 0.94, 0.98)$

reduces and ultimately loses the clear amplitude at the $q_{min}$ region. The adjacent poloidal Fourier components (such as $m = 25, 26..$) have weak symmetry properties and have the highest amplitude in the region $s \sim 0.55$. In the poloidal direction, the amplitudes are extended in a relatively larger range as seen in the left most subplots in Fig. 5.3, 5.4, 5.11(a) and 5.12(a).

The subdominant MTM mode $\mu 2$ has a clear tearing parity in reversed shear profiles $q^{WRS}$ and is apparent from the Figs. 5.5, 5.6, 5.13 and 5.14. The envelope of the amplitudes go through a minimum at $\theta = 0$ for $\varphi$ and maximum for $A_{\|}$. The mode is seen to be not located exactly near the $q_{min}$ region but is radially away at $s \sim 0.58$ in the positive shear region where $\hat{s} \simeq 0.7$ and will be discussed in the next Section. This is also evident from the real space plots Fig. 5.9, 5.10, where the $(24, 12)$ mode does not have any amplitude at $s = 0.5$. The adjacent poloidal Fourier components $m$ are seen to possess the tearing parity. Figs. 5.13, 5.14 show a clear tearing parity nature, visible more clearly at lower and higher extremes. At higher shear, in particular in Figs. 5.13((j),(k)..(n),(p)) and 5.14((j),(k)..(n),(p)), the modes show a characteristic suppression in the region $\theta > 0$ (4th quadrant Figs. 5.5, 5.6 ). The magnetic perturbation contours in Fig.[5.6] exhibit radially elongated structures in the first quadrant.

Global Microtearing modes are thus likely to be dominantly unstable in the strong magnetic shear region in the presence of steep electron temperature gradients. A reduction in the magnetic shear suppresses the dominant microtearing instability and a mode-transformation to perturbations with mixed parity is likely. The subdominant modes are not significantly affected by magnetic shear and remain unstable close to the $q_{min}$ region even in weak reversed shear configurations.

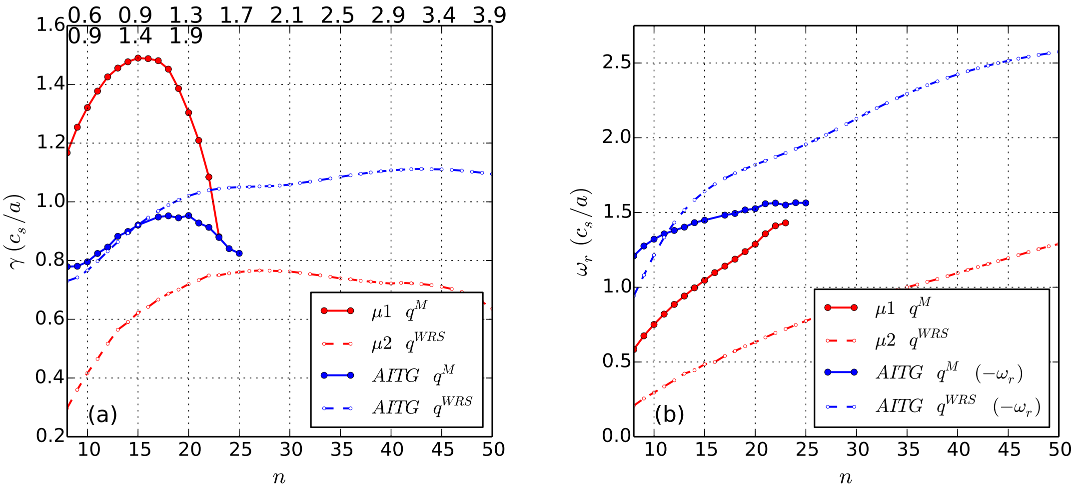


Figure 5.15: Toroidal mode number scan for MTM and AITG for safety factor profiles - regular $q^M$ and reversed shear $q^{WRS}$. The MTM branch $\mu2$ is studied for reversed shear $q^{WRS}$. $\overline{k_\theta \rho_i}$ values for $\mu1$ and $\mu2$ are indicated below and above the upper x-axis, respectively.

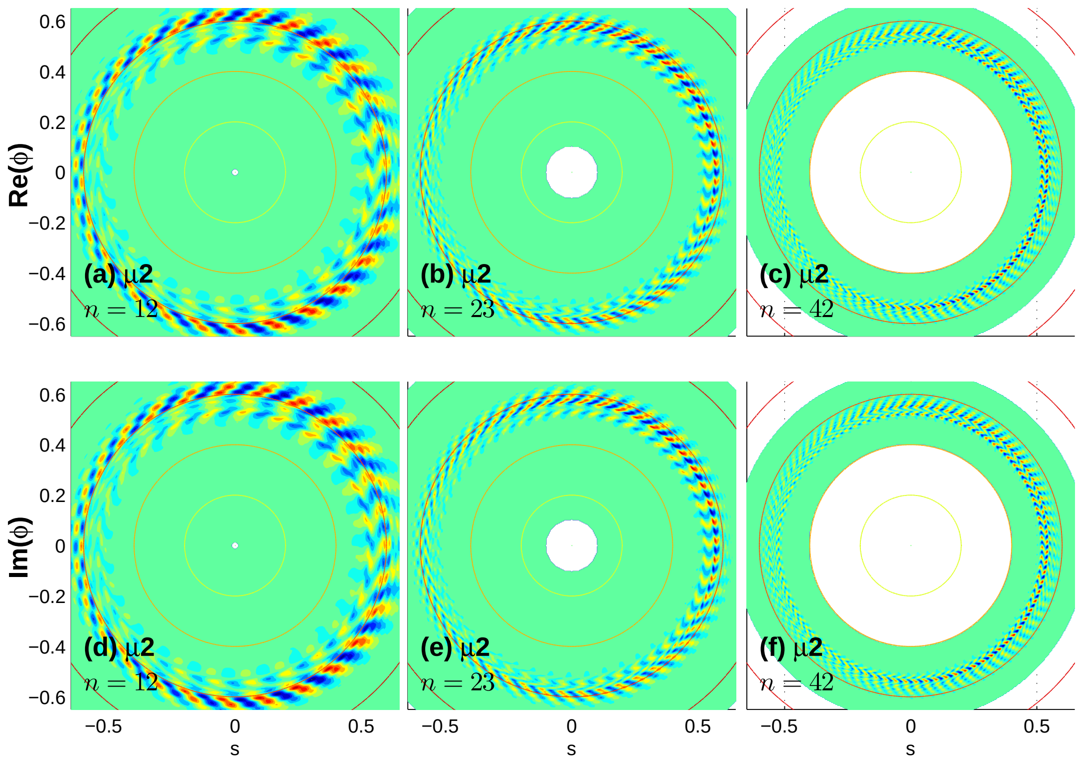


Figure 5.16: Contour plots of real and imaginary parts of $\tilde{\varphi}$ for $n = 12, 23, 42$ MTM modes $\mu2$ shown in Fig. 5.15.

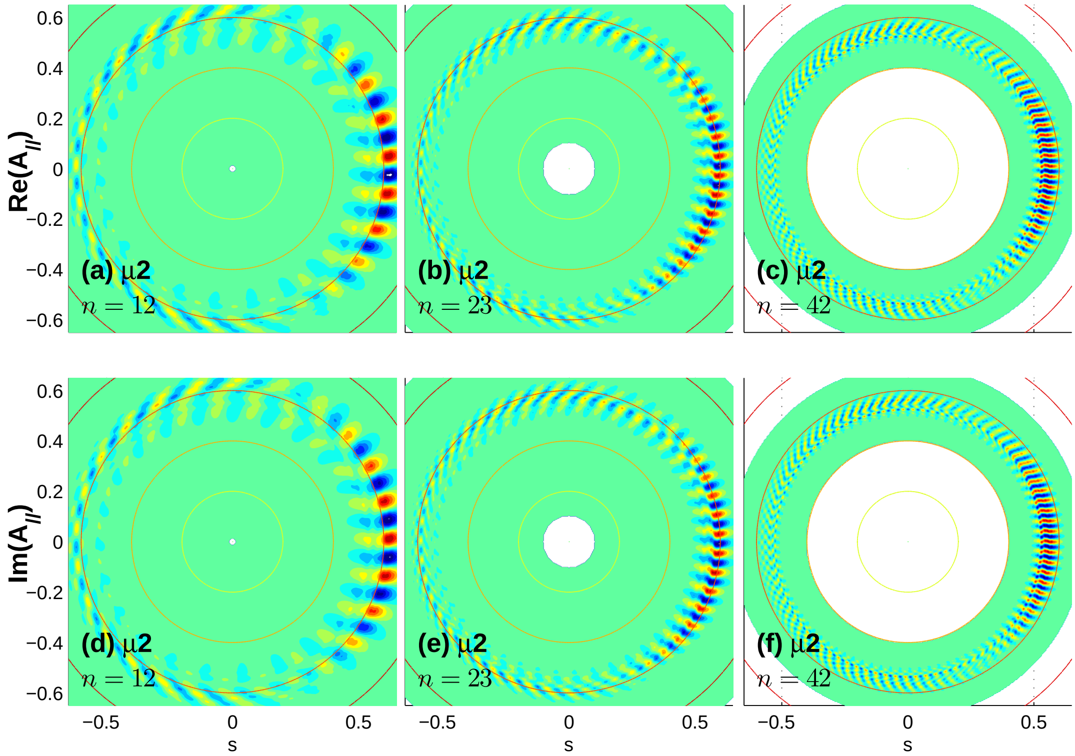


Figure 5.17: Contour plots of real and imaginary parts of $\tilde{A}_{\|}$ for $n = 12, 23, 42$ MTM modes $\mu 2$ shown in Fig. 5.15.

## 5.4 Growth rate spectrum

Growth rate spectrum has been obtained for MTM and AITG in a weak reversed shear regime for a broad range of toroidal mode numbers $n$. The study is performed for same equilibrium profiles for both MTM and AITG with $\beta_0 = 5\%, \eta = 4$ and $q^{WRS}$ and $q^M$ profiles, results of which are shown in Fig. 5.15. The real frequency of MTM is positive and that of AITG is negative, as they must be, with the electron diamagnetic direction being taken as positive by convention. The figures show the growth rate spectrum of MTM and AITG for the standard profile $q^M$ as well. The mode averaged $\overline{k_\theta \rho_i}$ values corresponding to $n$ are shown on the upper x-axis. The spectrum has a peaked structure, with highest growth rate for $\overline{k_\theta \rho_i} = 1.37, n \simeq 16$ in the regular $q(s)$ for the parameters used, and lower growth rates at still higher $n$, and is generally understood as arising due to FLR stabilization [49]. As noted in Chapter 3, the modes are mesoscale, with $\overline{k_\theta \rho_i} \sim 0.8 - 2$. MTMs below the ion

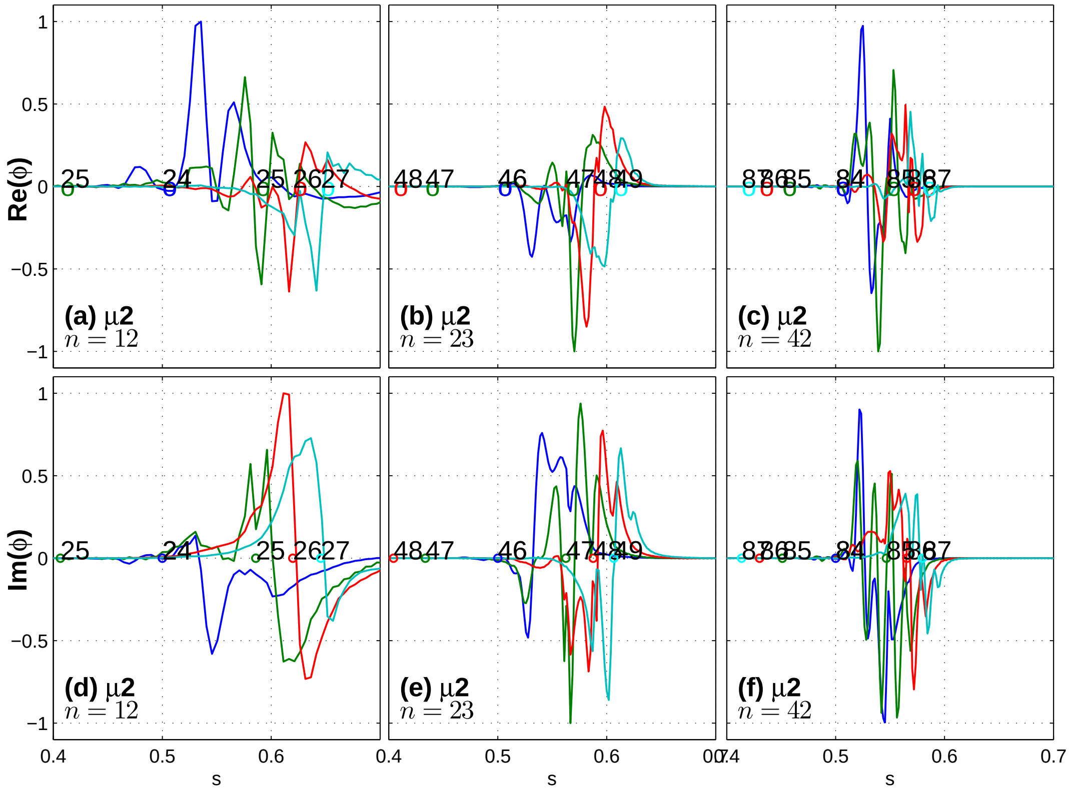


Figure 5.18: Real and Imaginary parts of $\tilde{\varphi}$ for $n = 12, 23, 42$ MTM modes $\mu 2$ shown in Fig. 5.15.

gyroscale have been reported earlier as well with and without collisions [39, 74].

As seen in Sec.[5.2], the MTM mode $\mu 2$ is seen to be unstable with finite growth rate in the weak reversed shear profile as well. However, the mode is relatively less unstable relative to the growth rates of non-$\mu$ mixed parity mode. Significantly, the unstable mode spectrum is seen to extend to much shorter wavelengths, with $\overline{k_\theta} \rho_i \sim 0.6 - 4$. In the spectrum for AITG as well, the higher-$n$ modes are seen to be unstable upto the range studied, $n \sim 50$. From these linear growth rates at the parameters considered, it is seen that the AITG modes are dominant with respect to MTM in the weak shear profile. The reason for the destabilization of higher $n$ is not entirely clear. The condition for resonance of the mode frequency of a given perturbation with the plasma has a complex dependence on various factors such as the particle velocity and the associated transit frequency (and its harmonics) and the geometry. Since many poloidal modes $m$ couple and the presence of $q_{min}$ surface

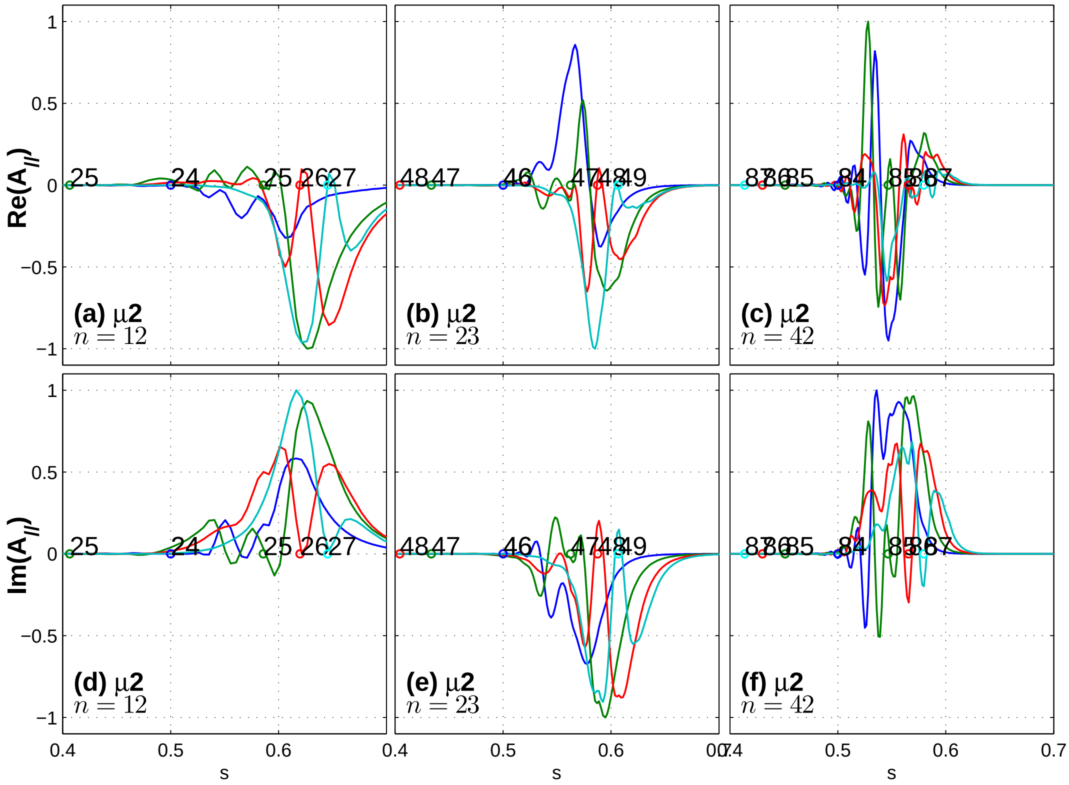


Figure 5.19: Real and Imaginary parts of $\tilde{A}_{\|}$ for $n = 12, 23, 42$ MTM modes $\mu 2$ shown in Fig. 5.15.

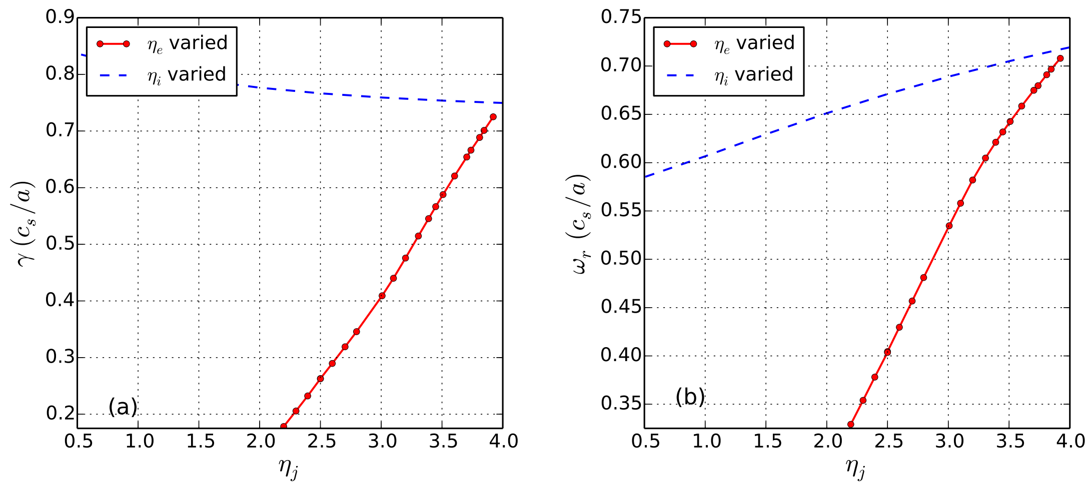


Figure 5.20: (a) Growth rates and (b) real frequencies versus temperature gradient $\eta_j$ for MTM $n = 23$ mode $\mu 2$ for the reversed shear $q^{WRS}$. $\eta_j$, $j = i, e$ is varied keeping the other fixed.

limits the lower $m$ coupling, these factors might be resulting in a destabilization.

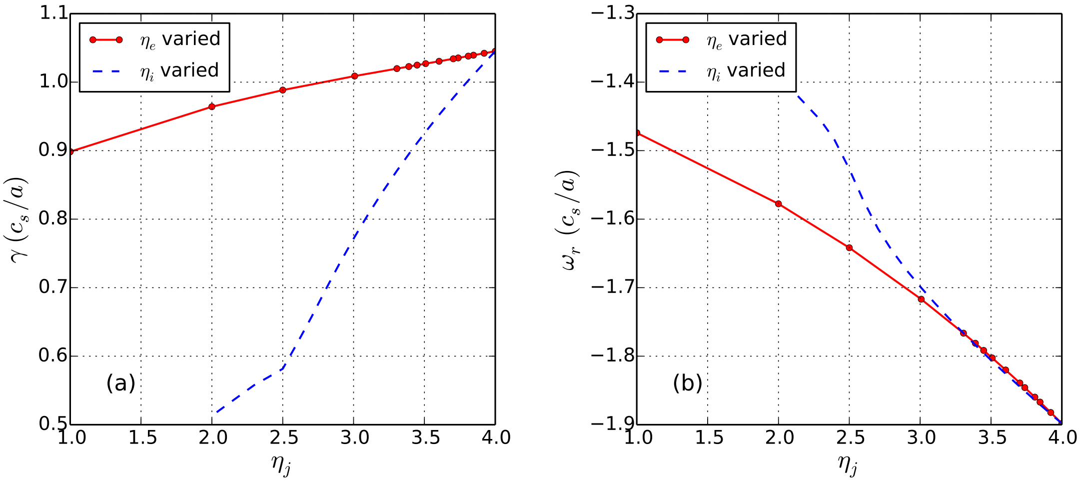


Figure 5.21: (a) Growth rates and (b) real frequencies versus temperature gradient $\eta_j$ for AITG $n = 23$ mode for the reversed shear $q^{WRS}$. $\eta_j,\ j = i, e$ is varied keeping the other fixed.

For the mode n=23, whose growth rate is near maximum for AITG and near to of the plateau for $\mu 2$ MTM, the dependence on the free energy source $\eta_j\ j = i, e$ is studied. Figs.5.20,5.21 shows the growth rates and real frequencies for MTM and AITG, respectively. The growth rates for MTM increase with increasing $\eta_e$ and are insensitive to changes in $\eta_i$ and have positive real frequency. The AITG mode n=23 is seen to be sensitive to ion temperature gradient and nearly insensitive to that of electrons. As seen earlier in Chapter 3 as well, these plots confirm the free energy dependence of these modes in weak reversed shear.

## 5.5 Dependence on plasma $\beta$

As described earlier, the plasma $\beta$ is an important performance parameter since fusion power $\propto \beta^2$, so that higher $\beta$ is desired for tokamak operation. However, existence of unstable electromagnetic microinstabilities would set in turbulence which would limit the confinement. Hence $\beta$ scaling studies are imporatant to understand electromagnetic turbulence. Fig. 5.22 shows the dependence of growth rates and

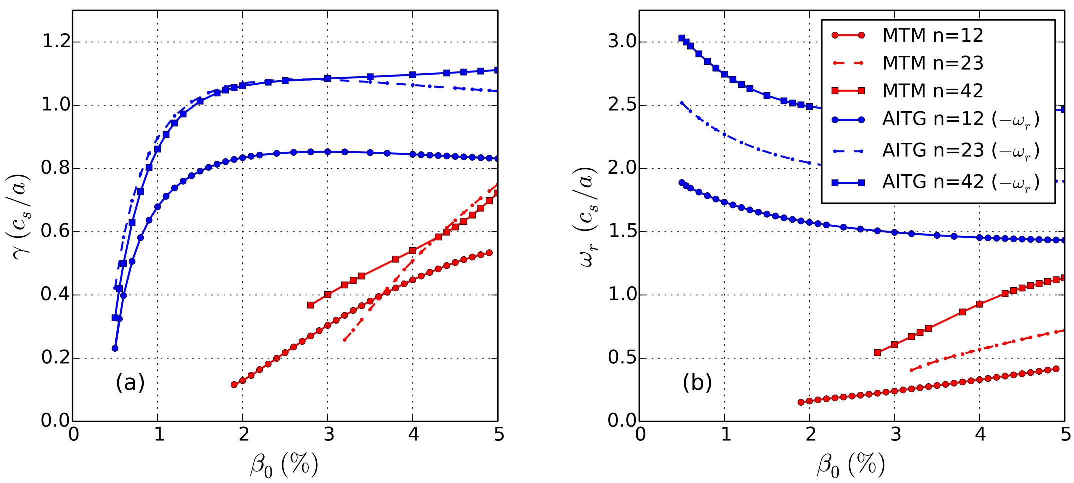


Figure 5.22: $\beta$ dependence of MTM and AITG instability in reversed shear profile $q^{WRS}$. The legend is shown in (b).

real frequencies of MTM and AITG on $\beta_0$ for weak reverse shear profiles. The temperature profile has a peak gradient of $\eta = 4$ at $s_0 = 0.6$. The growth rate decreases for lower lower $\beta_0$ values. The growth rates increase with increase in $\beta_0$. It is seen that MTM is unstable above a $\beta_{crit} \sim 1.5 - 3\%$ and that the thresholds are different for different toroidal mode numbers n, similar to that in regular $q$ profile in Chapter 4. Interestingly, $n = 44$ shows a slower rate of decrease of $\gamma$ for decreasing $\beta$. AITG modes, on the other hand, are seen to have a same $\beta_{crit}$ for different $n$, with $\beta_{crit} \sim 0.6\%$.

## 5.6 Radial location of MTM in reference $q$-profile and weak reversed shear case

Collisionless MTM driven by passing particles has been studied extensively and discussed in Chapter. 3. In Chapter 3, it was seen that the mode is sensitive to global temperature profiles. For thinner T profiles, the mode moves to $s_0$ . The eigenvalues change by about 25% within the range of study. The mode is primarily

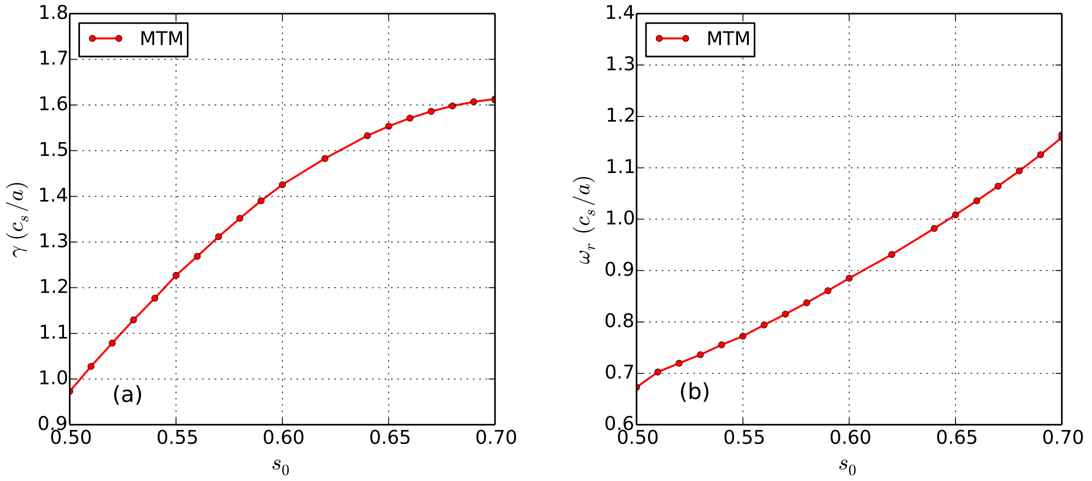


Figure 5.23: MTM growth rates for $n = 12$ for regular $q$ profile as $s_0$, the location of $\eta_{max}$, is changed.

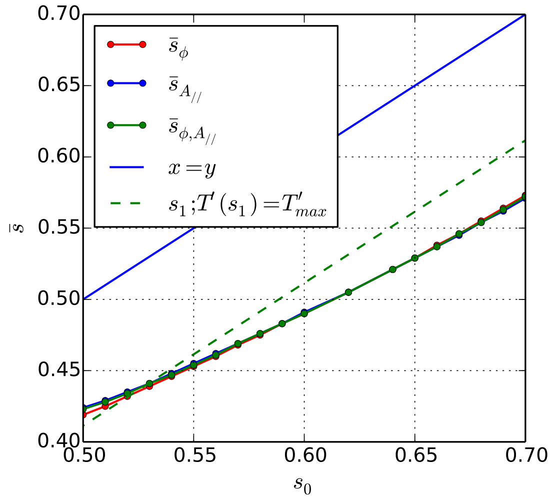


Figure 5.24: Mean radial location of MTM for $n = 12$ mode for regular $q$ profile as $s_0$ is changed.

destabilized by the magnetic drift of the passing electrons arising due to the tokamak magnetic field configuration. The separation of the Mode Rational Surfaces (MRS) is approximately $1/(nq\hat{s})$, where $n$ is the toroidal mode number, $q$ is the safety factor. The cross-field drift of the electrons causes coupling of the MRSs. The global results show that the mode is located about a radial location closer to the axis and away from $s_0$, even though $q, \hat{s}$ is lower and thus the MRS separation is relatively large in that region. On the other hand, ITG in electrostatic studies has typically been found at the location where $\eta$ is maximum [49, 84]. Also, as noted earlier, the mode appears slightly inwards of $s_0$, which is the location of $\eta_{max}$. At the mean radial location of the mode, the temperature $T$, $dT/ds$ is higher. Thus localization towards lower radius indicates the effect of $dT/ds$ relative to $\eta$. Since the mode is destabilized by the finite orbit width of electrons, it may be surmised that the mode appears in a higher T or $dT/ds$ region at the expense of $\hat{s}$. It is thus of interest to investigate whether it is the free energy drive that controls the location or the safety factor or shear.

For a given standard/regular $q(s)$ profile, with magnetic shear $\hat{s} = 1$ at $s = 0.5$, the temperature profile is varied by shifting radially inward/outward by changing $s_0$. The location of $s_0$ for density is also varied concurrently so that the $\eta$ peaks at the chosen $s_0$. The temperature at $s_0$ remains fixed at $T_0$, while the logarithmic gradient $a/L_T$, which is the free energy source, has an identical fall on either side of $s_0$. The results are shown in Fig. 5.23 and 5.24. It is observed that the MTM growth rate increases as $s_0$ is increased, confirming the earlier reports of the instability occurence in higher magnetic shear region. The AITG growth rate, on the other hand, is seen to be fairly insensitive to this profile variation. Thus, while MTM is seen to draw free energy from the electron temperature gradient, the mode is more unstable if the "same" temperature profile is located in higher shear region. The mode is observed to be located somewhat inwards of $s_0$. A plot of the mode location versus $s_0$ in Fig. 5.24 shows that the mode remains located in a higher temperature and $dT/ds$ region, but moves out linearly with the change in $s_0$.

The $\mu 2$ MTM mode is observed to locate in a region away from the $q_{min}$ region, where the $dT/ds|_{max}$ is located, unlike the $\mu 1$ at regular shear profile. Hence, the role of global temperature profile on the $\mu 2$ MTM is studied by shifting $s_0$, which radially shifts the $\eta$ profile. With $\beta = 5\%$ and a peak $\eta = 4$, the $n = 23$ mode is studied and shown in Fig.5.25. It is observed that the mode remains localised about

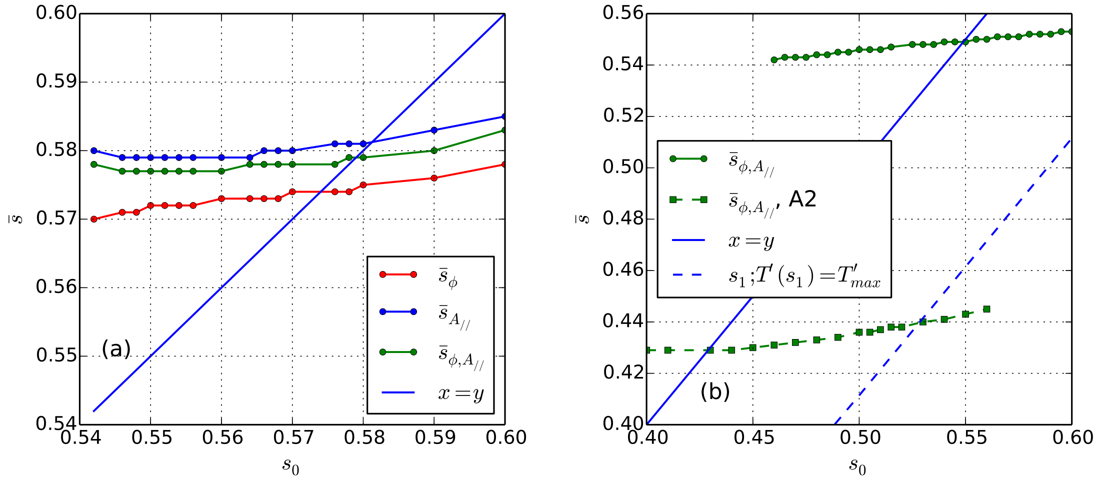


Figure 5.25: Mean radial location of MTM and AITG modes for $n = 23$ as $s_0$ is changed for WRS profile. The AITG mode unstable in the negative shear region is labeled $A2$ (right).

$s \simeq 0.58$ as obtained from the mode-averaged location $\bar{s}_{\phi,A_\parallel}$. This is unlike the $\mu 1$ at regular shear, which moves with $s_0$. Fig. 5.26 shows that the growth rate decreases as $s_0$ is decreased. Since $dT/ds|_{max}$ is moving inwards as $s_0$ is decreased, whereas the mode is localized about $s \simeq 0.58$, the $dT/ds$ at the location of the mode decreases, hence the mode is stabilized in the absence of the free energy source. Figs. 5.25(b) and 5.27 show the results of $s_0$ scan for AITG. The AITG mode labelled $A2$ is found unstable in the negative shear region, when the temperature profile is such that $\eta$ peaks in the negative shear region. Both the AITG modes are seen to remain at nearly same mean radial location $\bar{s}$ as $s_0$ is moved.

## 5.7 Conclusion

Steady state operation is a necessary requirement for a Tokamak fusion reactor. Significantly improved confinement is required for a steady state operation. Several advanced scenarios with improved confinement have been envisaged for ITER based on experiments in existing tokamaks such as JET, JT-60U, DIII-D. These advanced

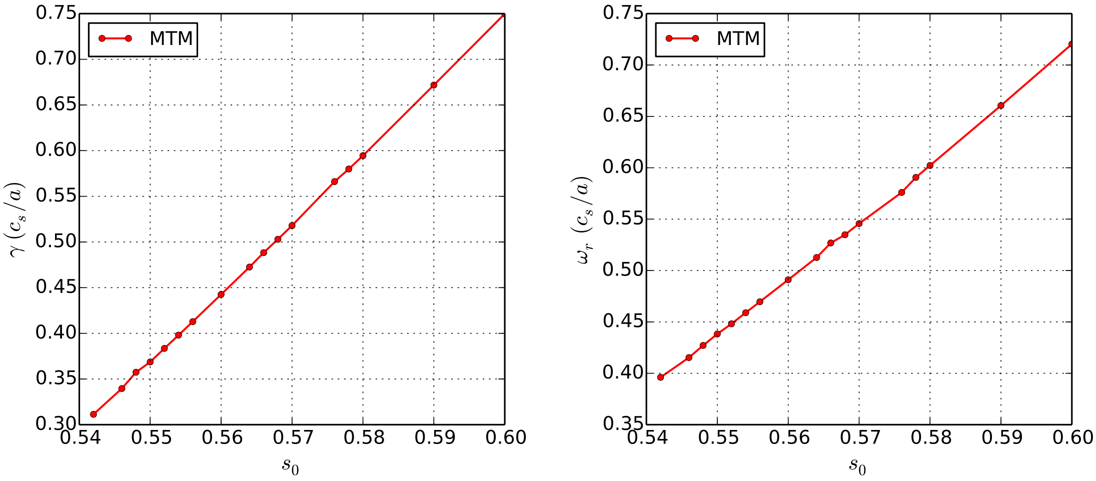


Figure 5.26: MTM growth rates for $n = 23$ as $s_0$ is changed for WRS profile.

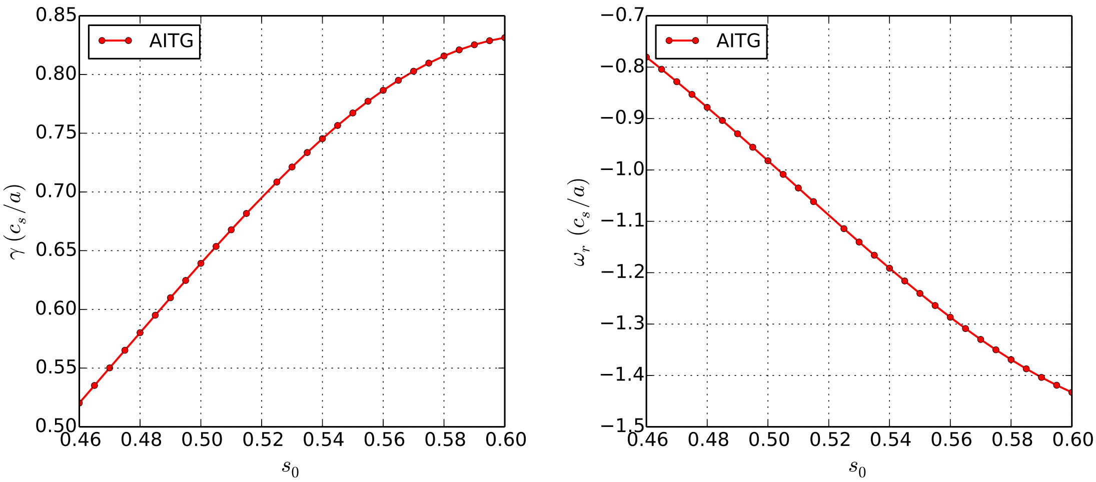


Figure 5.27: Growth rates and real frequencies $s_0$ is changed for AITG $n = 12$ mode found in the positive shear region in WRS profile.

tokamak scenarios include a reversed shear configuration in which plasma current is driven completely by non-inductive sources, and a hybrid scenario with near-zero shear in much of the core region. The formation of ITB in weak reversed shear configuration near the $q_{min}$ region is found to result in significantly improved confinement.

Since turbulent transport is one of the limiting factors in all these scenarios, a detailed understanding of the microinstabilities that generate microturbulence is of immense importance. In general, microinstabilities have been found to be suppressed by weaker magnetic shear.

Microtearing modes, previously considered unimportant in collisionless hot plasmas have been found unstable from recent gyrokinetic numerical investigations in several MCF devices considering experimentally relevant plasma parameters and MCF configuration. For this reason, study of MTM as a possible electron channel of transport has recently gathered momentum [3, 20, 45, 65, 38].

In this Chapter, global linear characteristics of collisionless MTM is investigated in detail for the regular and weak reverse shear profiles, with the main findings as follows:

- A systematic approach to arrive at the equilibrium profiles used in the study is adopted, based on the global linear characteristics of the mode in the regular monotonic $q$-profile. MTM is found to be sensitive to the global temperature profiles in Chapter 3. It was also found unlike ITG and ETG, the mean radial location for collisionless MTM is different from the location of $\eta_{max}$. The mode is found to localize in the region near $dT/ds|_{max}$.

- Considering a monotonic $q$-profile, a variation of the temperature profile by radially displacing the location of $dT/ds|_{max}$ outward, shows that (i) $\gamma$ increases suggesting that MTM is destabilized by higher shear, (ii) the mean radial location correlates to the location of $dT/ds|_{max}$.

- Considering the above results, the equilibrium profiles are chosen as follows: A weak shear with $q(0) = 3.0$, $q_{min} = 2$ at $s = 0.5$ and $q(q) \simeq 5.5$ is considered. A temperature profile of the form in Table. 3.1 with $s_0 = 0.6$ so that $\eta_{max}$ is at $s_0$ and $dT/ds|_{max}$ is at the location of $q_{min}$. Global characteristics of a given toroidal mode $n$ is studied with the value of $q$ at $s = 0.5$ kept constant so that in the reference scenario, $q = 2$ at the mean radial location of the mode $s = 0.5$, whereas in the WRS profile, $q = q_{min} = 2$ at $s = 0.5$. In this way, the location of a reference mode rational surface $q = m/n$ is unchanged. Temperature profile is also unchanged so that the free energy drive, at least at the mean radial location of the mode for reference $q$ profile is constant.

- In Chapter 4, it was seen that the trapped electron dynamics is negligible at low toroidal mode numbers at large aspect ratio, for monotonic $q$ profile. Hence, $n = 12$ is considered and a scan in the global $q$ profiles with the above constraints is performed. Two branches of MTM and an AITG branch are studied in particular, though several other unstable eigenmodes exist. The results show that MTM is sensitive to changes in global $q$ profiles. The most dominant eigenmode is less unstable as shear reduces.

- Multiple unstable mode branches are found as shear is varied at $s = 0.5$. Following these branches as a function of reducing shear $\hat{s}$, a gradual loss of clear tearing parity with a conversion to mixed parity in $\tilde{\varphi}$ and $\tilde{A}_{\parallel}$ is observed.

- Subdominant branches are seen to become more unstable as shear reduces. The modes remain unstable at $\hat{s} = 0$ with tearing parity structures, after peaking at $\hat{s} \simeq 0.5$. The mean radial location of this branch is seen to be near $s \simeq 0.6$, outside the $q_{min}$ region.

- The wave number spectrum of the $\mu 2$ branch in WRS profiles show that the spectrum of instability extends to shorter wavelengths or mesoscale, with higher $n$ being similarly unstable within the range studied.

- An identical study of AITG shows that AITG growth rates are relatively less sensitive to profile changes. Similar to MTM, the shorter wavelengths are more unstable within the range studied. For the same weak reverse shear profile and temperature profile, the AITG is seen to be more unstable, without trapped electrons. MTMs were not found to localize deep in the negative shear region, while an AITG eigenmode is unstable in the negative shear region.

- The characteristic nature of MTM and AITG are verified for their different sensitivity to iTG and eTG in WRS profile as well. A change in the radial location of $\eta$ profile in WRS reveals that the mean radial location of the $\mu 2$ branch remains characteristically anchored about $s \simeq 0.58$. Similarly, the AITG branches remain anchored about $s \simeq 0.54$ and $s \simeq 0.0.43$ in the positive and negative shear regions respectively.

- The $\beta$ scaling of AITG and $\mu 2$ reveal that AITG has a lower $\beta_{crit} \sim 0.5\%$, below the ideal MHD limit, while MTM $\mu 2$ modes have different $\beta_{crit}$ for different $n$ with $\beta_{crit} \sim 1.5\% - 3\%$, without trapped electrons.

- Even without including trapped electrons,

The trapped electron contribution has been seen to be ineffective at low toroidal mode numbers $n \sim 8 - 15$ (Fig. 4.1). Nevertheless, their dynamics is also sensitive to the local value of shear at each radial location. Though not attempted in this thesis, it is important to address the role of trapped electrons on MTM in these different magnetic shear scenarios.

# Chapter 6

# Conclusion

Understanding and predicting turbulent transport is a key issue in the development of Tokamaks as fusion reactors, since transport is one of the important limiting factors of confinement of the plasma. In an MHD stable plasma, microinstabilities lead to the generation of microturbulence driven transport and degradation of confinement. Hence understanding microinstabilities is of immense importance for steady state devices or fusion reactors. The development of gyrokinetic framework and of numerical codes to solve the gyrokinetic equations have helped in obtaining an insightful understanding of turbulent transport [7]. In the (simplified) limit of negligible plasma pressure (and hence magnetic fluctuations), local and global numerical simulations now closely consider experimental plasma parameters and magnetic geometry. In particular, several features of ion-Larmor scale instabilities and ensuing transport are now well understood from these simulations. However, hot Tokamak plasmas have a non-negligible plasma pressure or $\beta$. At finite $\beta$, the magnetic perturbations become significant, which alter the linear and non-linear characteristics of these microinstabilities. Also, new electromagnetic modes have been observed to emerge unstable above respective threshold value of $\beta$. Hence, not only electrostatic, but electromagnetic gyrokinetic study of microinstabilities is indispensable in developing an understanding of turbulent transport. In particular, Kinetic Ballooning modes, or Alfv̀en-ITG modes have been found unstable in the presence of ion temperature gradient above a threshold $\beta$. This mode has ballooning parity i.e. $\phi$ fluctuations being even in $\theta$ and $A_\|$ fluctuations being even in $\theta$ leading to leads to ion heat transport via magnetic flutter. The tearing parity modes, i.e. modes with odd $\phi$ and even $A_\|$ fluctuations, cause small-scale stochasticization of the underlying magnetic field topology near mode rational surfaces and thereby lead to transport when several magnetic structures overlap. At finite $\beta$, subdominant tearing parity ITG modes have been found to take part in transport via non-linear interaction with unstable modes and leading to their saturation [20, 90].

Microtearing modes, which are high-$n$ analogues of the conventional tearing modes were studied in simple geometries in the 70s and found unstable driven by electron temperature gradient and sustained by the electron-ion collisions. However, due to the collisionless regime of hot plasmas in modern tokamaks, these modes were thought to be unimportant. Hence, study of electron channel of transport has focused on ETG and TEM turbulence, within the electrostatic gyrokinetic framework. TEM turbulence is excited at ion-Larmor scales in the presence of pressure gradient and is unaffected by $\beta$ [17]. ETG modes appear at much shorter length scales of the order of electron-Larmor radii and become important for transport in conditions in which streamers are formed [8].

With the development of advanced electromagnetic codes that consider realistic tokamak geometry and plasma parameters in present day experiments, collisional MTMs have been found unstable in Spherical Tokamaks and subsequently in other MCF configurations as well. Global gyrokinetic simulations in [46], with finite collisionality found MTMs unstable in Standard Tokamaks. Electromagnetic simulations that consider non-adiabatic electron dynamics reported unstable collisionless MTMs as well in Spherical Tokamaks [39]. These were attributed to the drive mechanism of drift resonance of trapped electrons. These local flux-tube simulations, in $s-\alpha$ geometry and at small but finite collisionality, considering a scaling of $R$, expected the modes to be unstable at large aspect ratio. However, a detailed study was not carried out until the advent of this thesis, which carries out a collisionless, global, fully electromagnetic gyrokinetic simulation of MTM including profile variation physics, amongst others.

## 6.1 Results

Collisionless MTMs were found unstable in large aspect ratio tokamaks as part of this work. The characteristics of MTM and another electromagnetic mode namely AITG are investigated in detail in this thesis for large aspect ratio tokamaks. The gyrokinetic code EM-GLOGYSTO used in the past to study global linear characteristics of electrostatic and electromagnetic microinstabilities with full non-adiabatic ions and electrons was numerically optimized to improve runtime and handle, high resolution spanning ion-Larmor scale to electron-Larmor scale. This enabled the study of multi-scale modes such as MTM. By implementing hybrid MPI-OpenMP parallelization to the existing MPI code, better utilisation of the present-day multi-core architectures as well as a further speedup was achieved.

The important findings of the global linear characteristics of the electromagnetic instabilities MTM and AITG through this thesis are listed in the following paragraphs, followed by the scope for further work to obtain improved understanding of these instabilities.

In Chapter 3, linear full radius gyrokinetic calculations show the existence of unstable microtearing modes in purely collisionless, high temperature, large aspect ratio tokamak plasmas. The studies presented in this Chapter takes into account fully gyrokinetic highly passing ions and electrons. In this work presented in this

Chapter, the trapped electrons are not considered, enabling one to delineate the effects of their dynamics from that of passing particles. The global 2-D structures of the collisionless mode with full radius coupling of the poloidal modes is obtained and compared with another electromagnetic mode, namely the Alfvén ITG Mode (or Kinetic Ballooning Mode) for the same equilibrium profile. A clear symmetry swap of the two modes, the plasma - $\beta$ dependence and radial and poloidal length scales of the electrostatic and magnetic vector potential fluctuations, scaling of the growth rate with $\beta$ and the electron temperature gradient $\eta_e$ are obtained.

The main findings are the following:

- Completely collisionless unstable Microtearing Modes are found in large aspect ratio hot tokamaks in the finite temperature gradient region with a finite-$\beta$ plasma for a broad range of relevant parameters. ($\beta \sim 1\% - 5\%$, $a/L_{Te} \sim 1.5 - 12.5$). Electron magnetic drift resonance of the passing electron population is shown to be the main destabilizing mechanism. The aspect ratio considered was $A = 4$.

- Global 2D mode structures are obtained for MTM. For the same equilibrium profiles and parameters, co-existing AITG modes are also found and co-located in the radial direction. Profile variation studies at the system parameters considered, show that the mode structures and the linear growth rate depend strongly on the equilibrium density and temperature gradient width.

- The MTM and AITG modes exhibit appropriate parities. Real and imaginary parts of $A_{\|}$ of all the poloidal modes which constitute the global mode structure show even parity (tearing parity) about the mode rational surfaces in case of MTM and odd parity in case of AITG. On the other hand, $\tilde{\varphi}$ fluctuations show the opposite parity. $\tilde{\varphi}$ fluctuations of the AITG mode exhibit sharp structures near the MRSs due to inclusion of non-adiabatic electrons. This is the first time the radial features of MTM has been brought to the fore, importantly the tearing parity along the radial direction. Along the poloidal direction $\hat{\theta}$, a symmetry swap in the $r$-averaged mode structure is observed between MTM and AITG.

- The mode spectrum is characteristically mesoscale, extending to shorter wavelength than the typical ion-scale modes. For example, mode averaged wavenumbers are $\overline{k}_\theta \rho_i \sim 0.75 - 2.5$, and $\overline{k}_\perp \rho_i \sim 1.0 - 4.0$.

- Linear growth rates from $n$-scan and $\beta$ - scan for $\eta_{e,i} = 4$ show that if trapped electrons are neglected, MTMs are more unstable than AITG. MTM becomes unstable for $\beta \simeq 3\%$ and the growth rate monotonically increases with $\beta$ beyond this value. The MTM growth rate increases with $\eta_e$ for a given $\eta_i$ whereas for a constant $\eta_e$, variation in $\eta_i$ has minimal effect. Steeper electron temperature gradient is one of the crucial factors for the mode to be unstable.

- Parallel magnetic field perturbations were found to have only a marginal influence on the linear growth rates and $\beta$ threshold and hence were not studied in detail.

- A clear inverse relationship between $\eta_{e,i}^{crit}$ and $\beta$ is seen. In large aspect ratio machines, at low $\beta$, it can be expected that MTM would become unstable at large $\eta_{e,i}$ and vice-versa, resulting in a stability diagram in the $\beta$-$\eta_{e,i}$ space.

- Real frequency shows a clear and strong dependence on different parameters, including $\beta$ and $\eta_e$ and increases almost linearly with $\eta_e$, in agreement with the predictions of [30].

- In contrast to small aspect ratio collisional tokamaks where the trapped electron magnetic drift resonance is found to be important, in large aspect ratio tokamaks, a strong destabilization due to the magnetic drift resonance of passing electrons is observed and is identified as a possible collisionless drive mechanism for the collisionless MTM.

- Electron Landau Resonance weakly damps MTM. Further, phase velocity obtained from the mode-averaged parallel wavenumber is found to disparate from thermal velocities, $\omega/\overline{k}_{\parallel} > v_{th}$. An interplay with transit resonance harmonics is seen. Ion Landau resonance is also found to be ineffective and so is ion drift resonance.

Thus, this thesis unambiguously demonstrates for the first time, that MTM can be unstable in purely collisionless limit in large aspect ratio hot Tokamaks. The instability is shown to be driven by magnetic drift resonance of passing non-adiabatic electrons in the presence of electron temperature gradient. The ion temperature gradient is found to be unimportant. The mode size is several ion scales large, though driven by electron dynamics and hence truly muntiscale in nature. It is found that at high $\beta$, the $\eta_{crit}$ is lower and vice versa.

In Chapter 4, the contribution of non-adiabatic trapped electron dynamics on the Microtearing instability was studied by considering a drift kinetic equation and obtaining a bounce period-averaged contribution to the electrostatic potential fluctuations. The main findings are the following:

- The trapped electrons are found to contribute to electrostatic fluctuations $\tilde{\varphi}$ via a resonant toroidal precessional drift and further destabilize MTMs driven by passing nonadiabatic electrons. This is observed to lead to the creation of more localised and sharper gradient regions of $\tilde{\varphi}$ fluctuations near the mode rational surfaces. The radial spectrum $n_r$ broadens with the inclusion of trapped electrons.

- The aspect ratio scan within a finite range by varying the major radius $R$ shows that the trapped electron destabilization significantly adds to the passing electron drive, at lower aspect ratios, substantially altering the growth rates.

- At a given aspect ratio and plasma $\beta$, the resonant destabilization is relatively more effective for the high-$n$ MTM modes than at low $n$ modes.

- The $\beta$ threshold for the onset of the instability with only passing electrons is found to be lower for the low $n$ modes. The non-adiabatic trapped electron drive further downshifts the threshold.

- The ratio of the strength of the magnetic vector potential and electrostatic potential fluctuations is seen to be strongly dependent on $k_\theta \rho_i$ and plasma pressure $\beta$.

Thus, for large aspect ratio, the inclusion of trapped electron physics does not affect the MTM growth rates for intermediate to low toroidal mode numbers. However, MTMTE growth rates are higher and the spectrum extends to shorter scales, or higher $n$, than without trapped electrons. For an intermediate $n$ value, an aspect ratio scan demonstrates that trapped electrons affect the growth rates at lower aspect ratios. This is consistent with the findings for weakly collisional MTMs obtained in Spherical Tokamaks, where the trapped electrons were suggested to be more important. Inclusion of trapped electrons significantly increases the computational resoure requirement as shorter scale structures are introduced in $\tilde{\varphi}$.

In Chapter 5, the global characteristics of MTM and AITG in weak reversed shear configuration is addressed, which is one of the Advanced Tokamak Scenarios with improved confinement that have been envisaged for ITER encouraged by experiments in existing tokamaks such as JET, JT-60U, DIII-D. To reduce the computational demand, the modes are studied considering only passing particles, which also helps delineate the passing particle dynamics from that of trapped particles. The main findings as follows:

- In the regular monotonic $q$-profile, such as the one studied in Chapter 3, MTM is found to be sensitive to the global temperature profiles. Unlike ITG and

ETG, that the mean radial location is different from the radial location of $\eta_{max}$. The mode is found to localize in the region near $dT/ds|_{max}$, where $T(s)$ is the equilibrium temperature profile.

- Considering a monotonic $q$-profile, a radially outward displacement of the location of $dT/ds|_{max}$ shows that (i) $\gamma$ increases suggesting that MTM is destabilized by higher shear, (ii) the mean radial location correlates to the location of $dT/ds|_{max}$.

- Considering a weak reversed shear (WRS) profile with $q(0) = 3.0$, $q_{min} = 2$ at $s = 0.5$ and $q(q) \simeq 5.5$ and a temperature profile with $\eta_{max}$ at $s_0 = 0.6$ and $dT/ds|_{max}$ at the location of $q_{min}$, sensitivity of a given toroidal mode, say $n = 12$, to global $q$-profiles is studied by a continuous change of $q$-profile from the reference scenario monotonic $q$-profile to the WRS profile. The value of $q$ at $s = 0.5$ is kept constant so that in the reference scenario, $q = 2$ at the mean radial location of the mode $s = 0.5$, whereas in the WRS profile, $q = q_{min} = 2$ at $s = 0.5$. In this way, the location of a reference mode rational surface $q = m/n$ is unchanged.

- Multiple MTM and AITG mode branches are found unstable at these profiles, among which two branches of MTM (labelled $\mu 1$ and $\mu 2$)and an AITG branch are studied in particular. The results show that MTM is sensitive to changes in global $q$ profiles. The most dominant eigenmode is less unstable as shear reduces.

- As a function of reduced shear, a gradual loss of clear tearing parity is observed, with a conversion to mixed parity in $\tilde{\varphi}$ and $\tilde{A}_{\|}$.

- Subdominant branches are seen to become more unstable as shear reduces. The modes remain unstable at $\hat{s} = 0$ with tearing parity structures, peaking at $\hat{s} \simeq 0.5$. The mean radial location of the $\mu 2$ branch is seen to be near

$s \simeq 0.6$, outside the $q_{min}$ region.

- The wave number spectrum of the $\mu 2$ branch in WRS profiles show that the spectrum of instability extends to shorter wavelengths or mesoscale, with higher $n$ being similarly unstable within the range studied.

- An identical study of AITG shows that AITG growth rates are relatively less sensitive to profile changes. Similar to MTM, the shorter wavelengths are more unstable within the range studied. For the same WRS and temperature profile, the AITG is seen to be more unstable, without trapped electrons. In this thesis, MTMs were not found to localize deep in the negative shear region, while an AITG eigenmode is unstable in the negative shear region.

- The characteristic nature of MTM and AITG are verified for their different sensitivity to ion temperature gradient and electron temperature gradient in WRS profile as well. A change in the radial location of $\eta$ profile in WRS $q$-profile reveals that the mean radial location of the $\mu 2$ branch remains characteristically anchored about $s \simeq 0.58$. Similarly, the AITG branches remain anchored about $s \simeq 0.54$ and $s \simeq 0.0.43$ in the positive and negative shear regions respectively.

- The $\beta$ scaling of AITG and $\mu 2$ reveal that AITG has a lower $\beta_{crit} \sim 0.5\%$, below the ideal MHD limit, while MTM $\mu 2$ modes $\beta_{crit} \sim 1.5\% - 3\%$, without trapped electrons.

- This thesis does not conclude that MTMs survive only in the positive shear region. The trapped electron dynamics is known to be affected by magnetic shear and a shear scan including their contribution would shed more light on MTM instability, but is not carried out in this thesis. A more comprehensive work needs to be done to establish the relevance of MTMs in the negative shear region in such configurations.

## 6.2 Scope for future work

Completely collisionless MTMs are shown to be unstable in large aspect ratio hot Tokamaks in this thesis. The magnetic drift resonance of passing electrons is shown to be the reason for the destabilization. The model used has several approximations.

- Large aspect ratio, circular flux surface equilibrium at the temperature gradients $\eta$ and plasma $\beta$ are usually subject to equilibrium Shafranov shift effects. However, in this thesis, this effect is not considered. Taking cue from the Spherical Tokamak studies in weakly collisional limit using flux-tube geometries, which naturally include Shafranov shift, one may argue that the mode could be unstable even after the inclusion of Shafranov shift. One may also argue that in a global analysis, the differential Shafranov shift as a function of radius could stabilize collisionless MTMs. Also, recent nonlinear global collisional MTM studies indicate that the modes may remain unstable even in a global calculation such as this one, if Shafranov shift is included. A detailed study including Shafranov shift is desirable and needs to be done.

- The “equilibrium profiles” $n(r)$ $T(r)$ and $q(r)$ are chosen to be typical of Tokamak experiments. However, as indicated at several places in the thesis, they are not obtained by solving the exact Grad-Shafranov equation resulting out of MHD radial force balance. To this extent, the large scale MHD equilibrium as considered in this study are “ad hoc”.

  As the modes studied are short scale, low frequency modes, it is believed that the qualitative nature of these results should not seriously be altered by using exact MHD profiles for $n(r)$ $T(r)$ and $q(r)$. In the light of recent work by X. Lapillonne *et al.* [91], where the nature of equilibrium is shown to be important in altering microinstability, it is perhaps worthwhile to consider correct MHD equilibrium and redo the present studies.

- For the shear profile studies in Chapter 5, the present studies ignore the role of trapped electrons. However, it is well known that magnetic shear affects the pure TEM modes and ITG-TEM modes. Thus it may be expected to bring important qualitative and quantitative changes to MTM studies reported here for shear studies.

  The relation between the collisionless MTM branch presented in this thesis and the collisional MTM branch in both the core and edge, in the limit of zero collisionality also needs to be explored.

- A system size scaling of the MTM in reversed shear configuration is also an important work to gain insight on global profile effects in advanced scenarios.

- The underlying model has several areas where improvement is possible. In particular, the passing particles are considered highly passing, i.e. the modulation of parallel velocity $v_{\|}$ as the particles pass through the high field region is ignored. On the other hand, the trapped electrons are considered as deeply trapped. Thus the contribution due to the dynamics of particles in the trapped-passing boundary needs to be addressed. The presence of self-generated flows is known to affect linear stability and non-linear saturation of microinstabilities, which needs to be incorporated. The equilibrium particle distribution function is assumed to be Maxwellian, i.e. a distribution dependency on the adiabatic invariant is not considered and depends solely on the energy. To incorporate these important effects, construction of a numerical propagator solution to correctly span the phase-space is in order.

# Bibliography


[1] Tokamaks, J. Wesson, Oxford Publications 2011

[2] Fusion Physics, M. Kikuchi, L. Lackner, M. Q. Tran, IAEA (2012)

[3] M. Kikuchi and M. Azumi, Rev. Mod. Phys. 84, 1807 (2012)

[4] The Science of JET, J. Wesson, 2000

[5] ITER Physics Expert Group, 1999, Nucl. Fusion 39, 2175.

[6] W M Tang, V S Chan, Plasma Phys. Control. Fusion 47 (2005)

[7] X. Garbet, Y. Idomura, L. Villard and T.H. Watanabe, Nucl. Fusion 50 (2010)

[8] Progress in the ITER Physics Basis, Nucl. Fusion 47 (2007)

[9] L. I. Rudakov and R. Z. Sagdeev, Nucl. Fusion Suppl. 2, 481 (1962).

[10] W. Horton, B. G. Hong, and W. M. Tang, Phys. Fluids 31 , 2971 (1988).

[11] B. B. Kadomtsev and O. P. Pogutse, Nucl. Fusion 11, 67 (1971).

[12] J. Y. Kim, W. Horton and J. Q. Dong, Phys. Fluids B 5, 4030 (1993)

[13] Brizard A.J. and Hahm T.S. 2007 Rev. Mod. Phys. 79 421

[14] John R. Cary and Alain J. Brizard, Rev. Mod. Phys., Vol. 81, No. 2, April - June 2009

[15] Dimits A.M. et al 2000 Phys. Plasmas 7 969

[16] J. Chowdhury, R. Ganesh, P. Angelino, J. Vaclavik, L. Villard, and S. Brunner, Phys. Plasmas 15, 072117 (2008)

[17] E. A. Belli and J. Candy, Phys. Plasmas 17, 112314 (2010)

[18] G. L. Falchetto, J. Vaclavik and L. Villard, Phys. Plasmas **10**, 1424, (2003)

[19] R. Ganesh, P. Angelino, J. Vaclavik and L. Villard, Phys. Plasmas, **11**, 3106 (2004)

[20] P.W. Terry, D. Carmody, H. Doerk, W. Guttenfelder, D.R. Hatch, C.C. Hegna, A. Ishizawa, F. Jenko, W.M. Nevins, I. Predebon, M.J. Pueschel, J.S. Sarff and G.G. Whelan, Nucl. Fusion 55 (2015) 104011

[21] Rechester A.B. and Rosenbluth M.N. 1978 Phys. Rev. Lett. 40 38

[22] T. H. Stix, Phys. Rev. Lett. 30, 833 (1973)

[23] S. A. Colgate and H. P. Furth, Phys Fluids 3, 982 (1960)

[24] J W Dungey, Cosmic Electrodynamics, Cambridge University Press, New York, 1958, pp 98-102

[25] Furth, Killeen and Rosenbluth, Phys Fluids, 6 (4) 459, (1963)

[26] R. D. Hazeltine, D. Dobrott, and T. S. Wang, Phys. Fluids 18, 1778 (1975).

[27] Hazeltine and Strauss, PRL, 37, 102 (1976)

[28] J. F. Drake and Y. C. Lee, Phys. Fluids 20, 1341 (1977).

[29] Drake, Gladd, Liu, Chang, Phys Rev. Lett, 44, 994 (1980)

[30] P. J. Catto and M. N. Rosenbluth, Phys. Fluids 24, 243 (1981).

[31] Cowley S C, Kulsrud R M and Hahm T S 1986 Phys. Fluids 29 3230

[32] Connor J W, Cowley S C and Hastie R J 1990 Plasma Phys. Control. Fusion 32 799

[33] D J Applegate *et al* Phys. Plasmas 11, 5085 (2004)

[34] Kotschenreuther M, Rewoldt G and Tang W M 1995 Comput. Phys. Commun. 88 128

[35] D. J. Applegate, C. M. Roach, J W Connor, S C Cowley, W Dorland, R J Hastie, and N Joiner, Plasma Phys. Controlled Fusion 49(8), 1113 (2007).

[36] F. Jenko, W. Dorland, M. Kotschenreuther, and B. N. Rogers, Phys. Plas- mas 7, 1904 (2000).

[37] D Told et al, 15 102306 Phy. Plasmas (2008)

[38] D. Dickinson, C. M. Roach, S. Saarelma, R. Scannell, A. Kirk, and H. R. Wilson, Phys. Rev. Lett. 108, 135002 (2012)

[39] D Dickinson, C M Roach, S Saarelma, R Scannell, A Kirk and H R Wilson, Plasma Phys. Control. Fusion 55 (2013) 074006

[40] W. Guttenfelder, J. Candy, S. M. Kaye, W. M. Nevins, E. Wang, R. E. Bell, G. W. Hammett, B. P. LeBlanc, D. R. Mikkelsen, and H. Yuh, Phys. Rev. Lett. 106, 155004 (2011)

[41] J. Candy and R. E. Waltz, Phys. Rev. Lett. 91, 045001 (2003)

[42] J. Candy and R. E. Waltz, J. Comput. Phys. 186, 545 (2003).

[43] I Prebedon et al, PRL, 105, 195001 (2010)

[44] I. Predebon and F. Sattin, Phys. Plasmas 20, 040701 (2013)

[45] H. Doerk, F. Jenko, M. J. Pueschel, and D. R. Hatch, Phys. Rev. Lett. 106, 155003 (2011)

[46] H. Doerk, F. Jenko, T. Görler, D. Told, M. J. Pueschel, and D. R. Hatch, Phys. Plasmas 19, 055907 (2012)

[47] R. Ganesh and J. Vaclavik, Phys. Rev. Lett., 94, 145002 (2005)

[48] S. Brunner, M. Fivaz, T. M. Tran and J. Vaclavik, Phys. Plasmas. **5**(11), 3929 (1998)

[49] S. Brunner, Ph.D thesis, EPFL, Switzerland, Thesis no : 1701 (1997)

[50] G. L. Falchetto, Ph.D thesis, EPFL, Switzerland, Thesis no : 2524 (2002)

[51] P. J. Catto, W M. Tang and D. E. Baldwin, Plasma Physics **23** (7), 639 (1981)

[52] P. Angelino, Ph.D thesis, EPFL, Switzerland, Thesis no : 3559 (2006)

[53] N. A. Krall and A. W. Trivelpiece, *Principles of Plasma Physics* (San Francisco Press Inc, San Francisco, CA 94101-6800, 1986) p: 396-397

[54] B. Davies, Jnl Comput. Physics 66, 36-49 (1986)

[55] R Ganesh, P Angelino, EPFL Supercomputing Review N$^o$.14, Jan 2014

[56] J. Chowdhury, R. Ganesh, S. Brunner, J. Vaclavik and L. Villard Phys. Plasmas 17, 102105 (2010)

[57] W. Dorland, F. Jenko, M. Kotschenreuther, and B. N. Rogers, Phys. Rev. Lett., 85, 5579 (2000)

[58] M. N. Rosenbluth and M. L. Sloan, Phys. Fluids 14, 1725 (1971).

[59] P. C. Liewer, Nucl. Fusion 25, 543 (1985).

[60] T. Dannert and F. Jenko, Phys. Plasmas 12, 072309 (2005)

[61] J. Chowdhury, R. Ganesh S. Brunner, J. Vaclavik, L. Villard, and P. Angelino, Phys. Plasmas, **16**, 052507 (2009)

[62] C. Bourdelle, W. Dorland, X. Garbet, G. W. Hammett, M. Kotschenreuther, G. Rewoldt, and E. J. Synakowski, Phys. Plasmas 10, 2881 (2003)

[63] A. Sykes, R. J. Akers, L. C. Appel, E. R. Arends, P. G. Carolan, N. J. Conway, G. F. Counsell, G. Cunningham, A. Dnestrovskij, Yu. N. Dnestrovskij, A. R. Field, S. J. Fielding, M. P. Gryaznevich, S. Korsholm, E. Laird, R. Martin, M. P. S. Nightingale, C. M. Roach, M. R. Tournianski, M. J. Walsh, C. D. Warrick, H. R. Wilson, S. You, MAST Team, and NBI Team, Nucl. Fusion 41, 1423 (2001)

[64] C. M. Roach, D. J. Applegate, J. W. Connor, S. C. Cowley, W. D. Dorland, R. J. Hastie, N. Joiner, S. Saarelma, A. A. Schekochihin, R. J. Akers, C. Brickley, A. R. Field, M. Valovic, and The MAST Team, Plasma Phys. Controlled Fusion 47, B323 (2005)

[65] K. L. Wong, S. Kaye, D. R. Mikkelsen, J. A. Krommes, K. Hill, R. Bell, and B. LeBlanc, Phys. Rev. Lett. 99, 135003 (2007)

[66] W. Guttenfelder, J. Candy, S. M. Kaye, W. M. Nevins, R. E. Bell, G. W. Hammett, B. P. LeBlanc, and H. Yuh, Phys. Plasmas 19, 022506 (2012)

[67] W. Guttenfelder, J. Candy, S. M. Kaye, W. M. Nevins, R. E. Bell, G. W. Hammett, B. P. LeBlanc, and H. Yuh, Phys. Plasmas 19, 056119 (2012)

[68] D. Carmody, M. J. Pueschel, and P.W. Terry, Phys. Plasmas 20, 052110 (2013)

[69] S. Moradi, I. Pusztai, W. Guttenfelder, T. Fülöp and A. Mollén, Nucl. Fusion 53 063025 (2013)

[70] Aditya K. Swamy, R. Ganesh, J. Chowdhury, S. Brunner, J. Vaclavik, and L. Villard, Phys. Plasmas 21, 082513 (2014)

[71] L. Vermare, C Angioni, A Bottino, A G Peeters and ASDEX Upgrade Team, J. Phys. Conf Series 123, 012040(2008)

[72] E. Wang, X. Xu, J. Candy, R.J. Groebner, P.B. Snyder, Y. Chen, S.E. Parker, W. Wan, Gaimin Lu and J.Q. Dong, Nucl. Fusion 52 (2012) 103015

[73] R.J. Groebner, C.S. Chang, J.W. Hughes, R. Maingi, P.B. Snyder, X.Q. Xu, J.A. Boedo, D.P. Boyle, J.D. Callen, J.M. Canik, I. Cziegler, E.M. Davis, A. Diallo, P.H. Diamond, J.D. Elder, D.P. Eldon, D.R. Ernst, D.P. Fulton, M. Landreman, A.W. Leonard, J.D. Lore, T.H. Osborne, A.Y. Pankin, S.E. Parker, T.L. Rhodes, S.P. Smith, A.C. Sontag, W.M. Stacey, J. Walk, W. Wan, E.H.-J. Wang, J.G.Watkins, A.E. White, D.G. Whyte, Z. Yan, E.A. Belli, B.D. Bray, J. Candy, R.M. Churchill, T.M. Deterly, E.J. Doyle, M.E. Fenstermacher, N.M. Ferraro, A.E. Hubbard, I. Joseph, J.E. Kinsey, B. LaBombard, C.J. Lasnier, Z. Lin, B.L. Lipschultz, C. Liu, Y. Ma, G.R. McKee, D.M. Ponce, J.C. Rost, L. Schmitz, G.M. Staebler, L.E. Sugiyama, J.L. Terry, M.V. Umansky, R.E.Waltz, S.M. Wolfe, L. Zeng and S.J. Zweben, Nucl. Fusion 53 (2013) 093024

[74] D R Smith, W Guttenfelder, B P LeBlanc and D R Mikkelsen, Plasma Phys. Control. Fusion 53 (2011) 035013

[75] R. E. Waltz, M. E. Austin, K. H. Burrell and J. Candy, Phys. Plasmas 13, 052301 (2006)

[76] J Dominski, S Brunner, S K Aghdam, T Görler, F Jenko and D Told, J. Phys.: Conf. Ser. 401 012006 (2012)

[77] J.M. Canik,W. Guttenfelder, R. Maingi, T.H. Osborne, S. Kubota, Y. Ren, R.E. Bell, H.W. Kugel, B.P. LeBlanc and V.A. Souhkanovskii, Nucl. Fusion 53 (2013) 113016

[78] Waltz R.E. et al 1997 Phys. Plasmas 4 2482

[79] T. Dannert and F. Jenko, Phys. Plasmas 12, 072309 (2005);

[80] J. Chowdhury, W. Wang, S. Ethier, J. Manickam and R. Ganesh, Phys. Plasmas 18, 112510 (2011)

[81] Nordman H., Weiland J. and Jarmen A. 1990 Nucl. Fusion 30 983

[82] Jenko F. and Dorland W. 2002 Phys. Rev. Lett. 89 225001

[83] A. Bottino, Ph.D thesis, EPFL, Switzerland, Thesis no : 2938 (2004)

[84] J. Chowdhury, Ph.D thesis, IPR Gandhinagar, India (2011)

[85] D. R. Hatch, M. J. Pueschel, F. Jenko, W. M. Nevins, P. W. Terry, and H. Doerk Phys. Plasmas 20, 012307 (2013)

[86] D.R. Smith, S.E. Parker, W. Wan, Y. Chen, A. Diallo, B.D. Dudson, R.J. Fonck, W. Guttenfelder, G.R. McKee, S.M. Kaye, D.S. Thompson, R.E. Bell, B.P. LeBlanc and M. Podesta Nucl. Fusion 53 (2013) 113029

[87] A. Ishizawa, S. Maeyama, T.-H. Watanabe, H. Sugama and N. Nakajima, J. Plasma Physics (2015), vol. 81, 435810203

[88] G. S. Bevli, A. K. Sundaram, and A. Sen Phys. Rev. E 48, 4121 (1993)

[89] G.S. Bevli, Tarsem Singh, Physics Letters A 236 (1997) 548-556

[90] P. W. Terry, K. D. Makwana, M. J. Pueschel, D. R. Hatch, F. Jenko and F. Merz Phys. Plasmas 21, 122303 (2014)

[91] X. Lapillonne, S. Brunner, T. Dannert, S. Jolliet, A. Marinoni, L. Villard, T. Görler, F. Jenko and F. Merz, Phys. Plasmas 16, 032308 (2009)

[92] Tobias Görler, Xavier Lapillonne, Stephan Brunner, Tilman Dannert, Frank Jenko, Sohrab Khosh Aghdam, Patrick Marcus, Ben F. McMillan, Florian Merz, Olivier Sauter, Daniel Told, and Laurent Villard, Phys. Plasmas. 18, 056103 (2011);

[93] T. S. Hahm, W. W. Lee and A. Brizard, Phys. Fluids **31**(7), 1940 (1988)

[94] A. J. Brizard, Phys. Rev. Lett. **84** 5768 (2000)